Novel *In-Vivo* Magnetic Resonance Spectroscopy Techniques for 3 T and 7 T



Clark Lemke

Kellogg College

University of Oxford

A thesis submitted for the degree of

Doctor of Philosophy

Trinity 2015

Dedicated to my parents.

Acknowledgements

First and foremost I'd like to thank Lisa Thomson who has single-handedly kept me together.

I'd also like to thank my great network of friends that I have had the pleasure of getting to know while in Oxford including Rob Frost, Velicia Bachtiar, Jane Olin-Ammentorp, Desiree Kellerman, Hannah Lloyd, Brendan MacEvilly, Clare Rowsome-Smith, Kevin Rowsome-Smith, Sinead Brady, Molly Franta, Justus Thompson, and Eve Binder.

I'd like to thank those at FMRIB that either helped directly, inspired or provided indirect support: Adam Berrington, Uzay Emir, Peter Jezzard, Aaron Hess, Charlie Stagg, Jamie Near, Benoit Schaller, Chris Rodgers, Karla Miller, Emma Lawrance and Heather Neyedli. I couldn't have done this without the help of those that volunteered to let me test my sequences, thank you so much for your time.

Abstract

This thesis describes several novel *in-vivo* proton magnetic resonance spectroscopy (MRS) techniques used to study the human brain. By measuring brain metabolites non-invasively, MRS has provided seminal contributions to our fundamental understanding of the brain as well as a wide variety of clinical conditions. However, due to the relative insensitivity and low spectral resolution of MRS, many important brain metabolites cannot be accurately quantified under standard clinical conditions. One way of increasing both the sensitivity and spectral resolution of MRS is to increase the static magnetic field strength. Unfortunately, increasing the static magnetic field strength also creates new technical challenges that must be resolved before any gains associated with higher magnetic field strength can be achieved.

Due to increased shimming requirements and hardware limitations, many MRS experiments at higher magnetic fields are performed on a single voxel in the brain - thereby limiting any possible insight that may be shed by concurrent measurements in other regions of the brain. This thesis presents a pragmatic acquisition scheme for concurrent acquisition of high quality spectra from multiple brain regions at ultra-high field (7 Tesla). This is accomplished by dynamically updating the first order shims and flip angles and acquiring spectra in an alternating fashion. The dynamic acquisition protocol produced spectra similar to static single voxel measurements demonstrating that high spectral quality from two voxels can be acquired concurrently without specialized hardware.

This dynamic acquisition scheme was then used to investigate the time-course of metabolites in both motor cortices (M1) following application of a non-invasive brain stimulation technique called transcranial direct current stimulation (tDCS). When applied over the motor cortex, tDCS has been shown to increase or decrease neuronal excitability depending on current direction. However, the pathways by which specific neurochemicals might mediate the tDCS-induced changes are not fully understood. Concurrent measurement of the tDCS time-courses revealed that anodal stimulation reduced GABA in both the anode-targeted and non-stimulated M1s. Cathodal stimulation decreased GABA and glutamate in the non-stimulated M1, with no changes in the cathode-targeted M1. Bilateral stimulation reduced glutamate in both M1 and no change in GABA.

Another problem associated with *in-vivo* MRS is that most metabolite peaks are overlapped by broad, unwanted macromolecule and lipid signals. At higher magnetic field strengths this can introduce significant bias in metabolite measurements. One way of avoiding this potential source of quantification error is to delay signal acquisition until the broad, unwanted signals have relaxed leaving only the metabolite signals present. The main problem with waiting for these broad macromolecule signals to relax is that scalar coupled metabolites will now evolve under J-coupling - rendering them very difficult to quantify. The final project involved development of a new pulse sequence designed to suppress J-modulation. Results show that J-modulation was sufficiently suppressed at 3 T long enough for nearly all the macromolecule signal to relax (up to TE = 150 ms). This technique can also be used for straight forward T_2 measurements of coupled metabolites.

Contents

Contents i

List of Figures iii

List of Tables v

1 Fundamentals of Magnetic Resonance Spectroscopy 3
- 1.1 Larmor Equation . . . 4
  - 1.1.1 Classical Description . . . 4
  - 1.1.2 Quantum Mechanical Description . . . 6
- 1.2 Macroscopic Magnetization . . . 8
- 1.3 The Bloch Equations and Signal Detection . . . 10
- 1.4 Chemical Shift . . . 15
- 1.5 Spin-spin Coupling . . . 17
- 1.6 Spin-echoes and J-modulation . . . 19

2 *In-Vivo* ^{1}H Magnetic Resonance Spectroscopy of the Brain 23
- 2.1 Hardware and Radio-frequency Pulses . . . 24
- 2.2 Magnetic Field Gradients and Slice Selection . . . 26
- 2.3 Phase Encoding . . . 29
- 2.4 Single Voxel Localization Techniques . . . 32
  - 2.4.1 PRESS . . . 32
  - 2.4.2 STEAM . . . 35
  - 2.4.3 semi-LASER . . . 37
- 2.5 Water Suppression . . . 39
- 2.6 Metabolites . . . 40
  - 2.6.1 N-Acetylaspartate . . . 40
  - 2.6.2 Creatine and Phosphocreatine . . . 41
  - 2.6.3 Glutamate and Glutamine . . . 41
  - 2.6.4 γ-Aminobutyric Acid . . . 42
- 2.7 Macromolecules and Lipids . . . 44
- 2.8 Magnetic Field Homogeneity and Shimming . . . 44
- 2.9 Quantification . . . 46
  - 2.9.1 Signal Averaging . . . 47
  - 2.9.2 Eddy Current Correction . . . 47

2.9.3 Residual Water Removal 48
2.9.4 Quantification and Calibration 48

3 Ultra-High Field Spectroscopy of the Brain 51
3.1 Motivation for Ultra-High Field Spectroscopy 51
3.2 Challenges Associated With B_1^+ 52
3.2.1 Energy Deposition and Requirements 52
3.2.2 B_1^+ Inhomogeneity 54
3.2.3 Solutions to B_1^+ Inhomogeneity 57
3.3 Challenges Associated With B_0 59
3.3.1 B_0 Inhomogeneity 59
3.3.2 Solutions to B_0 Inhomogeneity 61

4 Two-Voxel Spectroscopy With Dynamic B_0 Shimming and Flip Angle Adjustment at 7 T in the Human Cortex 63
4.1 Introduction 63
4.2 Experimental 64
4.3 Results 71
4.4 Discussion 74

5 Modulation of Cortical Neurotransmitters by Transcranial Direct Current Stimulation of the Human Motor Cortices 83
5.1 Introduction 83
5.2 Experimental 86
5.3 Results 89
5.4 Discussion 96

6 Refocusing *J*-modulation 99
6.1 Introduction 99
6.1.1 Short Vs. Long Echo Time Spectroscopy 99
6.1.2 Suppressing *J*-Modulation 100
6.2 Simulations 103
6.3 Experiments 107
6.3.1 Pulse Sequence 107
6.3.2 Phantom Experimental 110
6.3.3 Phantom Results 112
6.3.4 *In-Vivo* Experimental 112
6.3.5 *In-Vivo* Results 116
6.4 Discussion 116

7 Conclusion 123

References 128

A Density Matrix, Product Operator Formalism and Phase Cycling 141

List of Figures

1.1 Magnetic fields in the laboratory and rotating frames 12
1.2 Coherence generation by an excitation pulse 13
1.3 Free induction decay (FID) and Fourier transform 14
1.4 Energy levels for an isolated and coupled ^{1}H - ^{13}C spin system 18
1.5 Spin-echo pulse sequence and echo formation 21
1.6 J-modulation as a function of echo-time for IS spin system 22

2.1 Simulated RF pulse shapes and frequency profiles 25
2.2 Slice selection 28
2.3 Principle of phase encoding 31
2.4 PRESS pulse sequence diagram 34
2.5 Four-compartment artifact during PRESS 34
2.6 STEAM pulse sequence diagram 36
2.7 semi-Laser pulse sequence diagram and adiabatic pulses 37
2.8 Simulated ^{1}H spectrum of glutamate and glutamine 42
2.9 Pulse sequence diagram for MEGA-PRESS 43
2.10 Flow chart for processing and quantification of *in-vivo* spectra. 47

3.1 Simulated axial images as a function of field strength 56
3.2 Comparison of spectra acquired with and without dielectric pads . . . 60

4.1 Barium titanate dielectric pads 65
4.2 B_1^+ maps with a variety of dielectric pads 67
4.3 Acquisition scheme for ^{1}H dual-voxel spectroscopy 68
4.4 B_1^+ field maps with and without dielectric pads 72
4.5 ^{1}H semi-LASER spectra at 7 T using static and DSU 73
4.6 Neurochemical profiles and CRLBs 75
4.7 Correlation coefficient matrices between metabolite concentrations . . 76
4.8 Average and 95% confidence interval of agreement 77

5.1 tDCS electrode placement for anodal, cathodal and bilateral tDCS . . 84
5.2 Average baseline ^{1}H spectra prior to tDCS 90
5.3 Anodal stimulation timecourse 93
5.4 Cathodal stimulation timecourse 94
5.5 Bilateral stimulation timecourse 95

6.1 Pulse sequence diagrams for CPMG and PROJECT sequences 103
6.2 J-modulation as a function of echo time 104
6.3 Simulated integrals for CPMG and PRESS-JR 105
6.4 Simulated spectra PRESS-JR for a range of echo times 106
6.5 Diagram of PRESS-JR 106
6.6 Gradient amplitudes and orientations for PRESS-JR. 108
6.7 Slice profile comparison for PRESS-JR. 108
6.8 Slice profile of PRESS and PRESS-JR. 111
6.9 Phantom PRESS-JR spectra 113
6.10 Phantom concentrations. 114
6.11 Phantom CRLBs. 115
6.12 *In-vivo* PRESS-JR spectra 117
6.13 *In-vivo* concentrations. 118
6.14 Frequency response of the 180° composite pulses 120

7.1 Short and long TE tumor spectra. 125
7.2 PRESS-JR with phase encoding 127

List of Tables

2.1 Spherical harmonics used for shimming 46

4.1 Linewidths, SNR and tissue content for experiments 74
4.2 Bland-Altman agreement assessment 77

5.1 Average CRLBS in left and right M1s 90

6.1 Phase cycle used to remove spurious echoes. 109
6.2 Phantom metabolite T_2s 112
6.3 *In-vivo* CRLBs for PRESS and PRESS-JR 118

A.1 Product operators for a two spin-1/2 system 144
A.2 Hamiltonians for Product Operator Formalism 144
A.3 Summary of product operator formalism 145
A.4 Phase cycle to select coherence transfer from +2 to -1. 146
A.5 Phase cycle for $\Delta p = +2$ 146

Preface

Thesis Overview

This thesis is structured around three journal articles describing new techniques for magnetic resonance spectroscopy of the brain. The first three chapters provide the background to the field. Chapter 1 describes the fundamentals of magnetic resonance spectroscopy. Chapter 2 focuses on specific aspects of *in-vivo* spectroscopy of the brain, including acquisition, processing, and quantification. Chapter 3 reviews the challenges and current solutions for ultra-high field spectroscopy of the brain. Chapter 4 expands on a paper, published in 2015, which describes a new acquisition scheme for concurrent acquisition of multiple voxels using conventional hardware 7 T. Chapter 5 implements the aquisition scheme described in Chapter 4 to metabolite timecourses in both motor cortices following transcranial direct-current stimulation and will be submitted as a paper in the near future. Chapters 4 and 5 were a collaboration with Velicia Bachtiar, Charlotte Stagg and Heidi Johansen-Berg of the Plasticity Group at FMRIB and I would like to acknowledge the contribution of Velicia Bachtiar, who performed the statistical analysis in Chapter 5, in collaboration with myself. In particular, she performed the repeated-measures ANOVAs for each tDCS stimulation condition and produced the figures for metabolite time-courses following tDCS. The thesis concludes with a final chapter discussing future research involving these projects.

This thesis resulted in the following works:

- Clark Lemke, Aaron Hess, Stuart Clare, Velicia Bachtiar, Charlotte Stagg, Peter Jezzard and Uzay Emir. Two-voxel spectroscopy with dynamic B0 shimming and flip angle adjustment at 7 T in the human motor cortex. 27:7, 852-860. NMR in Biomedicine, 2015.

- Clark Lemke, Peter Jezzard, Jamie Near, Uzay Emir and Aaron Hess. Long echo time in-vivo spectroscopy without J-modulation using perfect echoes. (In preparation).

- Clark Lemke, Aaron Hess, Jamie Near, Stuart Clare, Peter Jezzard, and Uzay Emir. Long echo time in-vivo spectroscopy without J-modulation. Poster at ISMRM 2015.

- Clark Lemke, Aaron Hess, Velicia Bachtiar, Stuart Clare, Charlotte Stagg, Peter Jezzard, and Uzay Emir. Two-Voxel Spectroscopy With Dynamic B0 Shimming and Flip Angles at Ultra High Field. Poster at ISMRM 2014.

- Clark Lemke, Uzay Emir, Peter Jezzard, Stuart Clare, and Jamie Near. Localized Spectroscopy Without J-modulation at Ultra High Field. Poster at ISMRM 2014.

- Clark Lemke, Jamie Near, Uzay Emir, Peter Jezzard. PRESS-JR: Long echo-time in vivo spectroscopy without J-modulation. Poster at ISMRM-British Chapter 2013.

Chapter 1

Fundamentals of Magnetic Resonance Spectroscopy

Magnetic resonance is a physical phenomenon caused by the interaction between matter and electromagnetic (EM) radiation when in the presence of an external magnetic field. EM radiation will only be absorbed or emitted at specific frequencies corresponding to characteristic energy level differences in the atoms or molecules in the magnetic field. This was first observed by Rabi [1] at Columbia University in 1937 and subsequently by Purcell *et al.* [2] at Stanford University and Bloch *et al.* [3] at Harvard University in 1946 who used the technique to determine nuclear magnetic moments of nuclei. For their work, Rabi was awarded the 1944 Nobel prize in physics and Purcell and Bloch were jointly awarded the 1952 Nobel prize in physics. However it was not until 1950 that Proctor and Yu [4] at Stanford and Dickinson [5] at MIT realized that nuclei of the same type within the same molecule absorb energy at different resonance frequencies. Connecting differences in resonant frequencies with variations in the chemical environment of those nuclei provided a catalyst that resulted in nuclear magnetic resonance (NMR) spectroscopy becoming one of the most important and useful scientific techniques of the past 60 years.

Due to the comparatively low absorption of RF radiation in NMR experiments, NMR is non-invasive - making it ideal for *in-vivo* measurements. Shortly after its inception NMR was applied to biological tissues and subsequently on intact, living tissues. In 1971, Damadian [6] at the State University of New York (SUNY) showed that NMR spectroscopy could be used to discriminate between healthy tissue and malignant tumors - highlighting the medical potential of NMR. In parallel with NMR spectroscopy, in 1973, Lauterbur [7] at SUNY and Mansfield and Grannell [8] at Nottingham discovered a technique to spatially encode NMR signals leading to the development of magnetic resonance imaging (MRI). MRI has become one of the most widely employed medical imaging techniques to investigate both anatomy and physiology. Lauterbur and Mansfield were awarded the 2003 Nobel prize in medicine for their foundational work. Since their formation, MRS and MRI have been developed in tandem and have evolved from simple experiments designed to measure nuclear magnetic moments into versatile, complex techniques that can used to examine a wide variety of applications including determining molecular structure, quantifying *in-vivo* neurotransmitters or monitoring brain activity in real time.

1.1 Larmor Equation

1.1.1 Classical Description

A more complete treatment of the fundamentals of MR can be found in [9] or [10].

The quantum mechanical concept of nuclear spin is the foundation for NMR. While nuclear spin is an inherently quantum mechanical phenomena and, therefore, classical physics is not adequate to completely describe an NMR experiment, classical physics provides a simple and intuitive explanation for most of the concepts discussed throughout this thesis.

A particle rotating with constant velocity about a fixed point is described by its

angular momentum $\mathbf{L}$ which is given by the cross product of its linear momentum $\mathbf{p}$ and its position relative to the point about which it is rotating $\mathbf{r}$:

$$\mathbf{L} = \mathbf{r} \times \mathbf{p} \tag{1.1}$$

The angular momentum of a particle is changed by applying a torque $\mathbf{T}$:

$$\mathbf{T} = \mathbf{r} \times \frac{\mathrm{d}\mathbf{p}}{\mathrm{d}t} = \frac{\mathrm{d}\mathbf{L}}{\mathrm{d}t} \tag{1.2}$$

If we consider a rotating particle of mass m possessing an electric charge q which forms a current loop I, a magnetic field will be created. A characteristic property of the generated magnetic field is called the magnetic dipole moment $\boldsymbol{\mu}$ which here is equal to IA where A is the area of the loop and can be expressed as:

$$\boldsymbol{\mu} = IA = \frac{q\mathbf{v}}{2\pi r}\pi r^2 = \frac{q}{2m}\mathbf{L} = \gamma\mathbf{L} \tag{1.3}$$

where γ is the classical gyromagnetic ratio and $\mathbf{L} = r \times m\mathbf{v}$. When the rotating particle is placed in a magnetic field $\mathbf{B_0}$, the loop experiences a torque given by:

$$\mathbf{T} = \boldsymbol{\mu} \times \mathbf{B_0} \tag{1.4}$$

Combining Eq. 1.2, 1.3 and 1.4 we find:

$$\mathbf{T} = \frac{\mathrm{d}\mathbf{L}}{\mathrm{d}t} = \frac{\mathrm{d}\boldsymbol{\mu}}{\mathrm{d}t} = \gamma\boldsymbol{\mu} \times \mathbf{B_0} \tag{1.5}$$

As the particle rotates, the amplitude of $\boldsymbol{\mu}$ does not change, therefore Eq. 1.5 describes the rotation (or precession) about $\mathbf{B_0}$ and can be expressed in terms of a frequency:

$$\frac{\mathrm{d}\boldsymbol{\mu}}{\mathrm{d}t} = \gamma\boldsymbol{\mu} \times \mathbf{B_0} = \boldsymbol{\mu}\boldsymbol{\omega}_0 \tag{1.6}$$

or alternatively as the famous Larmor formula:

$$\boldsymbol{\omega}_0 = \gamma \mathbf{B_0} \tag{1.7}$$

Eq. 1.7 expresses that the frequency of precession is proportional to the applied field and the gyromagnetic ratio - which is characteristic for the particle or nucleus examined. Hence, measurement of the precession frequency at a known magnetic field can determine the species (hydrogen, nitrogen, etc.) of an unknown particle.

The potential energy $\mathbf{E}$ of a magnetic moment $\boldsymbol{\mu}$ in a magnetic field $\mathbf{B_0}$ is defined as the work of the magnetic torque on re-alignment of the magnetic moment vector from the magnetic field:

$$\mathbf{E} = -\boldsymbol{\mu} \cdot \mathbf{B_0} = -\mu \mathrm{B}_0 \cos\theta \tag{1.8}$$

where θ is the angle between the magnetic moment $\boldsymbol{\mu}$ and the magnetic field $\mathbf{B_0}$. From Eq. 1.8 we see that the energy can take any value between $-\mu \mathrm{B}_0$ and $\mu \mathrm{B}_0$ and is minimized when $\theta = 0$ or when the magnetic moment is parallel with the magnetic field and maximized when $\theta = 180$ or when the magnetic moment is anti-parallel with the magnetic field. This is where the classical description of magnetic resonance begins to break down - as the observed magnetic resonance condition is more constrained. In order to fully explain the observed magnetic resonance condition, one must examine the quantum relationship between electromagnetic waves and nuclear spins.

1.1.2 Quantum Mechanical Description

One of the most important results of quantum mechanics is that the angular momentum of elementary particles is quantized with amplitude given by:

$$\mathrm{L} = \hbar \sqrt{I(I+1)} \tag{1.9}$$

where $\hbar$ is Planck's constant (divided by 2π) and I is the spin quantum number which can only take integral or half-integral values. For electrons, protons and neutrons $I = 1/2$. For ^{1}H, ^{13}C, and ^{31}P $I = 1/2$, and for ^{2}H $I = 1$. Remarkably, the direction of the angular momentum is also quantized with the component of angular momentum in the z direction L_z given by:

$$\mathrm{L}_z = \hbar m_z \tag{1.10}$$

where m_z can only take $2I + 1$ values given by:

$$m_z = I, I - 1, I - 2, \ldots, -I \tag{1.11}$$

Just as in classical physics, elementary particles have a magnetic moment $\boldsymbol{\mu}$ related to their angular momentum $\mathbf{L}$ through Eq. 1.3. Only now the angular momentum L is quantized and therefore the magnetic moment μ will also be quantized. For the z component of the magnetic moment μ we find:

$$\mu_z = \gamma \hbar m \tag{1.12}$$

When placed in a magnetic field $\mathbf{B_0}$ (conventionally aligned with the positive z-axis), the energy of a magnetic moment is given by Eq. 1.8, and when we combine this with Eq. 1.12, we find:

$$\mathrm{E} = -\mu_z \cdot \mathrm{B}_0 = -\gamma \hbar m \mathrm{B}_0 \tag{1.13}$$

As m is discrete, the energy levels are also discrete. For an $I = 1/2$ spin we have two energy levels $m = 1/2$ and $m = -1/2$ with energy difference between these states E_Δ given by:

$$\mathrm{E}_\Delta = \gamma \hbar \mathrm{B}_0 \tag{1.14}$$

The magnetic resonance condition is satisfied when an oscillating magnetic field perpendicular to the z axis is applied with a frequency ω such that the energy $\mathrm{E_{res}}$ equals that of Eq. 1.14:

$$\mathrm{E_{res}} = \hbar\omega \tag{1.15}$$

Combining Eq. 1.14 and Eq. 1.15, we once again arrive at the Larmor equation (Eq. 1.7):

$$\omega = \gamma \mathrm{B_0} \tag{1.16}$$

For all relevant NMR experiments, the applied magnetic field corresponds to electromagnetic radiation in the radio-frequency range. As the magnetic moment is quantized, the angle between the magnetic moment and static magnetic field is no longer continuous as predicted in Eq. 1.8. Instead, using the expressions for L_z and L from Eq. 1.9 and Eq. 1.10 we have:

$$\cos\theta = \frac{\mathrm{L_z}}{\mathrm{L}} = \frac{m}{\sqrt{I(I+1)}} \tag{1.17}$$

For a $I = 1/2$ ($m = -1/2, 1/2$) we find that θ must be 54.7 or -54.7 relative to the z-axis. Therefore, a particle's nuclear spin will precess at the Larmor frequency ω along a cone either parallel or anti-parallel to the magnetic field.

1.2 Macroscopic Magnetization

Thus far we have only discussed individual nuclear spins. However, all NMR experiments consist of examining a macroscopic sample containing many spins. In a macroscopic sample of $I = 1/2$ spins, the spins will be randomly distributed along the cones predicted by Eq. 1.17 with a small population difference due to the energy difference between the two states. The Boltzmann equation and Eq. 1.15 can be used

to calculate the population difference:

$$\frac{\mathrm{n}_\alpha}{\mathrm{n}_\beta} = \mathrm{e}^{\mathrm{E}_\Delta/\mathrm{k_B T}} = e^{\hbar\omega/\mathrm{k_B T}} \approx 1 + \frac{\hbar\omega}{\mathrm{k_B T}} \tag{1.18}$$

where α and β refer to the parallel and anti-parallel states respectively, $\mathrm{k_B}$ is the Boltzmann constant and T is temperature. The last step is performed by truncation after the second element of a Taylor expansion of the exponential. For a typical human (T = 37 °C) experiment at 7 T (ω = 297 MHz) we would only find a difference of about 0.0024% between the two states. This small population difference leads to a relative insensitivity of NMR when compared with other forms of spectroscopy.

For a number of spins n the net sum of the individual magnetic moments $\boldsymbol{\mu}$ is called the magnetization $\mathbf{M}$. The group of spins will be randomly distributed along cones as described in section 1.1.2 and therefore there will be no net component in the xy-plane (transverse plane). Due to the population difference expressed in Eq. 1.18, there will be a non-zero magnetization along the z-axis (longitudinal direction) M_0 given by:

$$\mathrm{M}_0 = \sum_{i=0}^{n} \mu_i = n_\alpha \mu_{z,\alpha} + n_\beta \mu_{z,\beta} = \frac{\gamma\hbar}{2} n_\alpha - \frac{\gamma\hbar}{2} n_\beta = \frac{\gamma\hbar}{2}(n_\alpha - n_\beta) \tag{1.19}$$

which can be expressed in terms of the total number of spins $n = n_\alpha + n_\beta$:

$$\mathrm{M}_0 = \frac{\gamma\hbar}{2}\left(\left(\frac{n}{2} - \frac{n\hbar\omega}{2\mathrm{k_B T}}\right) - \left(\frac{n}{2} - \frac{n\hbar\omega}{\mathrm{k_B T}}\right)\right) = \frac{\gamma\hbar}{2}\left(\frac{n\hbar\omega}{2\mathrm{k_B T}}\right) = \frac{n(\gamma\hbar)^2 \mathrm{B}_0}{4\mathrm{k_B T}} \tag{1.20}$$

As we will see in the next section M_0 is proportional to the NMR sensitivity. Eq. 1.20 reveals a number of important considerations for increasing sensitivity in NMR experiments. Increasing the number of spins n (increasing spin density or sample size) linearly increases the magnetization at thermal equilibrium. The quadratic dependance on the gyromagnetic ratio leads to large differences in sensitivity between

nuclei. ^{1}H has the largest γ and spin density of nuclei encountered in the body and therefore the greatest NMR sensitivity for *in-vivo* experiments. Magnetization also increases linearly with magnetic field strength, leading to demand for higher field magnets. Decreasing the temperature will also increase the magnetization and, though this is obviously not feasible for *in-vivo* applications, it is widely exploited in other NMR applications.

1.3 The Bloch Equations and Signal Detection

The magnetization in the longitudinal direction, M_z, is almost undetectable it its equilibrium state although it is possible to observe directly with SQUIDS [11] or field probes [12]. Therefore, in order to exploit the Larmor equation and resonance condition one must apply an additional magnetic field $\mathbf{B}_1$ in order to tip M_0 onto the transverse plane. As we will see, the transverse magnetization will induce a detectable signal in a receive coil.

To begin, we extend Eq. 1.6 from describing an individual magnetic moment to describing the magnetization of a sample:

$$\frac{d\mathbf{M}}{dt} = \gamma \mathbf{M} \times \mathbf{B}(t) \tag{1.21}$$

where $\mathbf{B}(t)$ includes both the static $\mathbf{B}_0$ and the additional, time-varying magnetic field $\mathbf{B}_1(t)$. For most conditions, the relevant $\mathbf{B}_1$ is given by:

$$\mathbf{B}_1(t) = B_1 \cos(\omega_{rf} t + \phi)\hat{\mathbf{x}} + B_1 \sin(\omega_{rf} t + \phi)\hat{\mathbf{y}} \tag{1.22}$$

where ω_{rf} is the frequency and ϕ is the initial phase offset of the oscillating field. Eq.

1.21 can be expressed as the Bloch equations without relaxation [3]:

$$\begin{aligned}
\frac{\mathrm{dM}_x}{\mathrm{d}t} &= \gamma\left(\mathrm{M}_y(t)\mathrm{B}_0 - \mathrm{M}_z(t)\mathrm{B}_1\sin(\omega_{rf}t+\phi)\right) \\
\frac{\mathrm{dM}_y}{\mathrm{d}t} &= \gamma\left(\mathrm{M}_z(t)\mathrm{B}_1\cos(\omega_{rf}t+\phi) - \mathrm{M}_x(t)\mathrm{B}_0\right) \\
\frac{\mathrm{dM}_z}{\mathrm{d}t} &= \gamma\left(\mathrm{M}_x(t)\mathrm{B}_1\sin(\omega_{rf}t+\phi) - \mathrm{M}_y(t)\mathrm{B}_1\cos(\omega_{rf}t+\phi)\right)
\end{aligned} \tag{1.23}$$

In reality, when $\mathbf{M}$ is perturbed from its equilibrium state it will attempt to return to the original (equilibrium) state by a process called relaxation. The complicated interactions responsible for relaxation can be accurately approximated as exponential processes with one time constant for relaxation in the longitudinal direction (T_1) and another for relaxation in the transverse direction (T_2). Including relaxation into the Bloch equations gives:

$$\begin{aligned}
\frac{\mathrm{dM}_x}{\mathrm{d}t} &= \gamma\left(\mathrm{M}_y(t)\mathrm{B}_0 - \mathrm{M}_z(t)\mathrm{B}_1\sin(\omega_{rf}t+\phi)\right) - \frac{\mathrm{M}_x(t)}{T_2} \\
\frac{\mathrm{dM}_y}{\mathrm{d}t} &= \gamma\left(\mathrm{M}_z(t)\mathrm{B}_1\cos(\omega_{rf}t+\phi) - \mathrm{M}_x(t)\mathrm{B}_0\right) - \frac{\mathrm{M}_y(t)}{T_2} \\
\frac{\mathrm{dM}_z}{\mathrm{d}t} &= \gamma\left(\mathrm{M}_x(t)\mathrm{B}_1\sin(\omega_{rf}t+\phi) - \mathrm{M}_y(t)\mathrm{B}_1\cos(\omega_{rf}t+\phi)\right) - \frac{\mathrm{M}_z(t)-\mathrm{M}_0}{T_1}
\end{aligned} \tag{1.24}$$

These equations are rather difficult to follow and it is more intuitive to transform these equations into a rotating frame denoted $\hat{\mathbf{x}}'$, $\hat{\mathbf{y}}'$, $\hat{\mathbf{z}}'$. If we use a frame aligned with the z-axis in the same direction as $\mathbf{B}_0$ ($\hat{\mathbf{z}} = \hat{\mathbf{z}}'$) but with x and y axes rotating about $\mathbf{B}_0$ with frequency ω_{rf}, we see that Eq. 1.22 simplifies to $\mathbf{B}_1'(t) = \mathrm{B}_1\cos\phi\hat{\mathbf{x}}' + \mathrm{B}_1\sin\phi\hat{\mathbf{y}}'$ and now:

$$\begin{aligned}
\mathrm{M}'_x &= \mathrm{M}_x\cos\omega_{rf}t + \mathrm{M}_y\sin\omega_{rf}t \\
\mathrm{M}'_y &= \mathrm{M}_y\cos\omega_{rf}t - \mathrm{M}_x\sin\omega_{rf}t \\
\mathrm{M}'_z &= \mathrm{M}_z
\end{aligned} \tag{1.25}$$

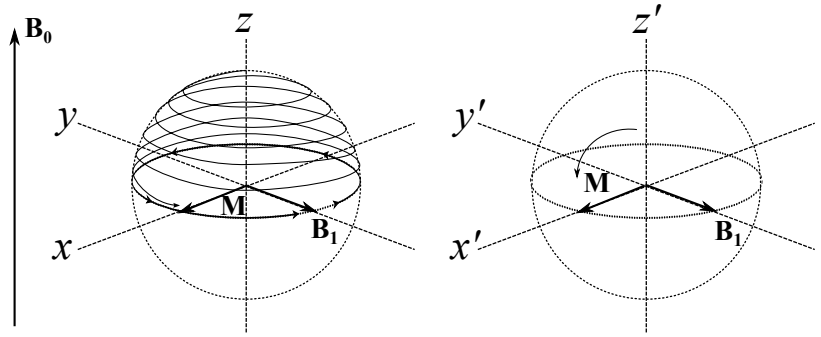


Figure 1.1: Magnetic fields $\mathbf{B}_0$ and $\mathbf{B_1}$ and magnetization $\mathbf{M}$ in the laboratory (left) and rotating frames (right). The periodic behaviour of $\mathbf{M}$ and $\mathbf{B_1}$ in the laboratory frame complicate comprehension whereas in the rotating frame the effect of $\mathbf{B_1}$ is more easily understood.

In the rotating frame the Bloch equations become:

$$\begin{aligned}
\frac{\mathrm{d}\mathrm{M'}_x}{\mathrm{d}t} &= \mathrm{M'}_y(t)(\omega_0 - \omega_{rf}) - \mathrm{M'}_z(t)\gamma\mathrm{B}_1\sin(\phi) - \frac{\mathrm{M'}_x(t)}{T_2} \\
\frac{\mathrm{d}\mathrm{M'}_y}{\mathrm{d}t} &= M'_z(t)\mathrm{B}_1\cos(\phi) - \mathrm{M'}_x(t)\gamma(\omega_0 - \omega_{rf}) - \frac{\mathrm{M'}_y(t)}{T_2} \\
\frac{\mathrm{d}\mathrm{M'}_z}{\mathrm{d}t} &= \gamma\left(\mathrm{M'}_x(t)\mathrm{B}_1\sin(\phi) - \mathrm{M'}_y(t)\mathrm{B}_1\cos(\phi)\right) - \frac{\mathrm{M'}_z(t) - \mathrm{M}_0}{T_1}
\end{aligned} \tag{1.26}$$

where we have used Eq. 1.7. At first glance, changing reference frames may not appear to simplify matters but, in the rotating frame, the time-dependent precession has been removed. The advantage of the rotating frame is illustrated in Fig. 1.1.

It should be noted that the Bloch equations only apply to the macroscopic magnetization and not to individual spins. As mentioned in Section 1.1.2, the individual spins can only be in a parallel or anti-parallel state. Fig. 1.2 illustrates how individual spins are not tipped but form a so-called coherence resulting in the magnetization vector being tipped into the transverse plane.

In modern NMR experiments, $\mathbf{B_1}$ is applied as a pulse (*i.e.* turned on for a time and then turned off). Pulses are denoted by the angle they tip the magnetization vector. Following a 90° pulse, the magnetization will precess in the transverse plane at the Larmor frequency. If a coil is placed in the transverse plane, according to

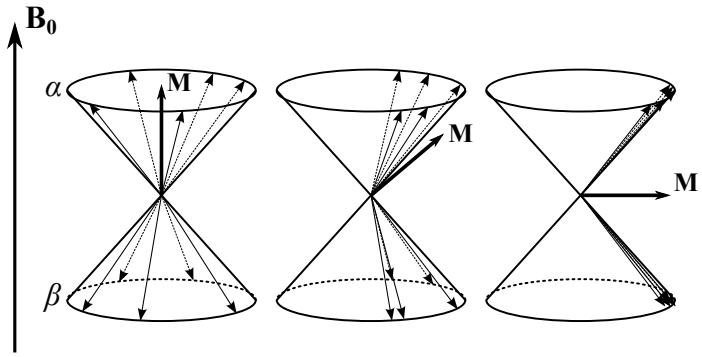


Figure 1.2: Application of an additional magnetic field perpendicular to the static magnetic field. Initially the spins are randomly distributed along cones (α or β) and therefore the magnetization is aligned with $\mathbf{B_0}$. The additional magnetic field forms a coherence between the spins and the magnetization vector tips towards the transverse plane.

Faraday's law, an emf will be induced in the coil and, due to T_2 relaxation, the emf will decrease over time. The detected emf is called the free-induction decay (FID). Solving the Bloch equations for the detectable components after a 90° pulse:

$$\begin{aligned} \mathrm{M}_x = &\quad \mathrm{M}_0 \cos\left((\omega_0 - \omega_{rf})t + \phi\right) \mathrm{e}^{-t/T_2} \\ \mathrm{M}_y = &\quad \mathrm{M}_0 \sin\left((\omega_0 - \omega_{rf})t + \phi\right) \mathrm{e}^{-t/T_2} \end{aligned} \tag{1.27}$$

where M_x and M_y are commonly referred to as the real and imaginary FIDs respectively and are illustrated in Fig. 1.3.a. Alternatively, Eq. 1.27 can be described by the combined complex form:

$$\mathrm{M}_{xy} = \mathrm{M}_x + i\mathrm{M}_y = \mathrm{M}_0 \mathrm{e}^{i(\omega_0 - \omega_{\mathrm{rf}})\mathrm{t} + \phi} \mathrm{e}^{-t/T_2} \tag{1.28}$$

Though the detected FIDs provide the desired information, it is generally more useful to convert the time domain signal $s(t)$ into the frequency domain $S(w)$ through the Fourier Transform:

$$S(\omega) = \int_0^\infty s(t) \mathrm{e}^{-i\omega t} \mathrm{dt} \tag{1.29}$$

Generally both real and imaginary signals are acquired (quadrature detection) in

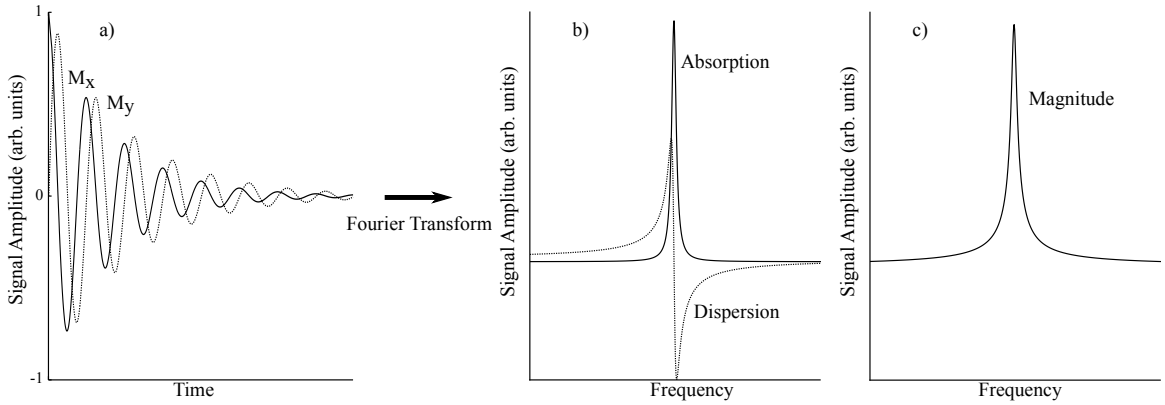


Figure 1.3: a) Free induction decay (FID) of magnetization following a 90 pulse. b) Fourier transform of a FID results in mixture of absorption and dispersion components. After phasing the spectrum ($\phi = 0$), the absorption peak will be fully upright and the line-width can be calculated by taking the full width at half maximum. c) Magnitude of the two components. The phase information has been lost and the peak width has increased due to the wide tails of the dispersion component.

order to discriminate positive from negative frequencies as $\cos(\omega) = \cos(-\omega)$. Taking the Fourier transform of our FIDs (Eq. 1.27) results in a spectrum comprised of a real $\mathrm{Re}\{S(\omega)\}$ and imaginary component $\mathrm{Im}\{S(\omega)\}$:

$$\begin{aligned} \mathrm{Re}\{S(\omega)\} &= \mathrm{A}(\omega)\cos\phi - \mathrm{D}(\omega)\sin\phi \\ \mathrm{Im}\{S(\omega)\} &= \mathrm{A}(\omega)\sin\phi + \mathrm{D}(\omega)\cos\phi \end{aligned} \tag{1.30}$$

where:

$$\begin{aligned} \mathrm{A}(\omega) &= \frac{\mathrm{M}_0 T_2}{1 + (\omega_0 - \omega)^2 T_2^2} \\ \mathrm{D}(\omega) &= \frac{(\omega_0 - \omega_{rf})\mathrm{M}_0 T_2}{1 + (\omega_0 - \omega)^2 T_2^2} \end{aligned} \tag{1.31}$$

$\mathrm{A}(\omega)$ and $\mathrm{D}(\omega)$ are the absorption and dispersion components of the Lorentzian function as illustrated in Fig. 1.3.b. Note that the width at half maximum of the absorption peak is $\frac{1}{\pi T_2}$, hence shorter T_2 leads to a broader peak. The absorption pattern is narrower and therefore for better separation of peaks the absorption spectrum is preferred. To obtain a purely absorption spectrum we need $\phi = 0$. This is adjustable in post-processing and called zero-order phase correction. Due to hardware imper-

fections, ϕ may depend on ω and therefore we may have to include first-order phase correction $\phi = \phi_0 + (\omega_0 - \omega)\phi_1$. If the phase of the signal is not relevant, the magnitude signal can be calculated by:

$$\|S(\omega)\| = \sqrt{\mathrm{Re}\{S(\omega)\}^2 + \mathrm{Im}\{S(\omega)\}^2} \tag{1.32}$$

Note that due to the inclusion of the dispersion component, the magnitude peak will be broader than the in-phase real component as illustrated in Fig. 1.3.c.

1.4 Chemical Shift

Thus far we have assumed that our macroscopic sample contains only a single type of nucleus resonating with a single frequency. If this were always the case, NMR spectroscopy would not be particularly useful. Fortunately the resonance frequency ω depends not only on the gyromagnetic ratio γ and the external magnetic field $\mathbf{B_0}$, but also on the local chemical environment of the specific nucleus under investigation. When a nucleus is placed in a magnetic field, the electrons surrounding the nucleus possess their own magnetic moment $\boldsymbol{\mu}$ which will alter the effective magnetic field experienced by the nucleus. The effective magnetic field $\mathbf{B_{eff}}$ is now:

$$\mathbf{B_{eff}} = (1 - \sigma)\mathbf{B_0} \tag{1.33}$$

where σ is the chemical shielding constant of the local electrons acting on the nucleus in question. Hence the resonance frequency is now given by:

$$\omega = \gamma(1 - \sigma)\mathbf{B_0} \tag{1.34}$$

The effect of electron shielding is generally expressed as the chemical shift δ and in units of parts per million (ppm) as units of Hertz would be magnetic field dependent:

$$\delta = \frac{\omega - \omega_{ref}}{\omega_{ref}} \times 10^6 \tag{1.35}$$

where ω_{ref} is the resonance frequency of a known reference compound. The most common reference compounds are tetramethylsilane (TMS) and 2,2-dimethyl-2-silapentane-5-sulfonate (DSS) but as they are both toxic, they are not generally used for *in-vivo* spectroscopy. In order to determine the chemical shift without an external reference compound a different equation is used:

$$\delta = \frac{\omega}{\omega_{trans} \times 10^{-6}} + \text{offset} \tag{1.36}$$

where ω_{trans} is the transmitter frequency and offset is a constant that references the ppm scale to an *in-vivo* standard which is usually the methyl peak of N-acetyl aspartate (NAA) with a chemical shift value of 2.01 ppm (see Sec. 2.6.1). Conventionally, resonance frequencies are plotted increasing from right to left and large ppm values are called "down-field" and small ppm values are designated "up-field". Hence, if we place a macroscopic sample containing a number of different chemical environments, we will find a number of separate peaks in our spectrum. This is the basis of NMR spectroscopy; different molecules in a sample resonate with slightly different frequencies, all of which can (ideally) be measured, separated, and analyzed. Under ideal conditions and after correcting for relaxation, the integral of each peak is proportional to the concentration of each spin population rendering NMR spectroscopy a powerful tool for quantitative measurements.

1.5 Spin-spin Coupling

There are a number of additional interactions between nuclei that can influence the appearance of the resulting NMR spectrum: dipolar coupling, the nuclear Overhauser effect and spin-spin coupling. Dipolar coupling occurs between two particles with non-zero spin directly through space. Although dipolar coupling is one of the main causes of relaxation [13], due to rapid changes in molecular orientation seen in liquids, there is no net dipolar interaction for liquids and hence no effect on *in-vivo* spectra (except for T_1 and T_2 relaxation). The nuclear Overhauser effect occurs by transfer of polarization between spin populations via the dipolar interaction when one population is relaxing and can result in a change in peak intensity of nearby nuclei [14, 15]. Unlike dipolar coupling, the nuclear Overhauser effect can effect liquid spectra but is mainly of concern for experiments performed on nuclei other than ^{1}H. Finally, spin-spin coupling (also called scalar coupling or J-coupling) occurs through the bonds between nearby spins [16]. This results in the splitting of certain resonance peaks into smaller lines and is extremely important for *in-vivo* NMR spectroscopy.

To visualize how spin-spin coupling works we take an isolated spin system of one ^{1}H particle and one ^{13}C particle (Fig. 1.4.a) and examine the uncoupled and coupled cases. For the uncoupled case each of the two particles can be in one of two states α or β so that the total spin system has four possible states: $\beta_{\mathrm{H}}\beta_{\mathrm{C}}$, $\beta_{\mathrm{H}}\alpha_{\mathrm{C}}$, $\alpha_{\mathrm{H}}\beta_{\mathrm{C}}$, $\alpha_{\mathrm{H}}\alpha_{\mathrm{C}}$. For this system there are four allowed energy transitions giving rise to two resonance frequencies ω_{H} and ω_{C} as illustrated in Fig. 1.4.b. For the coupled case we have to include the Pauli exclusion principle which requires the electron spins be anti-parallel with each other. This gives rise to new favourable and unfavourable energy states as illustrated in Fig. 1.4.c. resulting in a splitting of ω_{H} into $\omega_{\mathrm{H}} \pm \frac{J}{2}$ and ω_{C} into $\omega_{\mathrm{C}} \pm \frac{J}{2}$ where J is the scalar coupling constant between the particles.

Analysis of complicated coupled spectra is facilitated by labeling spin systems according to Pople notation [17]. Each set of magnetically equivalent spins is desig-

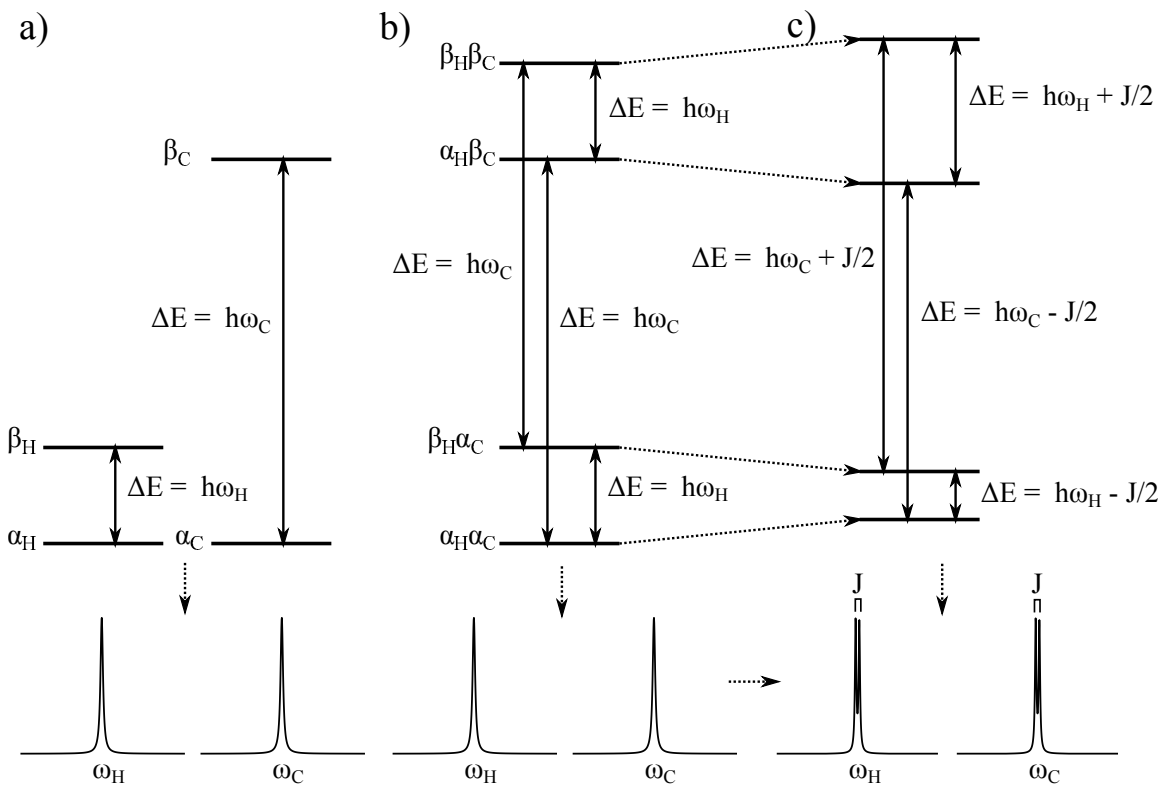


Figure 1.4: Energy level diagrams for a) isolated ^{1}H and ^{13}C nuclei, b) uncoupled ^{1}H - ^{13}C and c) coupled ^{1}H - ^{13}C (covalent bond). Below each energy level diagram is the corresponding spectrum. The isolated and uncoupled cases give rise to singlet resonances but the coupled case has perturbed energy states resulting in splitting of singlet resonances into two peaks each separated by the coupling constant J.

nated by a letter. Coupled spins in which the chemical shift difference is much larger than the coupling strength (weakly coupled) are referred to as AX or AMX. Coupled spins in which the chemical shift difference is on the order of the scalar coupling (strongly coupled) are referred to by adjacent letters (AB, NM, etc.). The number of magnetically equivalent spins in each set is denoted by the subscript so that CH_3 would be an AX_3 spin system. The number of peaks resulting from splitting for an A_nX_m spin system is $m+1$ for the A spins and $n+1$ for the X spins with the relative amplitudes of the peaks given by the binomial distribution. For example the AX_3 spin system would have the A resonance splitting into four peaks with relative amplitudes of 1:3:3:1 and the X_3 resonance splitting into two peaks of equal amplitude.

1.6 Spin-echoes and J-modulation

In order to acquire NMR signal the spins must possess a phase coherence. If there is no phase coherence the transverse component of the magnetization vector $\mathbf{M}_x(t)$, $\mathbf{M}_y(t)$ will be zero and hence no signal can be detected. As mentioned in Eq. 1.27, after applying a 90° pulse, phase coherence decreases exponentially with intrinsic time constant T_2. Unfortunately this does not tell the complete picture. T_2 only includes local interactions at the atomic and molecular levels, in which spins affect each other by their individual oscillating magnetic fields. Unfortunately, magnetic field $\mathbf{B_0}$ inhomogeneities and susceptibility effects must also be considered when NMR signal is detected. These effects result in a quicker relaxation with time constant T_2^* which accelerates the intrinsic relaxation properties of the nuclei. Fortunately there is a straightforward technique involving spin-echoes that can remove the inhomogeneous effects while retaining the intrinsic T_2 effects [18]. The simplest method to generate a spin-echo is illustrated in Fig. 1.5.a and begins by applying a 90° pulse along the $-x$-axis thereby tipping the magnetization into the $+y$ direction. This is followed by

a delay TE/2 during which phase coherence will slowly be lost as spins at different spatial locations will acquire different amounts of phase. After the TE/2 delay, a 180° pulse (also called a refocusing pulse) is applied in the y direction resulting in all spins being flipped about the y-axis. The 180° pulse is followed by another TE/2 delay during which each spin will acquire the exact opposite amount of phase that was acquired during the initial TE/2 period leading to a spin-echo at the echo time (TE = TE/2 + TE/2). At the echo time the only signal loss will be due to T_2 relaxation effects. Spin-echoes are useful for *in-vivo* spectroscopy as they can be used as part of the spatial localization process and can be used to measure T_2 for different resonance peaks.

The signal after a spin-echo for coupled spins is more complicated and requires a full quantum mechanical treatment. There are number of different methods including the density matrix [19] and product operator formalisms [9] that are outlined in Appendix A. The product operator formalism offers an intuitive method to visualize and predict spectra for coupled spins.

We will examine an I spin in a weakly coupled two-spin system IS (AX under Pople notation). Immediately after applying a 90° pulse the density matrix σ for I is given by:

$$\sigma(0) = I_y \tag{1.37}$$

As outlined above, the density matrix will evolve under the chemical shift and magnetic field inhomogeneities but scalar coupling must now be included for coupled spins. We have already discussed the chemical shift and magnetic field inhomogeneities above and will only concern ourselves with scalar coupling. Following the TE/2 delay we find [20]:

$$\sigma(\frac{\mathrm{TE}}{2}) = \left(I_y \cos\left(\pi J_{IS} \frac{\mathrm{TE}}{2}\right) - 2 I_x S_z \sin\left(\pi J_{IS} \frac{\mathrm{TE}}{2}\right)\right) \mathrm{e}^{-\mathrm{TE}/2T_2} \tag{1.38}$$

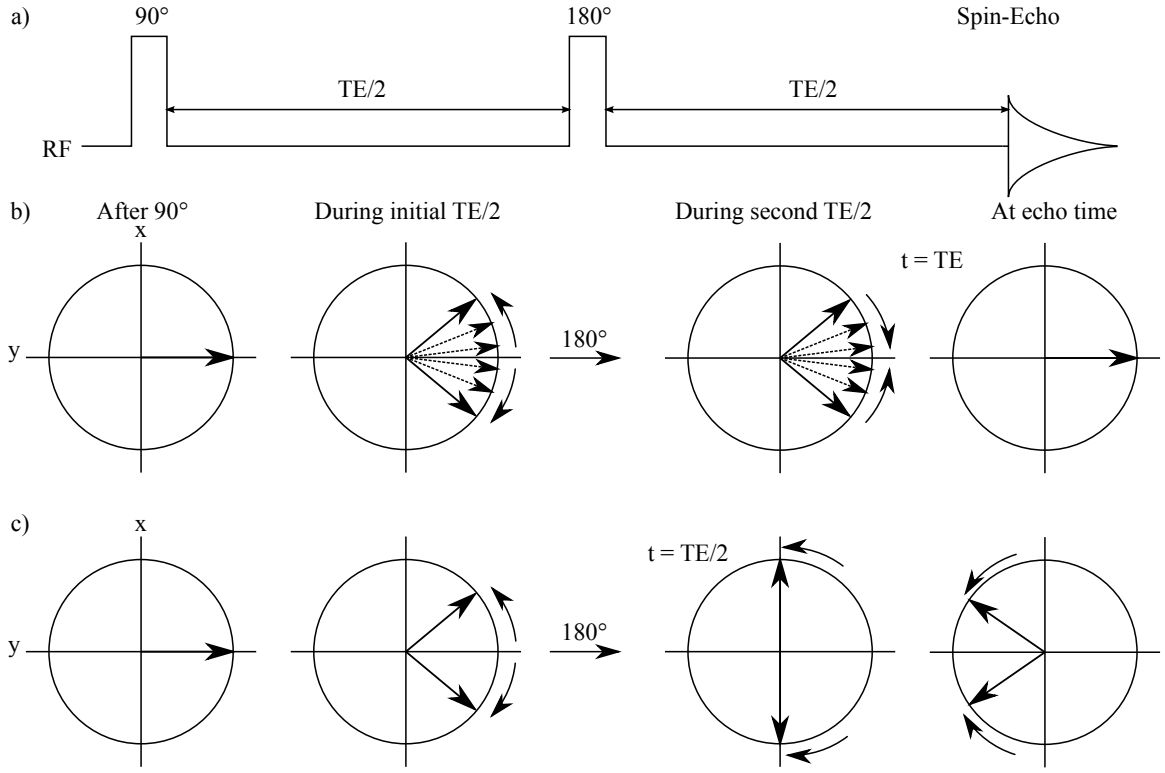


Figure 1.5: Pulse sequence diagram for a spin-echo experiment (a) as well as spin-echo formation for (b) uncoupled and (c) coupled spins. For the uncoupled case dephasing that occurs during the first TE/2 period is refocused following a 180° pulse and another TE/2 delay. For the coupled case, the 180° pulse flips the spins but also changes the direction of phase rotation. This results in an echo time dependent net phase difference at the echo time.

where J_{IS} is the coupling constant between spins I and S and $2I_xS_z$ is the anti-phase coherence of spin I. Due to the coupling between the spins, the 180° pulse not only flips the spins about y, it changes the direction of phase rotation of the accumulated phase - thereby having no overall effect on the density matrix of I. Hence the scalar coupling continues to evolve in the same fashion for the second TE/2 period resulting in:

$$\sigma(\mathrm{TE}) = \left(I_y \cos\left(\pi J_{IS}\mathrm{TE}\right) - 2I_xS_z \sin\left(\pi J_{IS}\mathrm{TE}\right)\right) \mathrm{e}^{-\mathrm{TE}/2T_2} \tag{1.39}$$

at $t = \mathrm{TE}$. Note that following the same treatment for the S spin would give the equivalent result. An illustration of the difference between the coupled and uncoupled cases is shown in Fig. 1.5.b and 1.5.c. Eq. 1.39 expresses that following a spin-echo, coupled spins will contain magnetization in the y direction and an anti-phase coherence - both of which are oscillating with the echo time resulting in so-called J-modulation. The impact of J-modulation on the I peak for an IS spin system is illustrated for a number of echo times in Fig. 1.6.

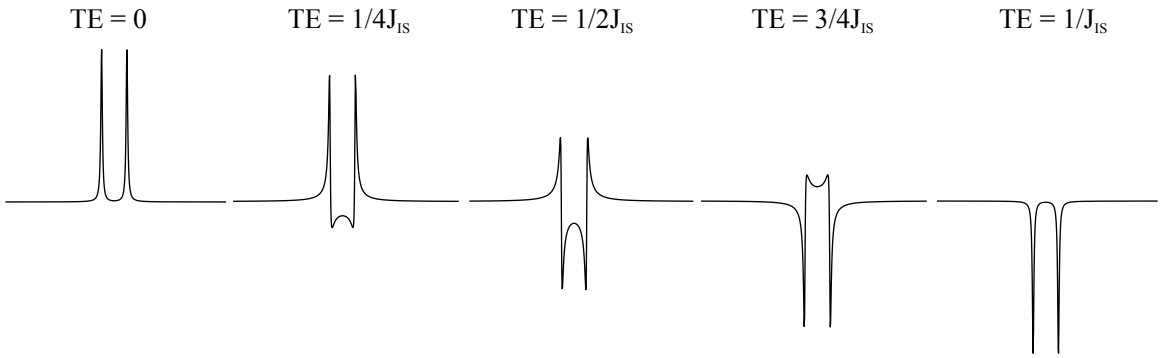


Figure 1.6: Behaviour of I resonance for a weakly coupled IS spin system at different echo times.

Chapter 2

In-Vivo ^{1}H Magnetic Resonance Spectroscopy of the Brain

The ^{1}H nucleus has the highest sensitivity for MRS due to its high gyromagnetic ratio and high natural abundance. As virtually all *in-vivo* compounds contain protons, ^{1}H spectroscopy can measure a wide range of biologically and medically meaningful compounds. There are a number of challenges that must be overcome before a useful spectrum can be generated in the brain. First, the signal must be spatially localized to a volume of interest (VOI) otherwise the spectrum will be a blurred average over the whole head giving no specific information on the local microscopic environment. As the concentration of water is several orders of magnitude greater than brain metabolites, the water signal must be removed or suppressed in order to measure metabolites accurately. Lipids and other large broad resonances must also be minimized or carefully modeled otherwise they contaminate the spectra. Finally, magnetic field heterogeneities over the VOI must be reduced in order to avoid signal loss and maintain narrow linewidths for better resolution.

2.1 Hardware and Radio-frequency Pulses

The central component of an MR scanner used for *in-vivo* spectroscopy is a powerful solenoidal, superconducting electromagnet which produces the static and spatially homogeneous $\mathbf{B}_0$ field. In addition to this magnet there are three additional pairs of field-generating coils, generally called magnetic field gradients, that are designed to produce linear modifications to $\mathbf{B}_0$ in any arbitrary direction. Yet another set of field-generating coils, called shim coils, are also included in order to correct any local inhomogeneities in $\mathbf{B}_0$ (see Sec. 2.8). In addition to the magnetic field gradients and shim coils are radio-frequency (RF) coils designed to generate an additional magnetic field $\mathbf{B}_1$. $\mathbf{B}_1$ can be further be decomposed into the $\mathbf{B}_1^+$ or transmit and $\mathbf{B}_1^-$ or receive but for now we will ignore the $\mathbf{B}_1^-$ component. $\mathbf{B_1}$ is designed to perturb the equilibrium magnetization from the longitudinal direction into the transverse plane where it can be detected as an induced signal in an adjacent receiver coil. For high resolution brain studies there are usually a number of receiver coils placed around the head.

The simplest method of manipulating spins involves application of a short, intense (square or hard) pulse which can be described using the Bloch equations in the rotating frame (Eq. 1.26). When off-resonance $\Delta\Omega$ effects can be ignored (*i.e.* the difference between the Larmor frequency ω_0 and frequency of the RF pulse ω_{RF} is small) then a hard pulse will tip the magnetization an angle θ given by:

$$\theta = \gamma \mathrm{B}_1 \tau \tag{2.1}$$

where τ is the pulse length. When off-resonance effects cannot be ignored (as is commonly the case *in-vivo*) the magnetization will not rotate about B_1 but about an

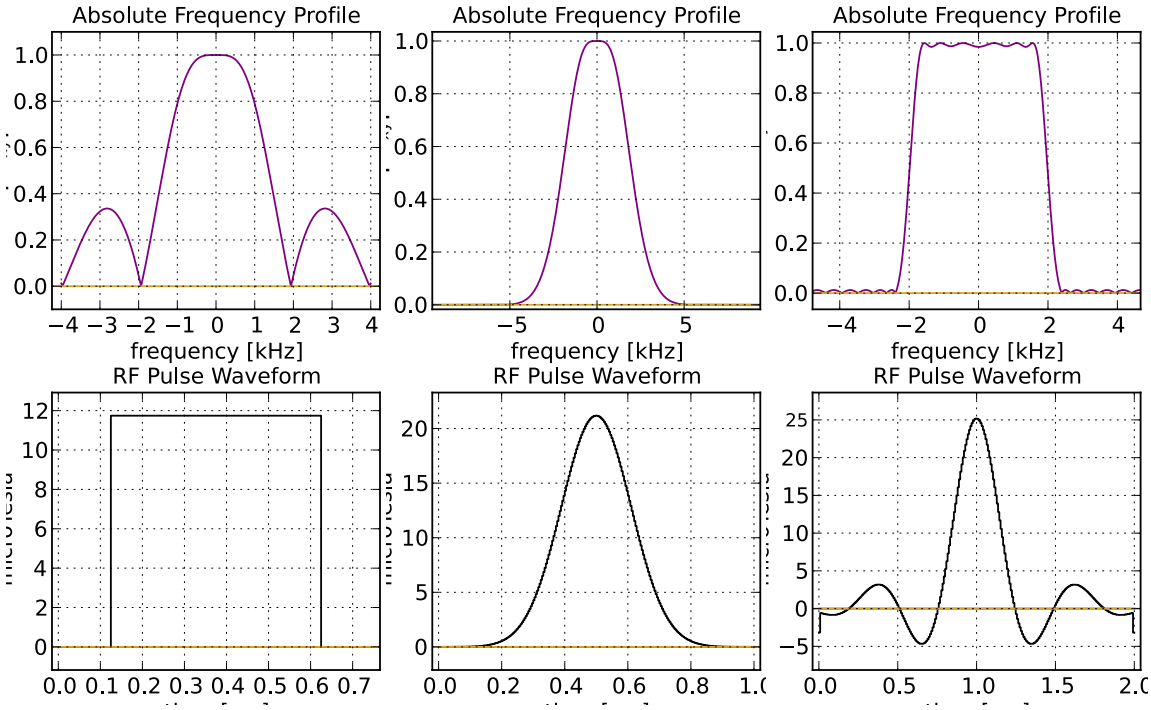


Figure 2.1: Excitation RF pulse shapes and their associated simulated frequency profiles. Left: Hard or square pulse. Center: Gaussian pulse. Right: Sinc pulse.

effective field B_{eff} with amplitude:

$$B_{eff=}\sqrt{B_1^2 + \left(\frac{\Delta\Omega}{\gamma}\right)^2} \tag{2.2}$$

with tip angle now dependent on the effective field:

$$\theta = \gamma B_{eff}\tau \tag{2.3}$$

The tip direction is also no longer necessarily towards the transverse plane as B_{eff} can point in the longitudinal direction. Visualizing off-resonance effects and predicting the effects of more sophisticated pulses is often performed with numerical simulations of the Bloch equations. Simulations are usually performed by breaking down complicated pulses into a series of short hard pulses and solving the Bloch equations at each time point. Fig 2.1 shows Bloch simulations for a hard pulse and two other common

pulse types. The product of the bandwidth BW of a pulse (the full width at half maximum of $M_{xy}(\Omega)$) and pulse length τ is the so-called "time-bandwidth product R" and is constant for a given pulse type and nominal flip angle [9]. A common pulse shape is the sinc function due to its desirable frequency profile (see Sec. 2.2). The R values for a 90° hard pulse and sinc pulse are 1.37 and 5.98 respectively therefore for a given pulse duration the BW of a sinc pulse will be 4.4 times wider. Regrettably this extra selectivity comes at a price; the peak B_1 amplitude for a sinc pulse is 5.7 times larger than for a hard pulse of equivalent BW. One must weigh the costs and benefits of different pulse shapes when designing experiments as different pulse shapes are suited to different applications.

2.2 Magnetic Field Gradients and Slice Selection

Spatial localization is generally accomplished for both *in-vivo* MRS and MRI by applying an additional magnetic field called a magnetic field gradient $\mathbf{G}$ in order to make different spatial locations resonate with different frequencies. The simplest method to accomplish this is to have $\mathbf{G}$ generate a magnetic field that varies linearly in each dimension:

$$\mathbf{G} = \begin{pmatrix} G_x \\ G_y \\ G_z \end{pmatrix} = \begin{pmatrix} \mathrm{d}B_z/\mathrm{d}x \\ \mathrm{d}B_z/\mathrm{d}y \\ \mathrm{d}B_z/\mathrm{d}z \end{pmatrix} \tag{2.4}$$

so that the magnetic field experienced by a spin at location r is:

$$\mathbf{B_z}(r) = \mathrm{B}_0 + \mathbf{r} \cdot \mathbf{G} \tag{2.5}$$

Note that both the static magnetic field B_0 and $\mathbf{G}$ are *always* pointed in the z direction and that the gradient axis refers to the direction in which the gradient varies (in reality this is not actually possible due to concomitant, or Maxwell, fields [21, 22]). In the

presence of magnetic field gradients the resonance condition (Eq. 1.7) is now:

$$\omega(\mathbf{r}) = \gamma \mathrm{B}_0 + \gamma \mathbf{r} \cdot \mathbf{G} \tag{2.6}$$

which gives the desired spatial dependence of the resonance frequency.

A spatial slice of spins can be selectively excited by the combination of an RF pulse and a magnetic field gradient. When an RF pulse that is designed to excite only a selective frequency range is applied simultaneously with the magnetic field gradient, only a selective range of frequencies, and hence positions, is excited. Slice selective pulses are generally designed to approximate a rect (or boxcar) function in the frequency domain so that spins outside the range of desired frequencies are left untouched. For small flip angles there is a Fourier relationship between the shape of the RF pulse and the resulting excitation profile. Hence a sinc shaped RF pulse will generate the desired rect excitation profile. Due to finite RF pulse durations, the truncation of the sinc function will not result in an ideal rect profile as shown in Fig. 2.2.a. The carrier frequency of the RF pulse determines the slice position while the RF bandwidth and gradient strength determine the slice thickness. An illustration of slice selection in the z direction is shown in Fig. 2.2.b. Note that only 1 dimension can be selected at a time using conventional linear magnetic field gradients and so other techniques must be employed to localize the acquired signal into other geometries (column, cube, sphere, etc.).

The spatial position of a slice selected in this method will be linearly affected by the chemical shift of the resonances under examination. If we rearrange Eq. 2.6 and examine only the z components we can find:

$$z = \frac{\omega(z) - \omega_0}{\gamma \mathrm{G_z}} \tag{2.7}$$

Hence two different resonance frequencies $\Delta\omega$ result in a spatial displacement δz of

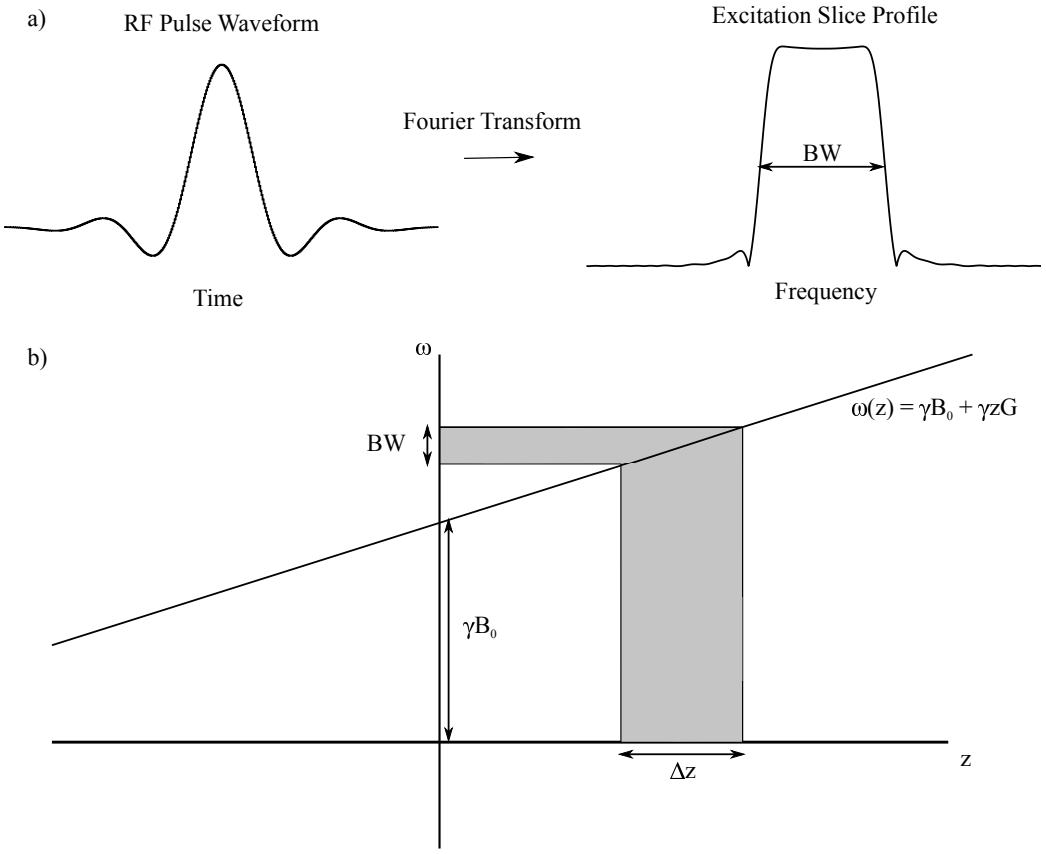


Figure 2.2: a) Truncated sinc pulse and resulting excitation profile. b) Principle of slice selection for a magnetic field gradient in the z direction. A selective range of spins are excited by a frequency-selective RF pulse.

the localized volume between them:

$$\delta \mathrm{z} = \frac{\Delta\omega}{\gamma \mathrm{G_z}} \tag{2.8}$$

and as the gradient strength required to select a region Δz is proportional to the BW:

$$\delta z = \frac{\Delta\omega}{\mathrm{BW}} \Delta z \tag{2.9}$$

Hence a smaller pulse bandwidth will generate a larger chemical shift displacement error (CSDE).

2.3 Phase Encoding

Magnetic field gradients can also be used to *phase-encode* a spatial location. This is done by turning a linear gradient on for a short period after excitation before turning it off again so that each spin will acquire a spatially dependent phase. The spins at position $\mathbf{r}$ will acquire spatially dependent phase ϕ:

$$\phi(\mathbf{r}, t) = \gamma \mathbf{r} \cdot \int \mathbf{G}(t) \mathrm{d}t \tag{2.10}$$

which for a constant gradient simplifies to:

$$\phi(\mathbf{r}, t) = \gamma \mathbf{r} \cdot \mathbf{G} t \tag{2.11}$$

Phase encoding is generally performed after slice selection to further localize signal. When the phase encode gradient moment is zero, the signal is untouched. When the phase encode gradient moment is non-zero, signal in the direction of the phase encode gradient will experience a linear phase shift leading to signal cancellation and signal loss along that direction thereby distorting the acquisition. We can extract the

location dependent phase by repeating the experiment a number of times as the real and imaginary signal for each peak will modulate as a function of the phase encode gradient amplitude so that now Eq. 1.30 becomes:

$$\begin{aligned} \mathrm{Re}\{S(\omega,\mathbf{r})\} &= \mathrm{A}(\omega)\cos\phi(\mathbf{r}) - \mathrm{D}(\omega)\sin\phi(\mathbf{r}) \\ \mathrm{Im}\{S(\omega,\mathbf{r})\} &= \mathrm{A}(\omega)\sin\phi(\mathbf{r}) + \mathrm{D}(\omega)\cos\phi(\mathbf{r}) \end{aligned} \tag{2.12}$$

To illustrate, consider a hypothetical experiment when 3 different compounds, denoted A, B and C with chemical shifts of 1, 2, and 3 ppm respectively, that have been placed separately at unknown locations along an axis as shown in Fig. 2.3. If we acquire signal with a number of phase encoding steps we see that the B resonance does not modulate for different phase encode steps and can therefore conclude that, according to Eq. 2.12, B must be located at $\mathbf{r} = 0$. The other two peaks are a bit more complicated but we can conclude that they are on opposite sides of B as they acquire opposite phase and that A must be further away than C as it acquires phase quicker.

To quantitively determine the spatial locations we note that the total spectrum of our samples (Eq. 1.29) also equals the sum of the individual spectra elements $s(\mathbf{r},\omega)$:

$$S(\omega) = \int_{-\infty}^{\infty} s(t)\mathrm{e}^{-i\omega t}\mathrm{dt} = \int_{-\infty}^{\infty} s(\mathbf{r},\omega)\mathrm{d}\mathbf{r} \tag{2.13}$$

If we include a phase gradient and combine Eq. 2.11 and 2.13 we find:

$$S(\mathbf{G},\omega) = \int_{-\infty}^{\infty} s(\mathbf{r},\omega)\mathrm{e}^{i\gamma\mathbf{r}\cdot\mathbf{G}t}\mathrm{d}\mathbf{r} \tag{2.14}$$

This is simply the inverse Fourier transform of $s(\mathbf{r},\omega)$ so we can invert this equation and find signal from individual elements $s(\mathbf{r},\omega)$ by taking the Fourier transform of

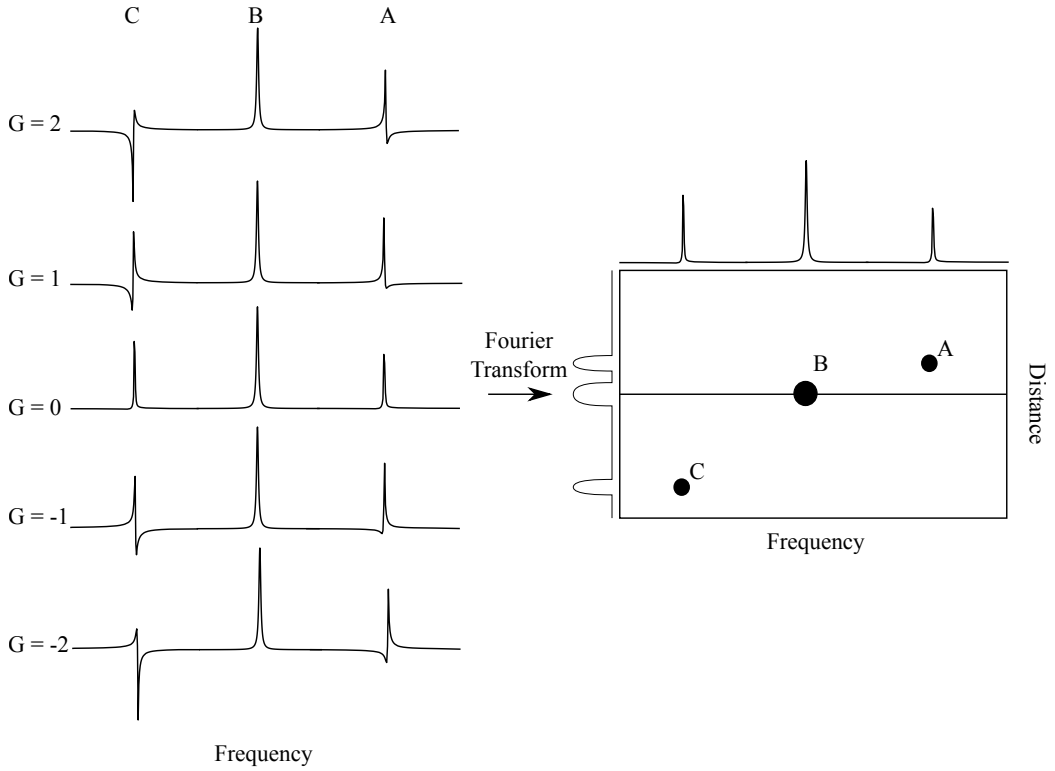


Figure 2.3: Diagram of the principle behind phase encoding for spatial localization of resonance peaks. Peaks at different spatial locations will acquire different phases when a phase encode gradient **G** is applied. After a number of **G** iterations, Fourier transform with respect to the phase-encoding gradient reveals the spatial distribution of the compounds.

$S(\mathbf{G}, \omega)$:

$$s(\mathbf{r}, \omega) = \int_{-\infty}^{\infty} S(\mathbf{G}, \omega) e^{-i\gamma \mathbf{r} \cdot \mathbf{G} t} \mathrm{d}\mathbf{G} \tag{2.15}$$

Eq. 2.15 suggests that we are continually sampling the phase encode gradient strength $\mathbf{G}$ but in reality we must use a discrete Fourier transformation. The number of phase encoding steps determines the digitization rate and is governed by the Nyquist–Shannon sampling theorem which bridges the gap between continuous and discrete signals [23, 24]. The Nyquist–Shannon criterion requires that the maximum phase shift difference between gradient increments over the entire region or field of view (FOV) be 2π:

$$2\pi = \gamma \mathrm{FOV} \Delta \mathrm{G} t \tag{2.16}$$

or alternatively:

$$\frac{1}{\mathrm{FOV}} = \frac{\gamma \Delta \mathrm{G} t}{2\pi} \tag{2.17}$$

2.4 Single Voxel Localization Techniques

Modern MRS experiments are conducted by employing a series of pulses to manipulate the magnetization as desired. These pulse sequences range from a simple one pulse experiment or the aforementioned spin-echo sequence, to sophisticated sequences employing hundreds of pulses. One critical requirement for *in-vivo* spectroscopy is three dimensional spatial localization in order to remove unwanted signals from outside the VOI. Localization is generally performed by a localization pulse sequence.

2.4.1 PRESS

One of the most common techniques for acquiring single-voxel localized spectra is the Point REsolved SpectroScopy (PRESS) sequence [25]. The sequence is illustrated in Fig. 2.4 and begins with a slice selective excitation pulse followed by two slice

selective refocusing pulses selecting orthogonal directions. The first two pulses form a spin-echo as outlined in Sec. 1.6 but because the slice selection direction for the two pulses is orthogonal, only spins found in a column at the intersection between the two slices will be refocused. The final pulse selects the remaining dimension and refocuses the spins in a voxel at the intersection between all three pulses at the echo time.

Signal will be generated by each of the applied pulses but only signal located at the intersection of all three pulse is of interest - the remaining signals must be removed. This is accomplished with magnetic field gradients. A short pulse of a linear magnetic field gradient will induce a spatially dependent phase. To remove unwanted FID or spin-echo signals, pairs of equal amplitude gradients are placed on either side of the refocusing pulses. As Eq. 2.11 suggests, the initial gradient imparts a phase and, after a 180° pulse, the second gradient will completely refocus the effects of the initial gradient for excited spins. Signal is crushed for any spins that were not excited by the initial 90° pulse and that subsequently experienced the 180° pulses.

As shown in Section 2.2, slice selection via a slice selective RF pulse and magnetic field gradient will result in a chemical shift displacement error (CSDE). For uncoupled spins this can be extended to two or three dimensions such that the selected voxel is slightly offset for each resonance peak. For coupled spins this is more complicated due to the so-called four-compartment artifact [26]. Fig. 2.5 illustrates the effect from the two PRESS refocusing pulses for the A spins in an AX spin system. In the V_1 region both spin species (A, X) will experience the desired selective pulses. In V_2, V_3, and V_4 however, the A spins are outside the X voxel and therefore the pulses will selectively refocus only the A spins. Using the product operator formalism (ignoring relaxation) and assuming that the density matrix after excitation is $\sigma = A_y$, we find

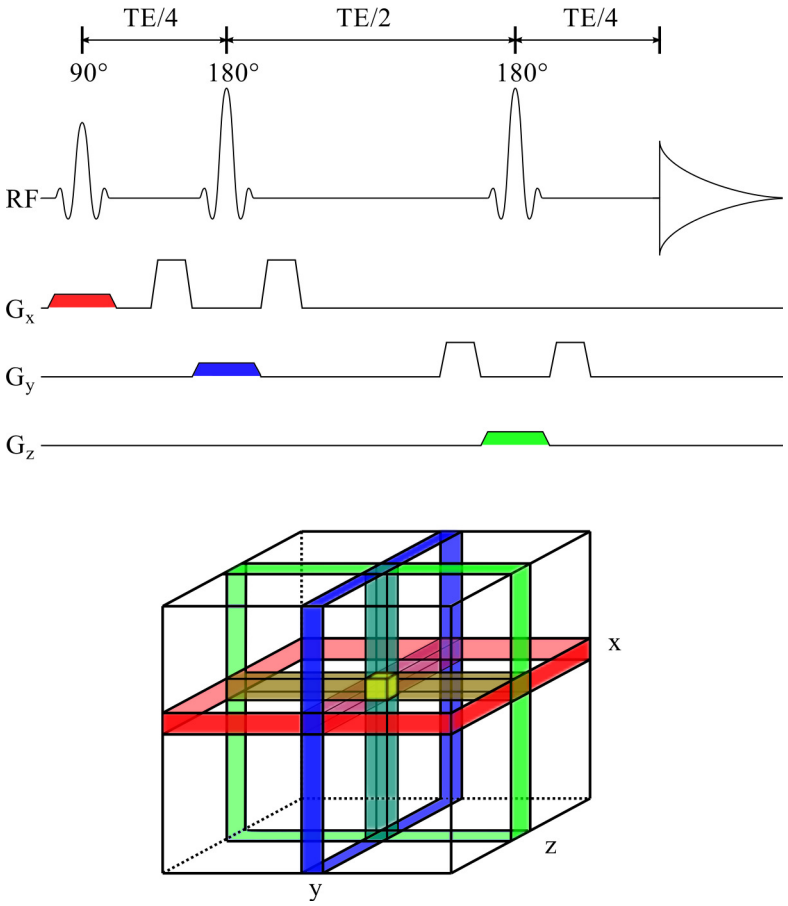


Figure 2.4: Top: PRESS pulse sequence diagram for 3D localization. Bottom: Three orthogonal slice selective pulses select a voxel (yellow) at the echo time with crusher gradients surrounding each refocusing pulse to remove unwanted signal from outside the voxel of interest.

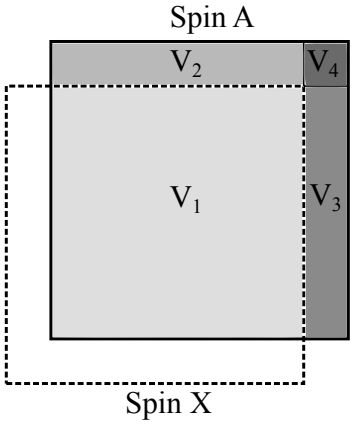


Figure 2.5: Four-compartment artifact due to chemical shift displacement error during PRESS localization on scalar coupled spins.

that for the 4 regions we have:

$$\begin{aligned}
\mathrm{V}_1 \rightarrow &\quad A_y \cos\left(\pi J_{AX} \mathrm{TE}\right) - 2A_x X_z \sin\left(\pi J_{AX} \mathrm{TE}\right) \\
\mathrm{V}_2 \rightarrow &\quad A_y \cos\left(\pi J_{AX} \frac{\mathrm{TE}}{2}\right) - 2A_x X_z \sin\left(\pi J_{AX} \frac{\mathrm{TE}}{2}\right) \\
\mathrm{V}_3 \rightarrow &\quad A_y \cos\left(\pi J_{AX} \frac{\mathrm{TE}}{2}\right) - 2A_x X_z \sin\left(\pi J_{AX} \frac{\mathrm{TE}}{2}\right) \\
\mathrm{V}_4 \rightarrow &\quad A_y
\end{aligned} \tag{2.18}$$

That is, in region V_1, the A spins will experience scalar coupling for the complete echo time as expected. For regions V_2 and V_3, A spins will evolve only under J-modulation for half the echo time and in V_4 the J-modulation is completely refocused. Hence when we acquire our signal, the A doublet will undergo an extra interference over and and beyond the sinusoidal J-modulation.

There are a number of ways of minimizing the CSDE. The most obvious method is to increase the RF pulse bandwidth by decreasing the pulse length; though regrettably this also drastically increases the required RF power and this quickly becomes too large or is unachievable using the hardware for *in-vivo* experiments. As a lower flip angle requires a lower RF power (and hence can achieve a larger BW), the refocusing pulses always produce a larger CSDE than the excitation pulse. Another approach is to acquire short-echo time spectra so that the effects of scalar coupling are minimized. This also has the added benefit of reducing signal loss due to relaxation.

2.4.2 STEAM

Most of the problems associated with PRESS can be attributed to the 180° refocusing pulses and by replacing the refocusing pulses with 90° pulses, one can reduce the associated errors. Stimulated Echo Acquisition Mode (STEAM) is a localization technique that does exactly this. Three 90° pulses generate a number of coherences: three direct FIDs (FID1, FID2, FID3), four spin echoes (SE12, SE123, SE23, SE13)

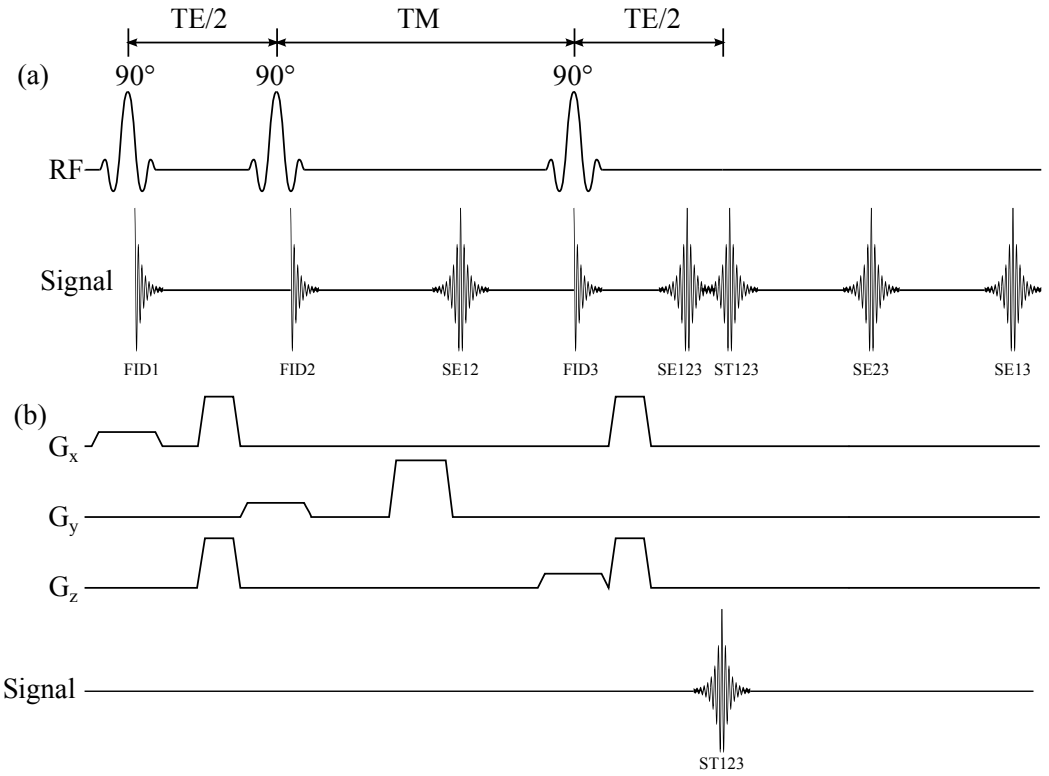


Figure 2.6: STEAM pulse sequence diagram for 3D localization and signal generation. (a) without crusher gradients, (b) with crusher gradients

and one so-called stimulated echo (ST123) as illustrated in Fig. 2.6. As we generally desire the ST123 coherence, we remove the spin-echo coherences by employing a gradient during the so-called mixing time (TM) which crushes all the spin-echoes. The FIDs are removed by employing crusher gradients during each TE/2 period. As illustrated at the bottom of Fig. 2.6, the only remaining signal is the stimulated echo.

The generation of a stimulated echo differs from a spin-echo and theoretically contains only 50% of the signal intensity of PRESS. This is because the second 90° pulse rotates half of the transverse magnetization back to the longitudinal axis while the other half is crushed by the mixing time crusher gradient. A characteristic of stimulated echoes is that the magnetization is tipped back to the longitudinal axis during the mixing time, during which magnetization will under go T_1 relaxation but not T_2 relaxation. As $T_1 \geq T_2$, the signal remains relatively stable during the mixing

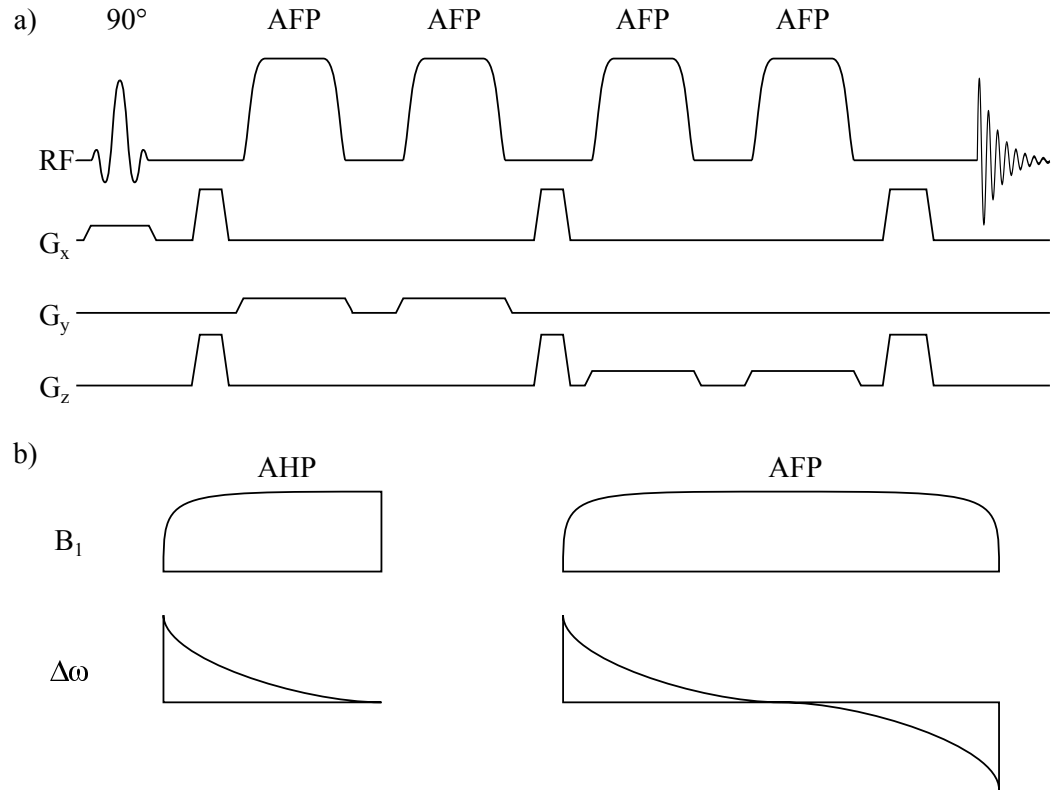


Figure 2.7: a) semi-Laser pulse sequence diagram for 3D localization. b) Adiabatic half passage (AHP) and full passage (AFP) pulses.

time allowing for optimized timing schemes [27] and/or diffusion measurements [28].

2.4.3 semi-LASER

Another alternative to PRESS and STEAM is the semi-Localization by Adiabatic SElective Refocusing (semi-Laser) sequence. semi-Laser replaces the refocusing pulses of PRESS with pairs of adiabatic full passage (AFP) pulses as illustrated in Fig. 2.7.a [29]. As described in Sec. 2.4.1, conventional 180° refocusing pulses produce a large CSDE. Additionally, due to practical limitations of transmit coils used for *in-vivo* spectroscopy, generated B_1 magnetic fields may be relatively inhomogenous leading to increased signal loss. Adiabatic pulses solve both these problems as they generate a uniform flip angle independent of the B_1 amplitude (above a threshold) and can achieve a much larger bandwidth than conventional pulses [30, 31].

Adiabatic pulses modulate not just the RF amplitude but also the frequency (or phase). Visualizing how this accomplishes the desired outcome is best done in a rotating frame (x', y', z') rotating at instantaneous frequency $\boldsymbol{\omega_{rf}}(t)$ so that $\mathbf{B}_1(t)$ remains fixed throughout the pulse. In this frame (denoted the frequency-modulated frame FM), whenever the frequency deviates from the Larmor frequency, an additional magnetic field is introduced in the z-axis equal to $\boldsymbol{\Delta\omega}/\gamma$ where $\boldsymbol{\Delta\omega} = \omega_0 - \boldsymbol{\omega_{rf}}(t)$. For conventional pulses, $\Delta\omega$ is constant and describes the effects of a pulse being off-resonance, but for adiabatic pulses $\boldsymbol{\Delta\omega}$ is a vector and hence the effective field $\mathbf{B}_{\text{eff}}(t)$ is the vector sum of $\mathbf{B}_1(t)$ and $\boldsymbol{\Delta\omega}/\gamma$:

$$\mathrm{B}_{\text{eff}}(t) = |\mathbf{B}_{\text{eff}}(t)| = \sqrt{\mathbf{B}_1(t)^2 + \frac{\boldsymbol{\Delta\omega}}{\gamma}} \tag{2.19}$$

As both $\mathbf{B}_1(t)$ and $\boldsymbol{\Delta\omega}$ change throughout the pulse, $\mathbf{B}_{\text{eff}}(t)$ changes its orientation at the instantaneous angular velocity $\frac{\mathrm{d}\alpha}{\mathrm{d}t}$:

$$\alpha = \arctan\left(\frac{\gamma\mathbf{B}_1(t)}{\Delta\omega(t)}\right) \tag{2.20}$$

As illustrated in Fig. 2.7.b, at the beginning of an adiabatic pulse, $\boldsymbol{\Delta\omega}$ is at its maximum value and $\boldsymbol{\Delta\omega}/\gamma$ is very large relative to $\mathbf{B_1}$. Hence, initially $\mathbf{B}_{\text{eff}}(t)$ is oriented approximately in the z'-axis. As $\boldsymbol{\omega_{rf}}(t)$ increases and $\boldsymbol{\Delta\omega}/\gamma$ decreases, $\mathbf{B}_{\text{eff}}(t)$ therefore rotates toward the transverse plane (in the direction of $\mathbf{B}_1(t)$). A so-called adiabatic half passage occurs when $\boldsymbol{\Delta\omega} = 0$ (90° excitation) and an adiabatic full passage AFP (180° inversion) occurs after a full frequency sweep when $\boldsymbol{\Delta\omega}_{final} = -\boldsymbol{\Delta\omega}_{initial}$. During an adiabatic pulse, the magnetization vector $\mathbf{M}$ follows $\mathbf{B}_{\text{eff}}(t)$ if the adiabatic condition:

$$|\gamma\mathbf{B}_{\text{eff}}(t)| \gg |\frac{\mathrm{d}\alpha}{\mathrm{d}t}| \tag{2.21}$$

is satisfied for all t. The maximum frequency modulation $\boldsymbol{\Delta\omega}_{max}$ of an AFP pulse

is directly related to the bandwidth, allowing for larger bandwidths compared with conventional pulses. Eq. 2.19 also reveals that adiabatic pulses are insensitive to $\mathbf{B_1}$ inhomogeneity when $\boldsymbol{\Delta\omega} = 0$ (90° excitation) as the direction of $\mathrm{B_{eff}}(t)$ now equals that of $\mathbf{B}_1(t)$ or when $\boldsymbol{\Delta\omega}$ is large compared with $\mathbf{B}_1(t)$ (180° inversion). Regrettably AFP pulses introduce a non-linear phase shift as the phase of the resultant magnetization varies as a function of ω_0 and B_1 amplitude. As such, for the semi-Laser pulse sequence, pairs of AFP pulses are employed with opposite frequency sweeps to refocus any phase shifts created by the pulses. The main disadvantage of semi-Laser is that the RF energy deposited by adiabatic pulses is generally much larger than conventional pulses and this limit the experimental flexibility for *in-vivo* applications.

2.5 Water Suppression

The water peak overwhelmingly dominates *in-vivo* ^{1}H spectra due to its high concentration (about 80% of wet weight in brain). Water resonates at 4.65 ppm (relative to NAA, see Sec. 2.6.1) and, when unsupressed, distorts the signal baseline and overlaps virtually all other relevant metabolite peaks resulting in unreliable metabolite detection. Suppressing the water signal removes the distortions and allows reliable metabolite measurements. There are number of methods to suppress water signal during acquisition including WATERGATE [32], WEFT [33], DEFT [34], CHESS [35] and VAPOR [27]. If the water suppression does not completely remove the water signal, filter methods during post-processing can be used to reduce the signal further. For *in-vivo* applications, CHESS and VAPOR sequences have proven to be very effective and relatively robust for small regions. CHESS involves application of a frequency selective excitation pulse that selects only resonances around 4.65 ppm. After excitation of the water signal, a crusher gradient is employed to dephase the water coherences in the transfer plane. As CHESS pulses depend on precise frequency

profiles and must flip all the water signal in the voxel of interest, B_0 and B_1 must be very homogenous otherwise residual water will remain in the acquired spectrum. Fortunately CHESS pulses can be applied more than once in order to increase the water suppression efficiency. VAPOR optimizes regular CHESS pulses by carefully setting delays between seven CHESS pulses in order to exploit differences in T_1 relaxation between water and other resonances resulting in robust water suppression that is less sensitive to B_1.

2.6 Metabolites

Once a localized, water suppressed ^{1}H spectrum has been acquired, a large number of biologically important compounds can be observed and quantified in the brain. These include alanine, aspartate, *N*-acetylaspartate, *N*-acetylaspartylglutamate, creatine, phosphocreatine, glutamate, glutamine, γ-aminobutyric acid, glycine, choline, phosphocholine, glycerophosphorylcholine, *myo*-inositol, *scyllo*-inositol, taurine, glutathione, glucose and lactate. A few important metabolites have been highlighted in the follow sections.

2.6.1 *N*-Acetylaspartate

The most prominent resonance peak for healthy brain *in-vivo* ^{1}H spectra (besides water) is the methyl group of *n*-acetylaspartate (NAA) at 2.01 ppm. NAA also has less prominent coupled resonance peaks at 2.49, 2.67 and 4.38 ppm. NAA is present in concentrations of approximately 12 mM in the human brain - making it one of the most highly concentrated metabolites [36]. NAA exists primarily in the neurons, some dendritic processes and in most axon fiber pathways [37]. NAA provides one of the most reliable markers for neuronal health and integrity. Unfortunately, this is not based on a full understanding of the functions of NAA but on consistent empirical

evidence showing a decrease in NAA in schizophrenia [38], severe brain injury [39], stroke [40], epilepsy [41], multiple sclerosis [42] and Alzheimer's disease [43] or an increase in NAA in Canavan's disease [44]. NAA has a variety of functions including serving as precursor for the biosynthesis of *N*-acetylaspartylglutamate (NAAG) - one of the most prevalent and active neurotransmitters [45]. Other proposed functions of NAA are still up for debate and include playing a role in brain nitrogen balance and in central nervous system fatty acid and steroid synthesis [46].

2.6.2 Creatine and Phosphocreatine

Besides NAA, the largest resonance peak usually corresponds to the singlet resonances at 3.03 and 3.93 ppm of the methyl and methylene groups of creatine (Cr) and phosphocreatine (PCr) usually referred to as total creatine (tCr). Creatine is present in most metabolically active tissue such as muscle, heart and brain. Quantification of tCr is not only valuable in its own right as a fundamental component of phosphate metabolism but also as a reference compound to quantify other metabolites as tCr concentrations remain relatively stable in healthy [47] and many pathologic states [48]. Expressing metabolite concentrations as ratios (with tCr as the denominator) is very common as any error associated with localization or local inhomogeneity is assumed to be equal for all metabolites and therefore relative concentrations of metabolites from the same spectra are self-corrected. This assumption must be taken with caution as it has been shown that using tCr ratios for relative concentrations can introduce additional variability [49]. More accurate absolute quantification is performed with an additional water unsupressed acquisition as outlined in Sec. 2.9.

2.6.3 Glutamate and Glutamine

Glutamate (Glu) and glutamine (Gln) are two structurally similar amino acids and, at field strengths of ≤ 3 T, have overlapping peaks and have therefore traditionally

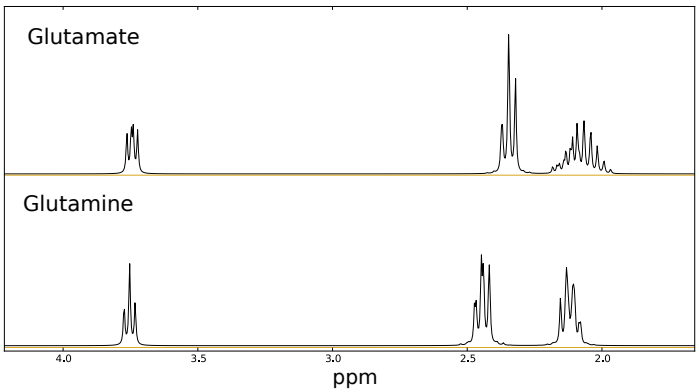


Figure 2.8: Simulated ^{1}H spectrum of glutamate and glutamine. Glutamine also has resonances downfield from water (not shown).

been measured together as combined Glx resonances. At magnetic field strengths of 7 T or higher, the resonances around 2.45 ppm begin to move apart and Glu and Gln can be quantified separately. The resonances for both Glu and Gln are strongly coupled and form a number of low intensity peaks as illustrated in Fig. 2.8. Glu has a variety of important biological roles including being the primary excitatory neurotransmitter in the central nervous system, a source of energy and ammonia, an important component in the synthesis of many metabolites including γ-aminobutyric acid (GABA) and glutathione and as part of the glutamate-glutamine cycle [50, 51]. Gln is an important intermediate in neurotransmitter metabolism and ammonia detoxification [50, 52].

2.6.4 γ-Aminobutyric Acid

γ-Aminobutyric acid (GABA) has both an important role as a metabolite and as the primary inhibitory neurotransmitter within the brain. GABA has three coupled methylene groups resonating at 1.89, 2.28 and 3.01 ppm and, as all the GABA resonances overlap with other more intense signals, GABA detection can be difficult. Therefore, GABA detection is usually achieved by specialized pulse sequences employing spectral editing. One of the most widely used methods for measuring GABA

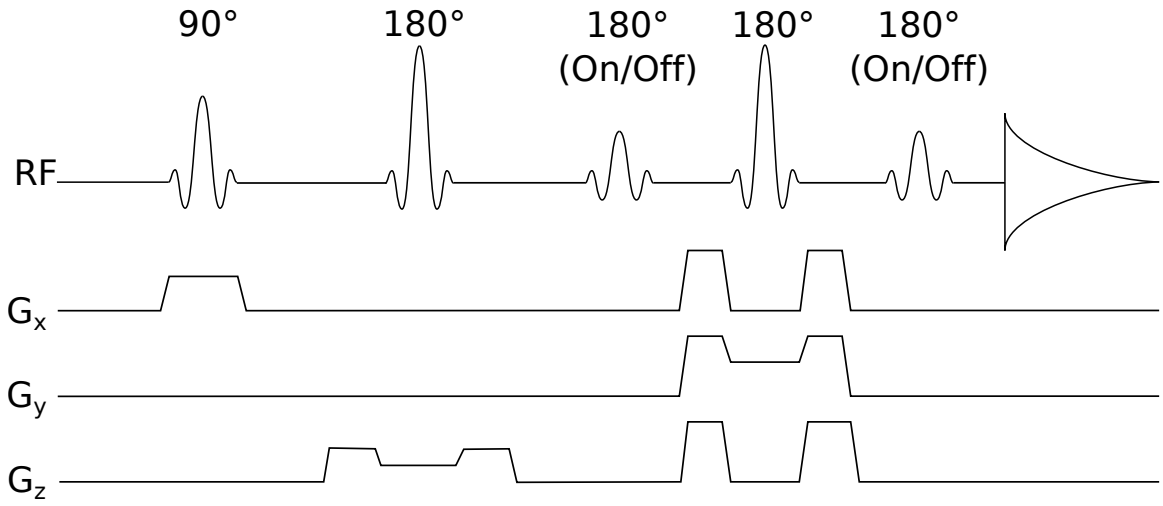


Figure 2.9: Pulse sequence diagram for MEGA-PRESS

is MEGA-PRESS (MEshcher-GArwood Point RESolved Spectroscopy) [53]. MEGA-PRESS involves acquisition of two interleaved spectra - one acquisition with two frequency selective editing pulses applied to GABA at 1.9 ppm (and therefore coupled to GABA spins at 3.0 ppm) and the other acquisition with the frequency selective pulses applied far outside the spectral range so it does not effect any relevant spins. Taking the difference of these spectra removes all the peaks except those affected by the editing pulses (GABA and Glx). Alternatively, at magnetic field strengths of 4 T or greater GABA can directly detected due to increased chemical shift resolution [54]. As MRS is the only measurement technique that allows direct, non-invasive quantification GABA *in vivo*, previous MRS studies have provided significant insights to a wide variety of neuroscience, pharmacological and clinical applications. These include, for example, shedding light on neuroplasticity [55], controlling seizures of epilepsy patients [56] and demonstrating reduced GABA concentrations in depressed subjects [57].

2.7 Macromolecules and Lipids

In-vivo ^{1}H spectra generally contain signal from both low-molecular weight metabolites as discussed above and high-molecular weight macromolecules (MM). MM signals in typical spectra arise from nuclei on the outer parts of large macromolecules or from smaller macromolecules with higher mobility. These resonances have been extensively studied and have been partly assigned to methyl and methylene resonances of amino acids in cytosolic proteins [58] - though due to their short T_2 and broad spectral signatures, they are not as well characterized as metabolites. In short TE spectra, a significant fraction of the observed signal consists of the MM resonances and failure to account for the broad MM resonances will generally lead to an overestimation of metabolite concentrations [59]. As the T_1 and T_2 relaxation times of MM signals are significantly shorter than those of the metabolites [60], one can selectively detect metabolites by acquiring spectra at long TE or detect only the MM resonances by using an inversion recovery sequence [61] with an inversion time tuned to the metabolite T_1 null. Long TE spectra suffer from severe J-modulation and therefore are only practical for quantifying uncoupled spins such as Cr or NAA.

Lipids in healthy human brain are normally very immobile and, as a result, are generally not present in *in-vivo* ^{1}H spectra. However, lipid signals may arise if either the VOI is placed too close to the scalp, allowing extra-cranial lipid signals to contaminate the spectrum, or in pathologies such as brain tumors where mobile lipids are naturally present. Just as with MM, lipids produce broad resonances that overlap metabolite resonances and can cause quantification biases.

2.8 Magnetic Field Homogeneity and Shimming

One of the most important requirements for high resolution spectroscopy is magnetic field homogeneity [9]. Modern MR scanners generate a very uniform $\mathbf{B}_0$ field but,

unfortunately, this homogeneity is compromised as soon as a subject is inserted into the magnet. The subject introduces both its own unavoidable microscopic inhomogeneities due to different tissue types and macroscopic inhomogeneities between tissue boundaries which must be reduced before acquisition. The effect of magnetic field inhomogeneity on a spectrum is most easily understood by notionally dividing up a macroscopic sample into smaller volumes such that for each smaller volume the magnetic field is constant. The signal for the total sample can then described (from Eq. 1.28):

$$\mathrm{M}_{xy} = \mathrm{M}_0 \mathrm{e}^{i\omega_0 t} \mathrm{e}^{-t/T_2} \sum_{n=1}^{N} \mathrm{e}^{i\omega_n \mathrm{t}} \tag{2.22}$$

where N is the total number of sub-volumes and ω_n is the difference in frequency in volume element n from the Larmor frequency ω_0 and T_2 is assumed to be equal for the whole volume. In a perfectly homogenous case, ω_n is equal for all volumes and each signal adds coherently resulting in a single peak. If magnetic field inhomogeneities are present, we have different ω_n and therefore the signals from each sub-volume do not add coherently resulting in a broad, irregularly shaped resonance peak.

High magnetic field homogeneity can be achieved on a subject by subject basis with active shimming. This is accomplished by magnetic field shim coils installed inside the bore of the superconducting magnetic. Shim coils are designed in such a way as to generate the basis set that is the spherical harmonic solution to Laplace's equation for the magnetic field inside the magnet [62]. On most systems different shims are referred to by their Cartesian functions as listed in Table 2.1 though most clinical human scanners do not have shim coils generating terms beyond the 2nd order. The process of shimming refers to mapping the magnetic field $\mathbf{B_0}$ and attempting to cancel any inhomogeneities with the available spherical harmonic shims. There are a number of methods for mapping the magnetic field distribution within the subject in a time efficient manner and most are based on either collecting images at different echo times (field map based, *e.g.* GRESHIM [63]) or by collecting profiles along different

Order n	Degree m	Cartesian function	Common name
0	0	1	Z^0
1	0	z	Z
1	1	x	X
1	-1	y	Y
2	0	$2z^2 - (x^2 + y^2)$	Z^2
2	1	zx	ZX
2	-1	zy	ZY
2	2	$x^2 - y^2$	$X^2 - Y^2$
2	-2	$2xy$	XY
3	0	$2z^3 - 3z(x^2 + y^2)$	Z^3
3	1	$4z^2x - x(x^2 + y^2)$	Z^2X
3	-1	$4z^2y - y(x^2 + y^2)$	Z^2Y
3	2	$z(x^2 - y^2)$	$Z(X^2 - Y^2)$
3	-2	$2zxy$	ZXY
3	3	$x(x^2 - 3y^2)$	X^3
3	-3	$y(3x^2 - y^2)$	Y^3

Table 2.1: Cartesian representation of spherical harmonics ($n \leq 3$)

directions (projection based, *e.g.* FASTMAP [64]).

2.9 Quantification

In principle, MR spectra can be used to derive absolute concentrations of metabolites *in-vivo*. This is because, as shown in Eq. 1.20, M_0 is directly proportional to the number of spins n, and hence is proportional to the molar concentration. Most quantification methods use a reference compound (*e.g.* creatine, water) of known concentration to calculate metabolite concentrations. If the requirements for accurate *in-vivo* quantification are satisfied (accurate localization, effective water suppression and high magnetic field homogeneity) then the flowchart illustrated in Fig. 2.10 shows how spectroscopy can derive MR visible concentrations.

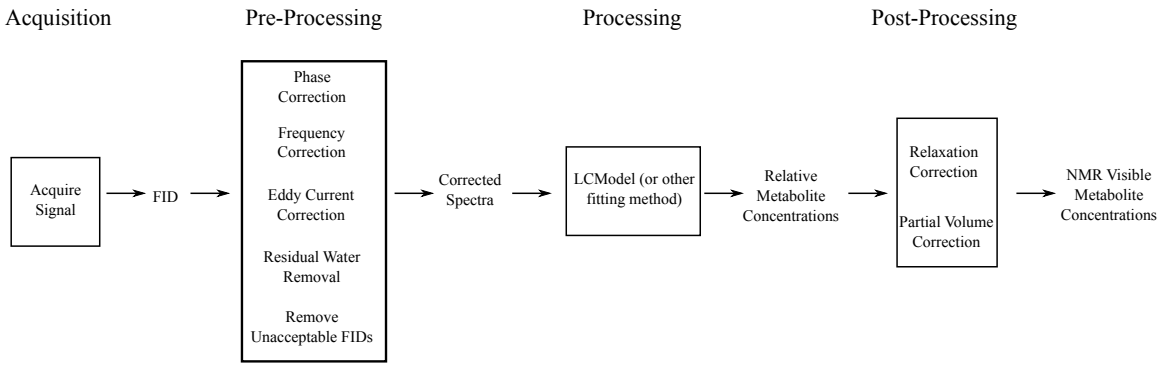


Figure 2.10: Flow chart for processing and quantification of *in-vivo* spectra. Residual water removal during pre-processing is optional.

2.9.1 Signal Averaging

The quality of NMR spectra is determined by the signal-to-noise ratio (SNR) and the line width of the resonance peaks. The SNR can be improved by averaging signal from n identical acquisitions by a factor of $\sqrt{n}$ as coherent signal will increase linearly with n but only the *power* of the noise will increase linearly with n. The time required for a single average is called the repetition time (TR) and for most *in-vivo* experiments this includes the complete pulse sequence, acquisition and any other time delays required before another acquisition starts. Due to the relatively low concentrations for relevant metabolites, *in-vivo* experiments are generally averaged as many times as experimentally practical.

2.9.2 Eddy Current Correction

Most quantification methods model the acquired signal as a sum of line shapes (Lorentzian, Gaussian or Voigt). Unfortunately, eddy currents generated due to fast switching of magnetic field gradients introduce line-shape distortion. Fortunately a simple post-acquisition method can cancel modulations arising due to residual eddy currents [65]. As eddy currents act on all resonances in the same fashion, any distortion in the time domain of an unsupressed water signal acquisition will be due to

eddy currents. Applying the opposite phase modulation will cancel the distortion on subsequent water suppressed acquisitions.

2.9.3 Residual Water Removal

When magnetic field inhomogeneity is less than perfect, residual water signal may still be present in water-suppressed metabolite spectra. When analyzing the region upfield from water (1.0-4.2 ppm), residual water can be ignored - provided that the signal does not distort the metabolite baseline. If the whole spectra range is considered or if the remaining water signal distorts the baseline, residual water signal can be removed using post-acquisition techniques. There are a number of effective techniques to remove residual water though the Hankel-Lanczos singular value decomposition (HLSVD) provides very reliable water removal and is easily automated which lends itself nicely to large datasets [66].

2.9.4 Quantification and Calibration

The next step involves estimating the relative resonance areas - as they are proportional to metabolite concentrations. Due to limited spectral dispersion and linewidths achievable *in-vivo*, reliable identification and estimation can be difficult. Hence the simple integration of spectral peaks is generally not possible and more sophisticated methods are required. There are a wide variety of spectral fitting tools and algorithms that achieve quantification including jMRUI [67], AMARES [68] and LCModel [69]. As an experimental spectrum is a superposition of each individual metabolites signal, most methods aim to reproduce the acquired signal using a linear combination of characteristic metabolite spectra. The relative weights for each metabolite therefore correspond to their relative concentrations. An accurate metabolite basis set is required and can be obtained by measurement or simulation [70].

Quantification errors encountered using LCModel are expressed as Cramér-Rao

lower bounds (CRLBs). CRLBs describe the lowest possible standard deviations of unbiased parameter estimates [71]. Generally metabolite concentrations with CRLBs $< 10\%$ are determined with acceptable precision, those with CRLBs between 10-30% should be analyzed with caution, and those with CRLBs $> 30\%$ are not reliable. However, a low CRLB is not always an indicator of accurate quantification as an inaccurate or incomplete basis set can introduce fitting biases resulting in erroneous concentrations. Metabolites with very similar chemical structures and overlapping signal (*e.g.* glutamate and glutamine) may be difficult for the fitting algorithm to separate. A correlation matrix can be used to quantitatively examine fitting relationships between metabolites. Coefficients between metabolites with values more negative than -0.5 are generally considered strongly correlated - *i.e.* the metabolites cannot be accurately determined individually and should be reported as a combined quantity (*e.g.* total creatine).

After the relative concentrations of each metabolite have been determined by a fitting algorithm, metabolite signals are compared to signal obtained from a known concentration (reference compound) using the same acquisition scheme. While an external reference of known concentration is ideal for true absolute quantification, it is more practical to use a stable internal reference compound. Water, creatine and NAA are common example compounds though in certain pathologies these concentrations could change [72]. Additionally, the concentration of internal reference compounds often change with position [73] though high resolution MRI images can be used to determine the relative presence of white matter, grey matter and cerebrospinal fluid (CSF) in order to correct for local biases.

Finally each metabolite must be corrected for transverse relaxation. Metabolite T_2 values are dependent on a variety of variables including field strength [74], brain region [75], subject age [76], and diseases [77]. As determining T_2 values would be an additional, time consuming experiment, the most pragmatic solution is to acquire

spectra using short echo-times in order to minimize T_2 differences and assume uniform metabolite relaxation. For longer echo times proper quantification can only be performed if the transverse relaxation time is known for each resonance.

Chapter 3

Ultra-High Field Spectroscopy of the Brain

3.1 Motivation for Ultra-High Field Spectroscopy

As described in Eq. 1.20, the static magnetic field strength B_0 is proportional to the overall SNR. An additional benefit of increased B_0 is increased spectral dispersion (as described in Eq. 1.34). Therefore, it is desirable to perform *in-vivo* measurements at higher magnetic field strengths in order to separate overlapping peaks (e.g. glutamate and glutamine) and decrease acquisition times. Though superconducting and direct current hybrid magnets can generate static magnetic field strengths up to 43-45 T, the size of the effective magnetic field bore must be decreased to a few dozen millimeters in order to maintain adequate field homogeneity [78] rendering it impossible for any *in-vivo* animal or human studies. In so-called 'widebore' NMR spectrometers (bore diameter $\sim$ 10 cm), field strengths up to 21.1 T can be generated [79] and have recently been applied to small rats *in-vivo* [80]. Currently, the highest field strength achievable with a bore diameter large enough for *in-vivo* human applications is 11.7 T [81]. Most standard clinical MRI scanners are either 1.5 T or 3T, though so-called

ultra-high field ($\geq$ 7 T) scanners in predominantly specialized neuroimaging centers (present estimate of 61 research centers [82]) are also commercially available. The Oxford Centre for Functional Magnetic Resonance Imaging of the Brain (FMRIB) is equipped with a 3 T and a 7 T scanner and, while there are dozens of research groups performing *in-vivo* spectroscopy at 3 T, there are many fewer research groups performing spectroscopy at 7 T.

Increasing the field strength from 3 T to 7 T increases the SNR approximately two-fold [83] and, when combined with an increase in spectral resolution, a number of additional metabolites can be resolved separately (*e.g.* glutamate and glutamine) allowing for more precise and accurate quantification. Why, then, is *in-vivo* spectroscopy at 7 T not more ubiquitous? Though increasing the field strength increases the data quality, it also increases the severity of a number of MR associated challenges.

3.2 Challenges Associated With B_1^+

3.2.1 Energy Deposition and Requirements

The first problem is that the required RF power for a fixed RF pulse length and flip angle increases quadratically with static field strength B_0 [84]. This becomes a problem for human studies at higher magnetic field strengths as the amount of energy absorbed quickly approaches safety limits. The magnetic energy absorbed by nuclear spins ultimately ends up as heat in the sample, but, as this is only a negligible fraction of the total thermal energy present at ambient temperatures, this can be ignored. However, as biological tissue is electrically conductive [85], RF pulses will, according to Faraday's Law, induce electrical currents in tissues. The induced currents deposit most of their energy locally by Joule heating which becomes the dominant safety hazard and, in order to avoid adverse effects, is regulated by the International Electrotechnical Commission [86]. The power deposited by RF pulses is

generally expressed as the specific absorption rate (SAR). European and international regulatory guidelines limit the whole body SAR to 1.5 W/kg averaged over 15 minutes, the head SAR to 3 W/kg averaged over 10 minutes, and the local SAR for any 10 g of tissue to 8 W/kg for the head/torso averaged over 5 minutes [86].

Average SAR in the head or body can be estimated during an experiment by:

$$\mathrm{SAR} = \frac{t_{RF}}{\mathrm{TR}} \times \frac{P}{m} \tag{3.1}$$

where t_{RF} is the time spent applying RF pulses, TR is the repetition time, P is the power of the RF pulse and m is the mass of the head or body. $\frac{t_{RF}}{\mathrm{TR}}$ is the duty cycle which represents the proportion of time spent irradiating the subject during a single TR. As the flip angle for a square pulse θ is linearly proportional to the applied magnetic field strength B_1 and pulse duration T:

$$\theta = \gamma \mathrm{B}_1 T \tag{3.2}$$

and P has been shown to be [87]:

$$P \propto \mathrm{B}_0^2 \mathrm{B}_1^2 \tag{3.3}$$

though this relationship slightly breaks down over 4 T. We can express P in terms of T:

$$P \propto \frac{\mathrm{B}_0^2 \theta^2}{T^2} \tag{3.4}$$

According to Eq. 3.3, stepping from 3 T to 7 T results in an approximate theoretical 5-fold increase of the SAR (for an identical pulse sequence) though in reality this is probably closer to only a 2-fold increase [84]. Nevertheless, this is still a significant concern for pulse sequence design at magnetic field strengths greater than 3 T. Note that though Eqs. 3.1, 3.3, and 3.4 do not provide a complete model for the maximum

local SAR, they provide a qualitative understanding for global SAR behaviour. For example, the SAR can be reduced by increasing the TR, increasing the subject mass, reducing the duty cycle or, for a constant flip angle, increasing the pulse duration.

Most clinical scanners accurately monitor the whole-body or whole-head average SAR, but not all monitor the local SAR (any 10 g of tissue) or local temperature increases [88]. In order to determine the maximum local SAR one must examine local fluctuations in the **E**-field and subject and tissue-specific induced current distributions [89]. While there is currently no practical way of measuring local SAR experimentally with MR, there are a number of methods to calculate the local SAR theoretically. Most methods are based on the finite-difference time-domain EM solver algorithm in which SARs are calculated in a region of tissue-containing "cells" surrounding a central cell and are averaged together as the region is expanded by one cell at a time until 10 g is reached [90]. For a scanner with a single channel transmit coil the local SAR is calculated for a number of different human models and correlated with the global SAR. A safety margin is then included to account for individual variations and the experimental global SAR monitoring alone is used to satisfy SAR safety requirements. The local SAR presents an even greater challenge than global SAR at ultrahigh fields and is especially of concern with parallel transmit applications (discussed in Sec. 3.2.3) as the correlation between local and global SAR breaks down.

3.2.2 B_1^+ Inhomogeneity

Increasing the magnetic field strength beyond 3 T also increases the inhomogeneity of the transmit magnetic field B_1^+. At 7 T, conventional, single transmit, volume coils used for *in-vivo* excitation (birdcage coil [91] or transverse electromagnetic mode (TEM) resonator [92]) provide enhanced sensitivity in the center of the human brain (*e.g.* putamen, substantial nigra and caudate) compared with peripheral regions (*e.g.* frontal, occipital and motor cortices). They usually have electrical currents with equal

magnitudes flowing in opposite directions from opposite sides of the head which can create a standing wave. The standing wave results in constructive interference near the center of the head and destructive interference $\frac{1}{4}$ wavelength away. For magnetic fields at 3 T or below, the wavelength is long enough that this can usually be ignored. However, at 7 T for example, the wavelength is approximately 13 cm and therefore areas of constructive and destructive interference can occur in the brain. While it could be expected that tissue conductivity would lead to decreased signal at the center of the brain (as is the case for lower field strengths) thereby damping the standing wave, constructive interference from fields propagating all around the head still result in an overall central signal increase [93].

$\mathbf{B_1}$ can be separated into two circularly polarized components on an axial plane through the center of a sample as:

$$\begin{aligned} \hat{\mathbf{B}}_1^+ &= (\hat{\mathbf{B}}_x + i\hat{\mathbf{B}}_y)/2 \\ \hat{\mathbf{B}}_1^- &= (\hat{\mathbf{B}}_x - i\hat{\mathbf{B}}_y)^*/2 \end{aligned} \tag{3.5}$$

where $\hat{\mathbf{B}}_x$, $\hat{\mathbf{B}}_y$, $\hat{\mathbf{B}}_1^+$, and $\hat{\mathbf{B}}_1^-$ are complex vectors as denoted with a circumflex and $*$ is the complex conjugate [94]. We assume that $\hat{\mathbf{B}}_1^+$ is in the direction of the nuclear precession and therefore the component that determines the excitation. We can now rewrite the RF flip angle generated by a rectangular, constant RF pulse of duration τ as (Eq. 2.1):

$$\theta = V \left| \hat{\mathbf{B}}_1^+ \right| \gamma\tau \tag{3.6}$$

where V is a dimensionless scaling factor proportional to the coil driving voltage [95]. The signal intensity of a particular metabolite SI is proportional to the sine of the flip angle [96], the receptivity of the receiving coil $\hat{\mathbf{B}}_1^{-*}$ and the concentration of the

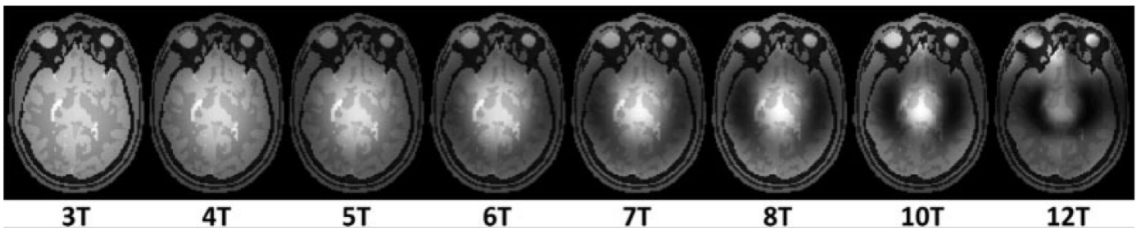


Figure 3.1: Simulated axial images as a function of field strength. Note the central brightening and decreased signal around the periphery as field strength increases. Adapted from [93] with permission.

metabolite in the excited region ρ:

$$SI \propto \rho \left|\hat{\mathbf{B}}_1^{-*}\right| \sin(V \left|\hat{\mathbf{B}}_1^{+}\right| \gamma\tau) \tag{3.7}$$

Here we see that the signal intensity depends linearly on the reception but sinusoidally on the excitation. It is this discrepancy that, at higher fields, leads to periodic signal intensity over an axial slice. Fig. 3.1 shows simulated images as a function of field strength.

As outlined in Eq. 1.34, the chemical shift for a given resonance frequency is linearly dependent on B_0. Therefore, for a given spectrum, increasing B_0 results in an increased range of resonant frequencies and one must be careful that the pulse bandwidth is wide enough to accommodate the increased spectral dispersion. The combination of increased SAR, B_1^+ amplitude requirements, B_1^+ inhomogeneity and pulse bandwidth constraints culminate in the need for specialized RF pulses that are B_1^+ insensitive, do not require unattainable RF power, do not produce prohibitively high SAR and excite a relatively large bandwidth. As outlined in Sec. 3.2.3, increasing the pulse duration can reduce the B_1^+ demand and reduce SAR though doing so results in a smaller bandwidth which also introduces a large chemical shift displacement error (CSDE). The CSDE can be defined as the localization difference between two resonances with different chemical shifts caused by limitations in the excitation

or refocusing pulse bandwidth. The fraction of discrepancy in localization (CSDE) between two peaks of frequency f_1 and f_2 (in ppm) is given by:

$$\text{CSDE} = \frac{\gamma(f_1 - f_2)\text{B}_0}{\text{BW} \cdot 10^6} \tag{3.8}$$

where BW is the bandwidth of the pulse (given in Hertz). Consider a Mao optimized 180° refocusing pulse [97] with a duration of 6 ms and corresponding bandwidth of 1.0 kHz. This pulse is routinely used at 3 T but conventional RF amplifiers cannot generate the required amplitude at 7 T and would require a much longer duration. Even if such a pulse could be generated for 7 T, the CSDE over the spectral range of interest (from water at 4.7 ppm to lipid CH_3 at 0.9 ppm) would increase from 49% at 3 T to over 113% at 7 T. In order to achieve the approximately the same CSDE at 7 T, one would need to increase the bandwidth of the pulse to 2.35 kHz, reduce the duration to 2.3 ms and increase the required RF power well beyond present RF amplifier and SAR limits.

3.2.3 Solutions to B_1^+ Inhomogeneity

One of the most effective responses to increased B_1^+ inhomogeneity and SAR challenges associated with MRS at field strengths $\geq$ 7 T is multiple transmit array coils (also known as parallel transmit or B_1 shimming) [98]. In particular, parallel transmit refers to a multiple transmit array coil capable of independent adjustment of the phase and amplitude of the individual coil elements, thereby allowing uniform flip angles over a targeted region. B_1 shimming extends this and allows for independent control of the waveforms used in the individual coil elements. As mentioned in Sec. 2.1, MR signal from one VOI can be detected by multiple receive coils in order to dramatically increase signal detection efficiency [99]. It has been shown that by sampling each coil on a different digital receiver one can remove signal loss caused by

phase differences between coil elements [100]. Analogously, one can acquire individual transmit profiles for each transmission coil, sum the individual coil B_1^+ fields and minimize any destructive phase cancellation [101]. While the detected signal will still be nonuniform due to sensitivity differences in the receive coils, this can be avoided by combining individual coil signals after acquisition [102]. The net result is that not only can the B_1^+ field be made very homogeneous, but the RF power required to achieve a given magnitude of B_1^+ in a local area can be significantly reduced. One difficult challenge associated with parallel transmit is that determining the SAR is far more complicated when compared with a single transmission coil as now each coil channel must be individually monitored and global and local SAR are no longer correlated (see Sec. 3.2.1) [101]. Therefore for each subject, experimental setup, B_1^+ shim solution, and set of pulse sequence parameters a full computer simulation must be performed. Additionally, monitoring of the forward and reflected RF power on each channel must be performed during the experiment and if the power input into any coil element exceeds a predefined safety threshold the experiment must be immediately stopped [86].

Implementation of a multi-element transmit array in a routine clinical environment is very difficult and only a small number of research groups currently have access to a human-safe setup. Alternatively, a simpler approach can be used by placing high dielectric materials around the head in order to increase B_1^+ homogeneity [103] or efficiency [104, 105]. Dielectric pads have the advantage of not requiring software or hardware modification, are simple to fabricate and recent studies have shown that dielectric pads do not produce higher local energy deposition and do not have any detrimental effects on the B_0 homogeneity or receive array coupling [106]. In the region near to the pads, B_1^+ has been shown to increase by over 100% and B_1^- by up to 50% [106]. According to Maxwell's equations, in conductive dielectric materials (such as the human brain tissues), the magnetic field is perturbed by the conductive

current $\mathbf{J}_C$ and displacement current $\mathbf{J}_D$:

$$\nabla \times \mathbf{B} = \mu \mathbf{J}_C + \mu \mathbf{J}_D = \mu\sigma\mathbf{E} + i\mu\epsilon_0\epsilon_r\omega\mathbf{E} \tag{3.9}$$

where $\mathbf{B}$ is the magnetic flux density, $\mathbf{E}$ is the electric field, ϵ_0 is the electric constant, ϵ_r is the relative permittivity of the dielectric, μ is the magnetic permeability, σ is the electrical conductivity and ω is the frequency of the RF field. In a homogeneous medium, the conductive current leads to decay of the RF field, whereas the displacement current increases RF propagation [107]. If we take the ratio of these two currents we get:

$$\mathbf{J}_C/\mathbf{J}_D = \sigma/\epsilon_0\epsilon_r\omega \tag{3.10}$$

For human tissues this ratio is ~ 0.5 so both currents play an important role but for a high-permittivity material (like a dielectric pad) the ratio can drop to ~ 0.005 and therefore the conductive current can be effectively ignored. Hence materials with low σ and high ϵ_r can result in an enhanced B_1 in the local area around the material. A demonstration of the effect of a dielectric material on MRS data is shown in Fig. 3.2.

3.3 Challenges Associated With B_0

3.3.1 B_0 Inhomogeneity

The final problem that arises at 7 T is increased B_0 inhomogeneity [108]. As mentioned in Sec. 2.8, inhomogeneity across acquisition voxels will broaden spectral linewidths. A current passing through a conductor creates a magnetizing field $\mathbf{H}$ that induces a magnetic field $\mathbf{B}$ and are related in a linear substance by:

$$\mathbf{B} = \mu\mathbf{H} \tag{3.11}$$

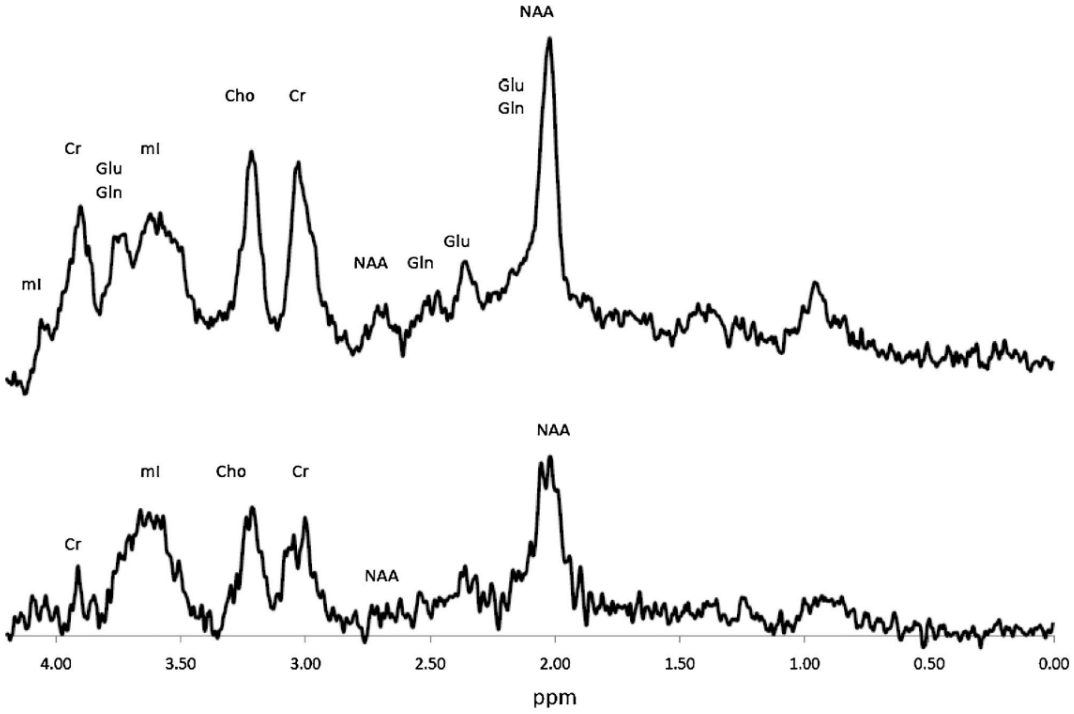


Figure 3.2: ^{1}H spectra acquired from the temporal lobe of the same subject with a calcium titanate dielectric material present (top) and without the pads (bottom). Adapted from [105] with permission.

where μ is the magnetic permeability of the medium with μ_0 describing the magnetic permeability in a vacuum. The interaction between moving charged particles in a medium and a magnetic field will induce a magnetization $\mathbf{M}$ in the medium which combines with $\mathbf{H}$:

$$\mathbf{B} = \mu\mathbf{H} = \mu_0\mathbf{H} + \mu_\mathbf{0}\mathbf{M} \tag{3.12}$$

As μ is generally very close to μ_0, it is convenient to use use the magnetic susceptibility $\chi = (\mu/\mu_0) - 1$ to simplify Eq. 3.12:

$$\mathbf{B} = \mu_0(1 + \chi)\mathbf{H} \tag{3.13}$$

At a tissue interface with tissue susceptibilities χ_1 and χ_2, a local field inhomogeneity $\Delta\mathrm{B}_0$ is generated:

$$\Delta\mathrm{B}_0 = (\chi_1 - \chi_2)\mathrm{B}_0 \tag{3.14}$$

Therefore, the local inhomogeneity is linearly proportional to the static magnetic field strength and to the difference in magnetic susceptibilities. At higher field strengths this places extra demands on shimming equipment in order to maintain an adequate linewidth.

3.3.2 Solutions to B_0 Inhomogeneity

B_0 shimming is a key factor for successful MRS at 7 T as it determines the achievable spectral resolution and reliability of metabolite quantification. At lower field strengths, large regions of the brain can be sufficiently shimmed using first and second-order shims [109]. It has also been demonstrated that at 7 T a first and second-order shim system is sufficient for reasonably small volumes as seen in conventional single voxel spectroscopy (SVS) [110]. However, to achieve acceptable linewidths over a larger region at 7 T third-order B_0 shimming is required [111, 112]. Regrettably, most

human 7 T scanners are not equipped with third-order shim coils. A larger shim volume is required when employing magnetic resonance spectroscopic imaging (MRSI) [111, 113, 114]. MRSI acquires metabolic profiles over large regions of the brain at the same time by using phase encoding gradients (see Sec. 2.3). Alternatively, one can adapt single voxel localization sequences such as STEAM [115] or semi-LASER [29, 116] to multiple regions by dynamic shim updating (DSU) for each region and acquiring spectra in an interleaved fashion. This approach maintains the precision and relative simplicity of single voxel techniques as well as only requiring second-order shims but enables several regions to be studied concurrently.

Ernst and Hennig first demonstrated this effective technique for two voxels at 2 T using PRESS [117]. They dynamically shimmed the first order gradients and tilted the volume selection gradients in order to avoid mutual saturation of the two voxels and greatly increase scan efficiency. Théberge *et al.* used STEAM at 4 T to acquire signal from 2 voxels in a single TR (2.6 s) by employing DSU of the first order shims and decreased the experimental time by approximately 50% [118]. Koch et al. recently used semi-LASER at 4 T to acquire signal from 4 voxels in a single TR (2.5 s) by employing DSU for both the first and second order shims [119]. They implemented a specialized B_0 compensation and shim pre-emphasis [120] system to correct for temporal effects associated with eddy currents generated by changing second order shim currents [121]. Their results showed a significant improvement in spectral linewidth compared with a static global shim resulting in high quality spectra in all 4 voxels.

Chapter 4

Two-Voxel Spectroscopy With Dynamic B_0 Shimming and Flip Angle Adjustment at 7 T in the Human Cortex

4.1 Introduction

In this chapter a practical acquisition strategy is presented that can acquire high quality spectra at 7 T from multiple VOIs using standard vendor hardware by combining dynamic shim updating (DSU) of first order shims (in a manner as first outlined by Ernst and Hennig [117]) generated by regular gradient systems with dielectric pads. As dielectric pads may not produce a uniform B_1^+ between the VOIs, flip angles may need to be adjusted for each VOI in order to maintain high quality spectra for each voxel. To test the feasibility of this technique at 7 T, spectra were acquired from voxels centered on the hand knob of the motor cortices (M1) bilaterally [122]. In order to compare the effectiveness of this acquisition strategy, isolated static single voxel

experiments were also performed from each M1 separately. This practical acquisition technique lends itself to functional spectroscopy applications requiring high spectral and temporal resolution in multiple brain regions.

4.2 Experimental

Subjects

Six healthy volunteers [5 male; aged 25 ± 3 years; 2 left handed] participated in this study after giving informed consent under an institutionally agreed technical development protocol.

Dielectric Pad

To optimize B_1^+ efficiency in the VOI, we used dielectric pads containing barium titanate ($BaTiO_3$) prepared by heat-sealing within polypropylene. $BaTiO_3$ powder (99%, Sigma Aldrich, UK) was suspended in deuterium oxide (99%, Sigma Aldrich, UK) until the powder became saturated with a mass-to-mass ratio of 4:1. In order to determine what pad geometry provided the optimum B_1^+ efficiency we performed an initial pilot experiment with 4 different pad dimensions: a) 11 × 11 cm^2, b) 30 × 4 cm^2, c) 24 × 5 cm^2, and d) 12 × 5 cm^2 (Fig. 4.1). The pads were placed 1 or 2 at a time on top or across the subject's head for the duration of the experiment. For each pad orientation and size, B_1 maps were acquired using the actual flip angle imaging (AFI) sequence [123] (field of view, 240 × 240 mm^2 ; TR1/2 = 6/30 ms; TE = 2.58 ms; slice thickness 2.5 mm; non-selective flip angle 60°, scan time 3 minutes) and are shown in Fig. 4.2. The decision on which pad to use ultimately came down to practicality. As shown in Fig. 4.2, two 11 × 11 cm^2 pads provided the largest increase in B_1^+ in the VOIs. Unfortunately, initial placement of the pads was not only very difficult and time consuming but only very small heads could still fit inside the coil.

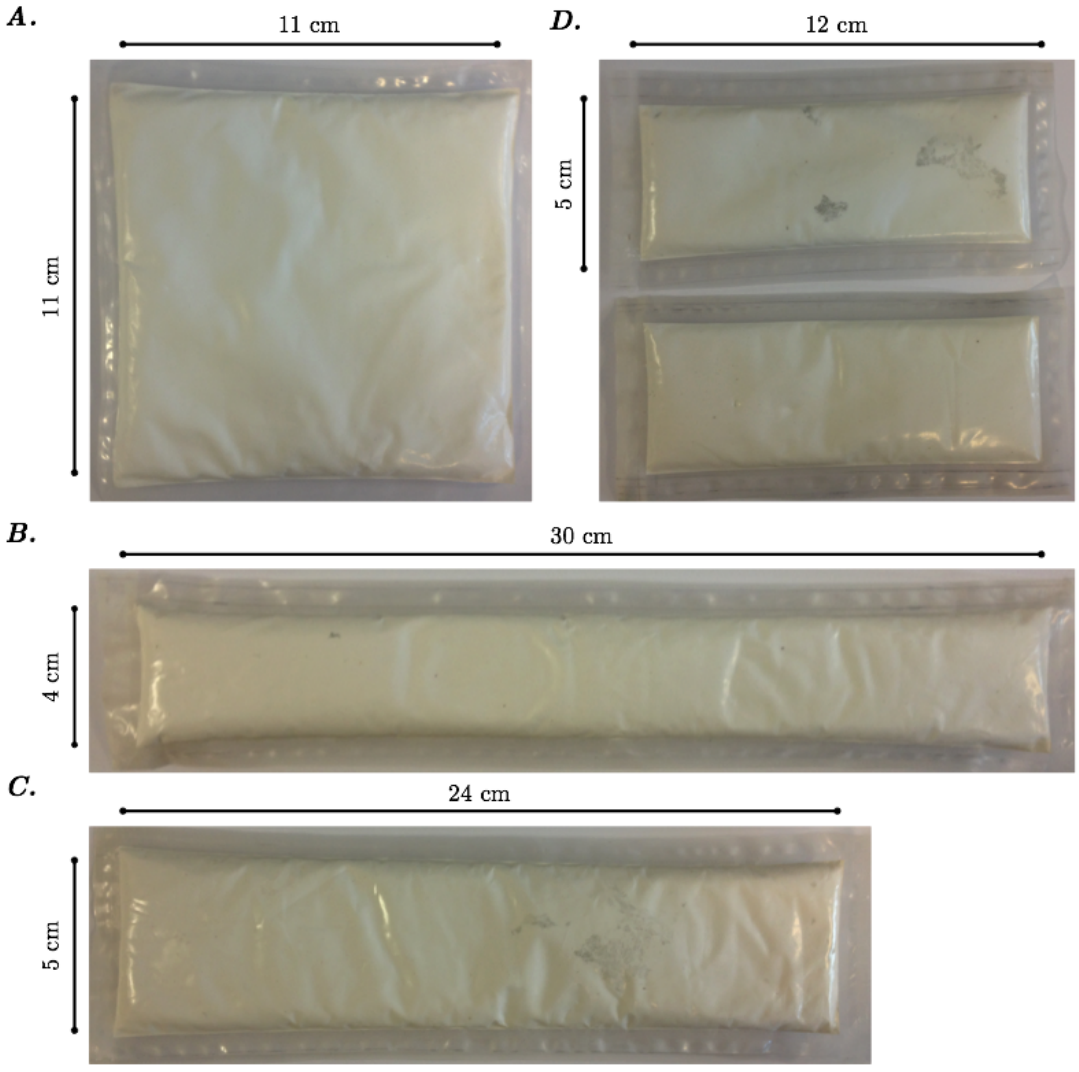


Figure 4.1: Barium titanate dielectric pads of thickness 5 mm: A) 11 × 11 cm^2, B) 30 × 4 cm^2, C) 24 × 5 cm^2, and D) two 12 × 5 cm^2.

We determined that a single 11 × 11 cm^2 pad provided the largest signal increase with the least signal variability between the VOIs and therefore this arrangement was used for the full study. In terms of RF safety this pad geometry and orientation has been used previously and was shown to produce no increase in peak local SAR [124].

MR Protocol

All measurements were performed on a 7 T Siemens MAGNETOM scanner (Siemens, Erlangen) equipped with a 60 cm (inner diameter) gradient coil (maximum amplitude 70 mT/m; maximum slew rate 200 mT/m/ms) and a Nova Medical 1 channel transmit, 32-channel receive array head-coil (Nova Medical, Wilmington, USA). The second-order shim coils in the gradient system had a maximum strength of 7.04 mT/m^2 at 20 A for ZX, ZY, XY, X^2+Y^2 and 11.0 mT/m^2 at 20 A for Z^2. In order to verify that adequate and normalized transmit power had been achieved in the regions of interest with the dielectric pads, B_1 maps were acquired using the actual flip angle imaging (AFI) sequence [123] (field of view, 240 × 240 mm^2; TR1/2 = 6/30 ms; TE = 2.58 ms; slice thickness 2.5 mm; non-selective flip angle 60°, scan time 3 minutes). To aid in selecting the regions of interest, structural 3D T_1-weighted images were acquired with an MP-RAGE sequence [125] (field of view, 192 × 192 mm^2; TR = 2.2 s; TE = 2.82 ms; slice thickness 1 mm; slices 96; non-selective inversion; scan time 3 minutes) for all subjects.

Shimming

In order to compare the effectiveness of DSU at UHF, spectra were acquired from two voxels under two conditions: (i) DSU, and (ii) static single voxel spectroscopy. For the DSU acquisitions, B_0 shimming was performed in a two-step process. First, GRE-SHIM [63] (field of view, 384 × 384 mm^2; TR = 600 ms; TE1/2 = 2.04/4.08

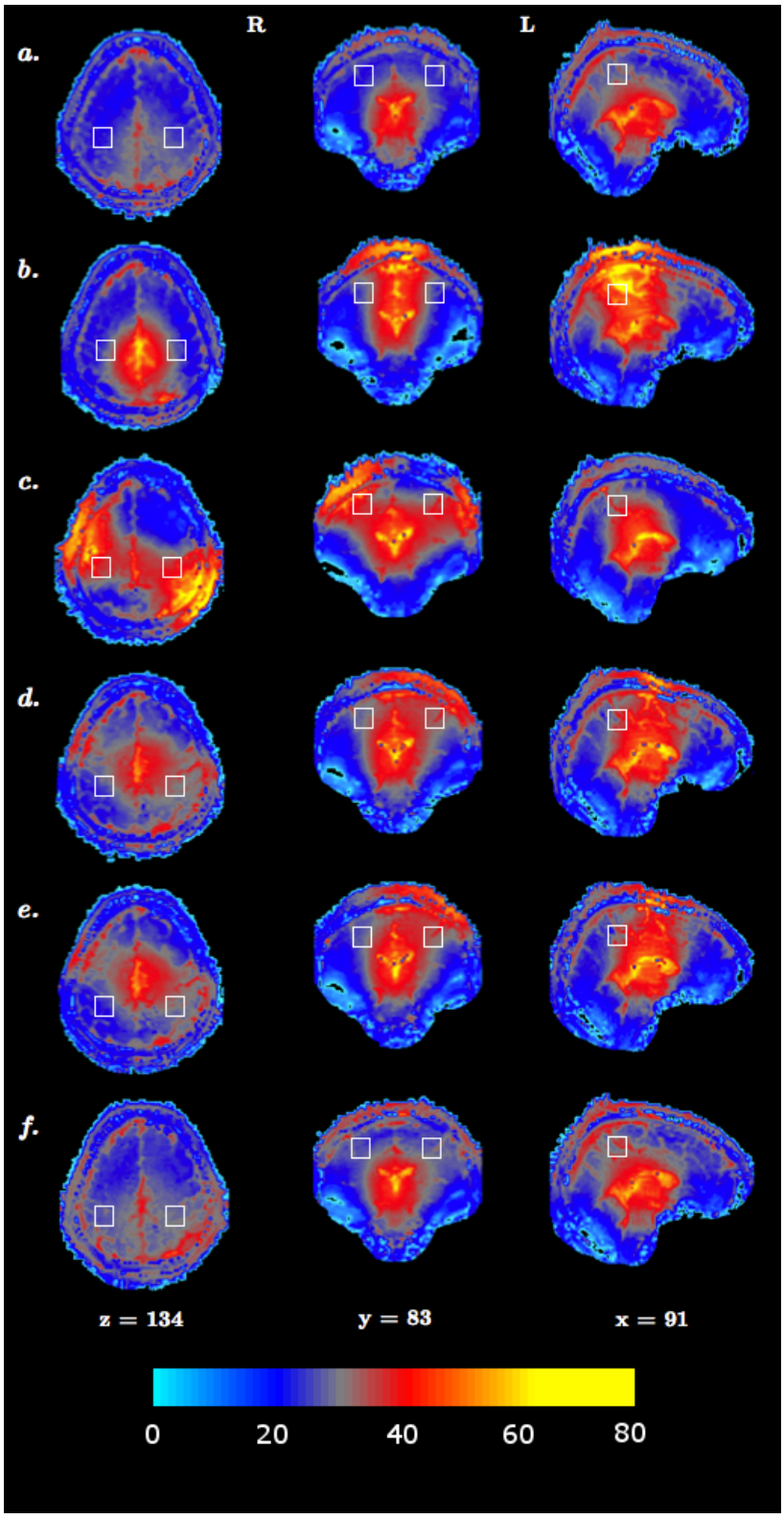


Figure 4.2: B_1^+ maps with a) no pad, b) a 11 × 11 cm pad centered on top of the head, c) two 11 × 11 cm pads, one on each side of the head, d) a 30 × 4 cm pad centered across the top of the head, e) a 24 × 5 cm pad centered across the top of the head, f) two 12 × 5 cm pads placed over each motor cortex region. Intensity refers to flip angle in that voxel.

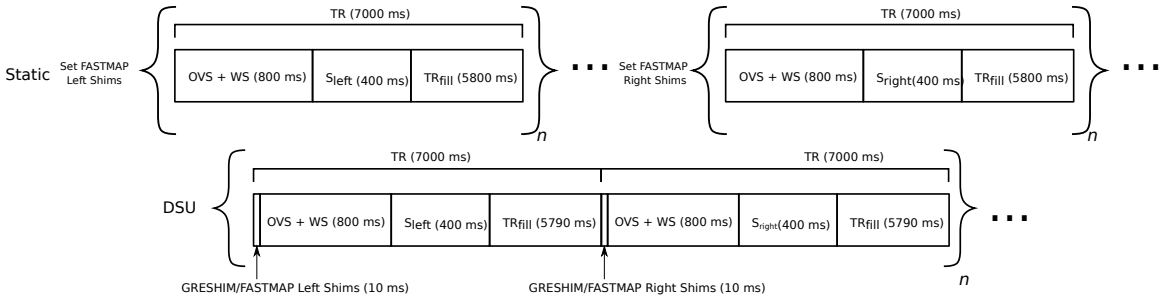


Figure 4.3: a) Acquisition scheme for ^{1}H spectroscopy. Upper: Static single-voxel sequence. Lower: Interleaved DSU scheme. S_{left} and S_{right} – signal localization and acquisition for left and right VOIs, n – number of acquisition averages.

ms; slice thickness 4 mm; flip angle 15°; slices 64; scan time 45 s) was used to determine the optimal second order shim currents (Z^2, ZX, ZY, XY, X^2+Y^2). The second order shim currents were optimized for the total volume encompassing the two voxels ($80 \times 20 \times 20$ mm^3). The second step involved determining optimized first order shims (X, Y, Z) for each voxel using FASTMAP [64] – while keeping the second order shims static. Prior to acquisition, excitation, water suppression and outer volume suppression (OVS) flip angles were calculated for each voxel. Specific parameters and shim values for both voxels were then entered into the system prior to the start of acquisition. The sequence was programed to alternate all the relevant parameters between each transient, with a short delay (10 ms) included for synchronization of the sequence and shim updates. Effectively, our implementation of DSU altered the magnetic field gradients with a voxel specific offset. For the static single voxel acquisitions, B_0 shimming for all shim coils was performed using FASTMAP optimized for each individual voxel. This was performed over four sequential FASTMAP acquisitions – two to determine the second-order shims and two to determine the first-order shims. Fig. 4.3 illustrates the difference between DSU and static acquisitions.

MR Spectroscopy

All spectra were localized using semi-LASER as described by Öz and Tkác [29] as this method has been shown to be robust against B_1-inhomogenieties and has a low chemical shift displacement error (CSDE) at ultra high field [126]. The duration of the asymmetric slice-selective excitation pulse was 4.2 ms with bandwidth 3.70 kHz and the duration of the adiabatic slice selective refocusing pulses was 4.5 ms with bandwidth 5.27 kHz [127]. Crushing gradients were applied before and after the refocusing pulses as well as between each acquisition to suppress unwanted coherences. All spectra were acquired with VAPOR [27] water suppression (pulse duration = 35 ms) and 8 outer volume suppression pulses (pulse duration = 4.6 ms) as performed previously [127]. 64 averages with an echo time of 30 ms and repetition time of 7 s were acquired for both DSU and static acquisition schemes. As SAR is the limiting factor for semi-LASER at 7 T, this technique does not gain any scan time over static measurements as was achieved previously at lower field strengths. As a result, scan times of 15 minutes were required for both acquisition schemes. Signal was acquired from two voxels located in the left and right motor cortex with a voxel size of 20 × 20 × 20 mm^3 and average distance of 40 mm apart.

Data Processing and Metabolite Quantification

The unsuppressed water signal acquired from the same VOI was used to remove residual eddy current effects and to reconstruct the phased array spectra. This included weighting the spectra based on the sensitivity of each receive element at the VOI and correcting for the different channel-specific phase shift offset terms of the complex spectra prior to summation. Single scan spectra summed from 32 channels were corrected for frequency and phase variations induced by subject motion and then signal averaged. Finally any residual water signal was removed by using a Hankel-Lanczos singular value decomposition (HLSVD) [66] filter before LCModel [69] analysis. The

raw data was extracted off the scanner using each second average was reconstructed separately.

Metabolites were quantified using LCModel. The model spectra of alanine (Ala), aspartate (Asp), ascorbate/vitamin C (Asc), glycerophosphocholine (GPC), phosphocholine (PCho), creatine (Cr), phosphocreatine (PCr), γ-aminobutyric acid (GABA), glucose (Glc), glutamine (Gln), glutamate (Glu), glutathione (GSH), *myo*-inositol (*myo*-Ins), lactate (Lac), *N*-acetylaspartate (NAA), *N*-acetylaspartylglutamate (NAAG), phosphoethanolamine (PE), *scyllo*-inositol (*scyllo*-Ins) and taurine (Tau) were generated based on previously reported chemical shifts and coupling constants [128, 129] by VeSPA Project (Versatile Simulation, Pulses and Analysis) [70]. *In-vivo* acquired macromolecule spectra from the occipital cortex were included in the model. LCModel analysis was performed on all spectra within the chemical shift range 0.5 to 4.2 ppm. Metabolite concentrations were obtained relative to an unsuppressed water spectrum acquired from the same VOI assuming a water content of 71% [130]. Only metabolites quantified with Cramér–Rao lower bound (CRLB) $\leq 30\%$ in at least four of six subjects were included in the final neurochemical profile. In the case of a high correlation between two metabolites ($r <$ -0.5) being measured, the sum was used instead *e.g.* total creatine (tCr), total choline (tCho), Glu+Gln and Glc+Tau. FMRIB's Automated Segmentation Tool (FAST) [131] was used to correct the structural images for B_1 inhomogeneity and calculate the relative quantities of grey matter, white matter and cerebrospinal fluid (CSF) within the voxels before correcting metabolite concentrations by the fraction of the voxel containing CSF. Finally corrections were made for grey matter (GM) / white matter (WM) differences between subjects by employing the method outlined by Dou *et al.* [132]. This was performed by performing a linear regression between uncorrected metabolite concentrations and corresponding GM percentages across both VOIs and subjects. The corrected metabolite concentrations were then taken as the values that fall on the fit at their corresponding GM

percentage.

Paired two-tailed t-tests were performed to examine differences in linewidths between VOIs and acquisition techniques. To assess the agreement between dynamic and static acquisition schemes, a Bland-Altman analysis [133] was performed on each reported metabolite. For all subjects, in each VOI, for each metabolite, the difference (in μmol/g) between acquisition techniques is calculated. If a normal distribution is assumed, 95% of the differences will fall between $\pm$ 1.96 standard deviations of the mean difference (referred to as the confidence interval). As CRLBs express a theoretical lower limit on the standard deviation of a metabolite, we compared the static CRLBs with the standard deviation of the Bland-Altman differences between acquisition techniques in order to assess if the DSU scheme can be used interchangeably with static acquisitions.

4.3 Results

B_1 Optimization

In order to confirm the efficacy of the dielectric pad at increasing local B_1^+ sensitivity in the VOIs, B_1 maps were acquired with and without the pad present in a single subject (Fig. 4.4). The B_1^+ maps established that the dielectric pad increased the B_1^+ in the VOIs for all subjects. The relative transmit efficiency (RTE) or ratio of the B_1^+ maps with and without dielectric pads averaged over each voxel was 1.2 $\pm$ 0.1 for the left VOI and 1.3 $\pm$ 0.1 for the right VOI. This resulted in transmit reference voltages in the left and right motor cortices of 213 $\pm$ 42 V and 216 $\pm$ 23 V, respectively. As per Siemens documentation, the transmit reference voltage corresponds to the voltage required to produce a 1 ms 180° pulse (11.75 µT) for ^{1}H.

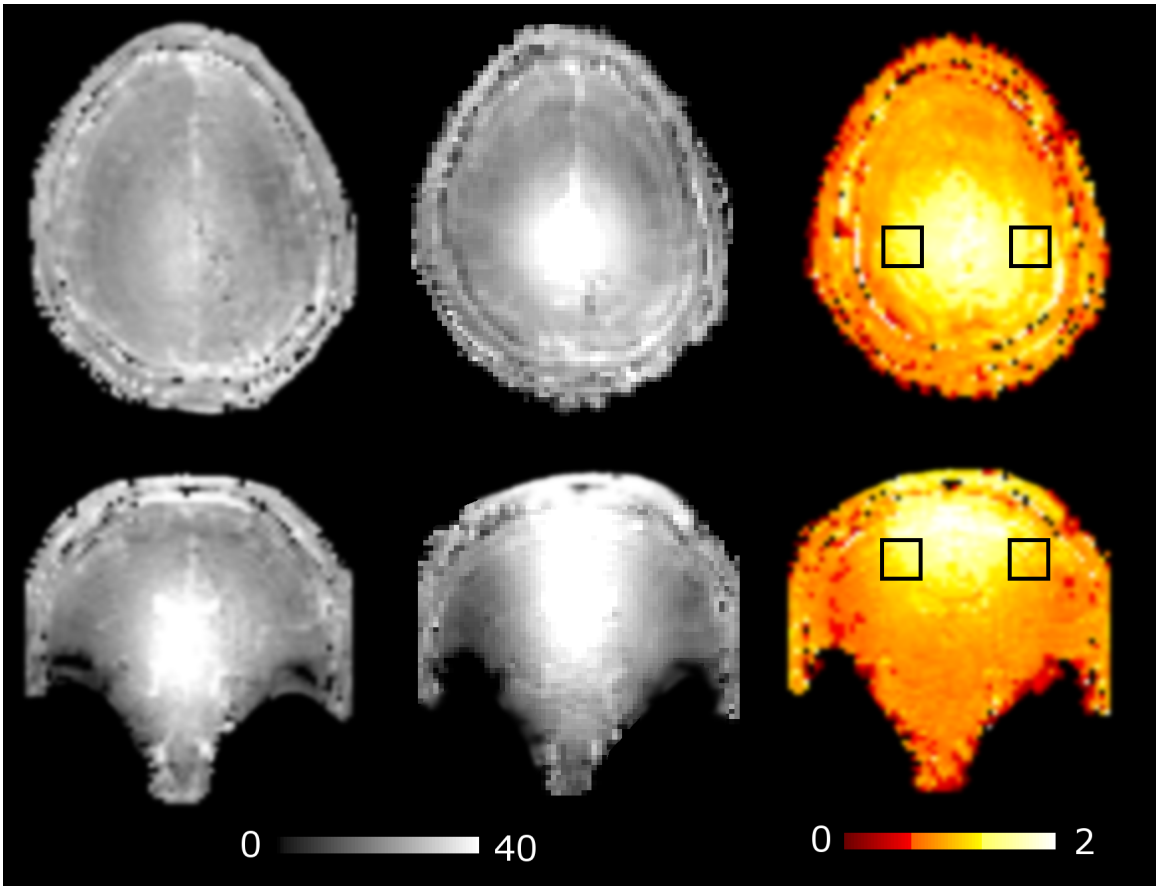


Figure 4.4: Acquired B_1^+ field maps without (left) and with (center) the barium titanate dielectric pad placed on subject's head. Intensity refers to flip angle in that voxel. Ratio of images (right) shows a B_1^+ increase in both VOIs.

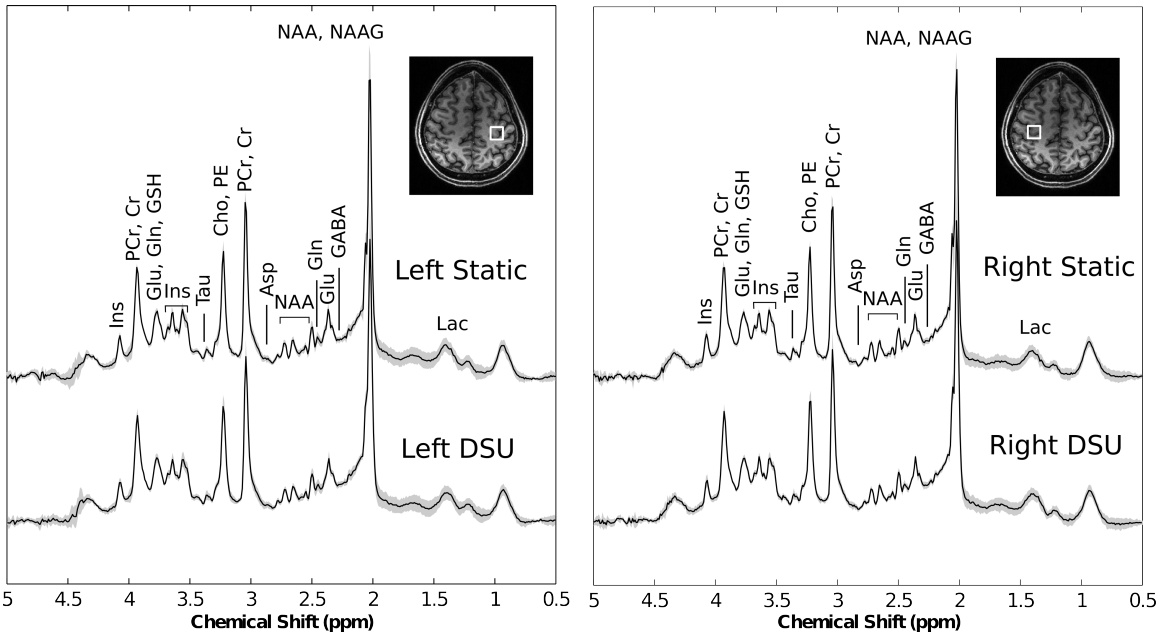


Figure 4.5: Average *in-vivo* ^{1}H semi-LASER spectra (TR = 7 s; TE = 30 ms; Averages = 64) from all six subjects from the two VOIs using both acquisition schemes at 7 T. The shaded grey area is the standard deviation. Note the high spectral quality and reproducibility in all conditions.

Spectral Quality

Fig. 4.5 shows the average spectra from both methods in all six subjects, it shows that spectra with high SNR and spectral resolution were obtained from the two VOIs with both DSU and static measurements. Water suppression was effective and virtually identical for both techniques leading to a residual water signal smaller than the NAA singlet peak for both regions. In addition, the double localization accomplished by semi-LASER and OVS eliminated signals from outside the voxels resulting in artifact-free spectra with a flat baseline. Table 4.1 shows the linewidths and SNR achieved with the two methods. It shows a marginal increase in linewidths (0.8 Hz) and drop in SNR for the DSU method compared to a static shim. These differences were not significant (paired t-test, 2-tailed, p-value > 0.1). The measured linewidths were similar to those reported previously [124].

	Left (DSU)	Left (Static)	Right (DSU)	Right (Static)
Water LW (Hz)	12.8 ± 1.3	12.0 ± 0.8	12.4 ± 1.1	11.6 ± 0.7
tCr LW (Hz)	10.2 ± 0.8	9.3 ± 0.6	9.9 ± 1.4	9.0 ± 0.5
SNR_{NAA}	140.2 ± 19.4	147.2 ± 28.3	143.1 ± 21.8	138.5 ± 9.9
GM ± SD	0.29 ± 0.05		0.31 ± 0.05	
WM ± SD	0.64 ± 0.07		0.62 ± 0.06	
CSF ± SD	0.07 ± 0.02		0.07 ± 0.01	

Table 4.1: Water signal linewidths, methyl resonance tCr linewidths, SNR_{NAA}, and tissue content for both VOIs using both acquisition methods. Values reported are mean ± standard deviation of all spectra and linewidths refer to FWHM. SNR_{NAA} is calculated using the maximum height of the signal of NAA methyl resonance. Note that no significant difference (p-value ≥ 0.5) between both VOIs and acquisition methods was determined for linewidths, SNR or tissue content.

Neurochemical Profiles

The high spectral quality enabled the quantification of a neurochemical profile consisting of 13 individual and 3 combined metabolites. The mean concentrations of metabolites that met our criteria for reliable quantification are shown in Fig. 4.6. Both the sum and individual values are reported for NAA and NAAG because these metabolites could be reliably distinguished in both regions with correlation coefficients between -0.43 and -0.48 (Fig. 4.7). Fig. 4.8 illustrates the average Bland-Altman agreement (average difference in µmol/g between acquisition techniques) and 95% confidence intervals between dynamic and static acquisition methods. Table 4.2 summarizes differences in variation between acquisition schemes. All metabolites (except Lac) resulted in variations similar to the static CRLBs suggesting a good agreement.

4.4 Discussion

This study demonstrates that high-quality semi-LASER spectra can be obtained from two VOIs in an interleaved mode within a single session at 7 T using a single channel transmit, 32 channel receive coil, and dielectric pads. We have shown that, by

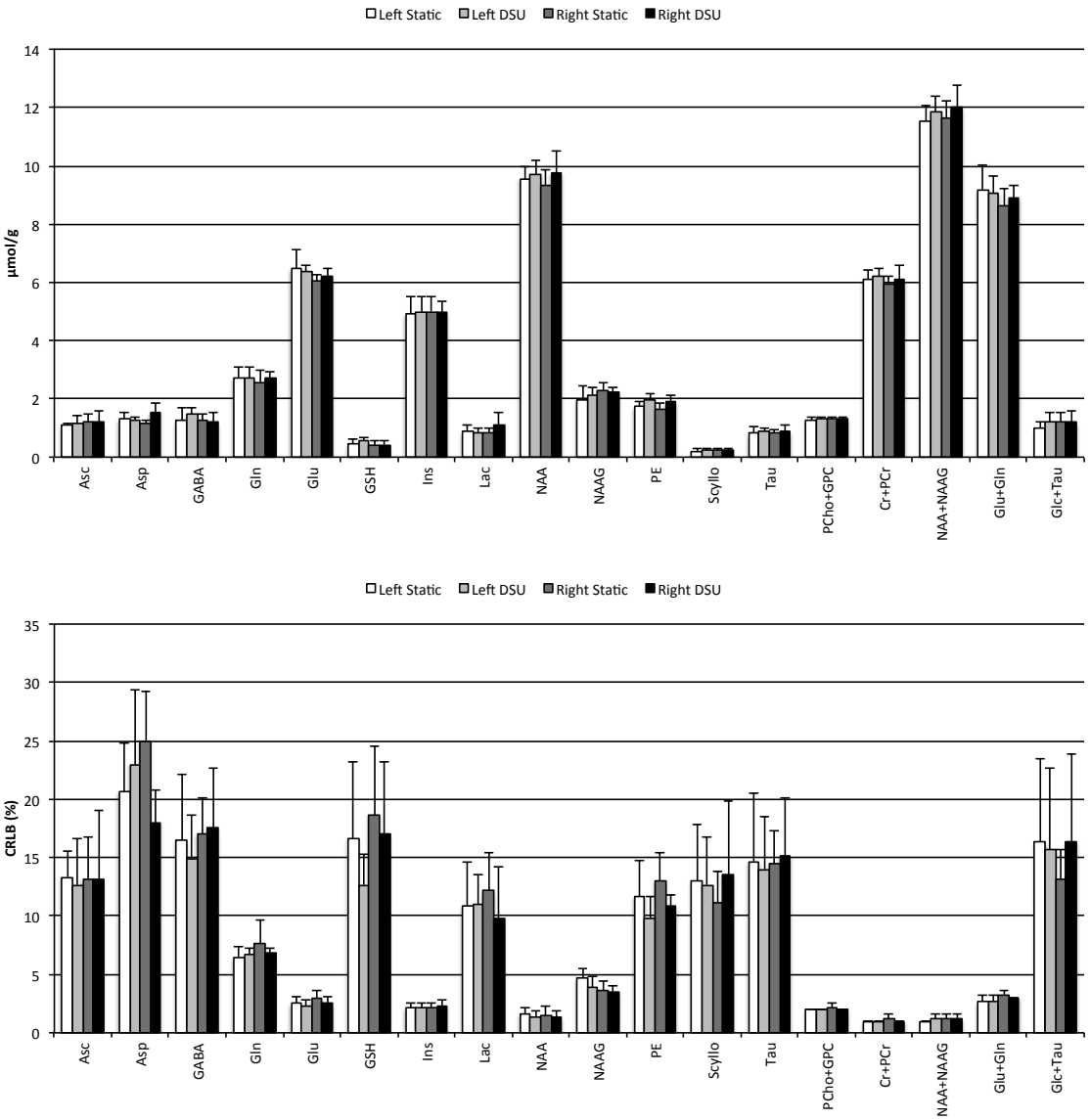


Figure 4.6: Neurochemical profiles (above) and corresponding CRLBs (below) from both VOIs and acquisition schemes determined by LCModel fitting of semi-LASER spectra acquired at 7 T. Note that no significant difference (p-value ≥ 0.5) between conditions was determined for any metabolite concentrations. Error bars are inter-subject standard deviation.

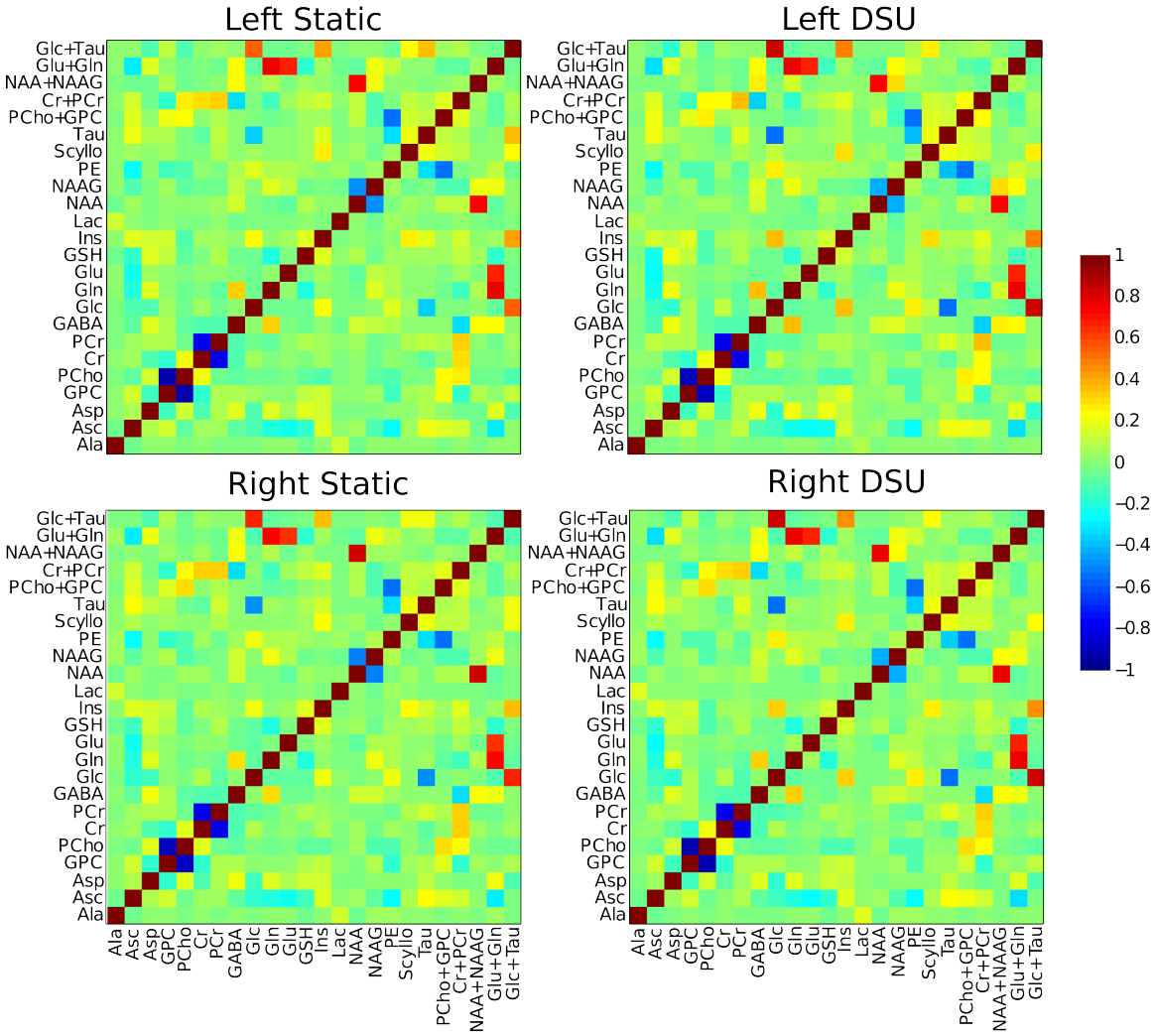


Figure 4.7: Mean correlation coefficient matrices between metabolite concentrations for both VOIs and techniques determined by LCModel. Nonzero off-diagonal elements of the correlation coefficient matrices indicate the level of covariance between the fitting results for the corresponding two metabolites.

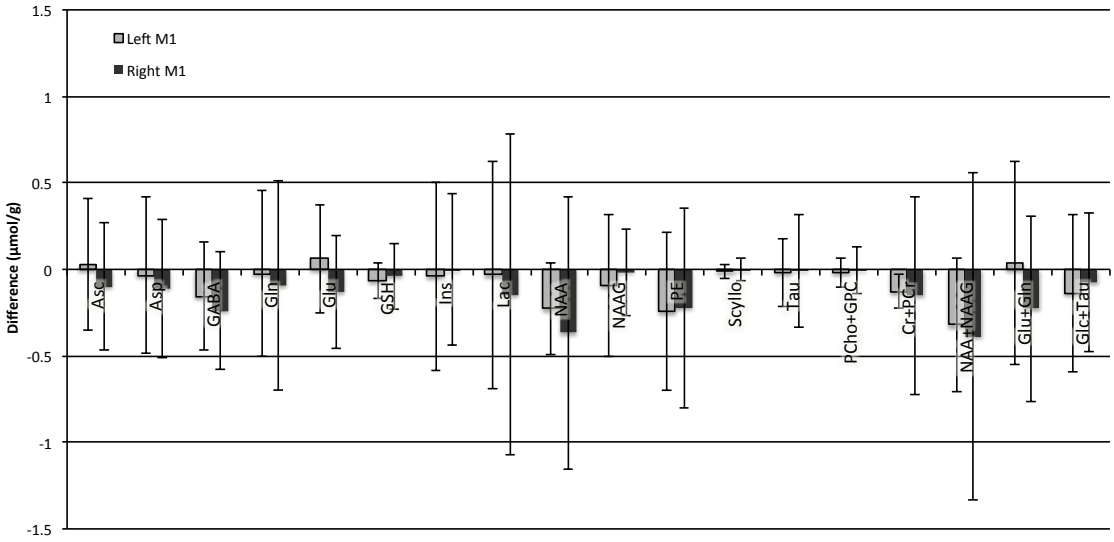


Figure 4.8: The average and 95% confidence interval of agreement between static and DSU acquisition schemes (µmol/g) measured using the Bland-Altman method for both left and right VOIs.

	Left		Right	
	B-A Variation	Static CRLBs	B-A Variation	Static CRLBs
Asc	18.1%	13.3%	14.9%	13.2%
Asp	17.5%	20.7%	22.3%	25.0%
GABA	9.8%	16.5%	10.6%	17.0%
Gln	8.9%	6.5%	11.8%	7.7%
Glu	2.5%	2.5%	2.7%	3.0%
GSH	11.0%	16.7%	22.4%	18.7%
Myo-Ins	5.6%	2.2%	4.4%	2.2%
Lac	37.8%	10.8%	50.8%	12.2%
NAA	1.4%	1.7%	4.2%	1.5%
NAAG	10.4%	4.7%	5.6%	3.7%
PE	12.7%	11.7%	16.6%	13.0%
Scyllo	9.0%	13.0%	13.6%	11.2%
Tau	12.2%	14.7%	19.0%	14.5%
PCho+GPC	3.4%	2.0%	5.3%	2.2%
Cr+PCr	0.8%	1.0%	4.9%	1.2%
NAA+NAAG	1.7%	1.0%	4.1%	1.2%
Glu+Gln	3.3%	2.7%	3.1%	3.2%
Glc+Tau	22.3%	16.3%	16.1%	13.2%

Table 4.2: Variation (standard deviation of differences divided by mean concentration) measured using the Bland-Altman method and static conditions CRLBs for both left and right VOIs.

dynamically updating first order shims in multiple regions, excellent spectra from bilateral motor cortex VOIs are achievable at 7 T. In addition, neurochemical profiles from these spectra contained 13 individual and 3 combined metabolites and were consistent with previous biochemical and MRS literature (see below). Notably, this study was accomplished without B_1^+ shimming and/or second order or higher B_0 shim manipulations thereby allowing facilities not equipped with multiple channel transmit or other specialized hardware to acquire high-quality spectra in two brain regions concurrently. As most of the, currently more than sixty, 7 T research centers [82] do not have access to B_1^+ shimming in the human brain and/or pre-emphasis of higher order shim coils, a more pragmatic approach may be desirable for most centers.

It has been shown that the electromagnetic wave behavior of B_1 for volume coils at 7 T inside a human head is non-uniform and that the bright center region results in B_1^+ degradation in the motor cortex [84]. Therefore, in order to achieve sufficient B_1^+ (23 µT which is required for our adiabatic pulses) for MRS localization in the bilateral hand areas of the motor cortex, the B_1^+ field was optimized by proper placement of dielectric pads. As illustrated in Fig. 4.2, barium titanate dielectric pads result in slightly increased B_1^+ inhomogeneity within the voxels. While this is not desirable, increasing B_1^+ efficiency outweighs the increased inhomogeneity [101]. The dielectric pad provided satisfactory B_1^+ for spectroscopy at 7 T in the motor cortex. The RTE achieved is similar to previous MRS studies in the hand area of the motor cortex at 7 T: transceiver array coils driven by multichannel transmit system (local B_1^+ shimming) achieved an RTE of 1.31 $\pm$ 0.1 [134] and an ROI and coil setup very similar to ours determined a peak RTE of 1.5 [124]. As dielectric pads result in a B_1^+ 'hot spot' and decreased efficiency away from the pad, acquisition from voxels that are further apart than performed in this study may not be feasible (e.g. one voxel near the front of the brain and one near the back).

For this study, the semi-LASER sequence was chosen over STEAM or PRESS as

the adiabatic refocusing pulses provide high B_1^+ insensitivity, a desirable slice selection profile and a minimal chemical shift displacement error (CSDE) [29, 116]. Previous multi-voxel MRS studies borrowed elements of multi-slice imaging where multiple voxels are excited in a single TR [117, 118]. Adiabatic inversion pulses of semi-LASER are SAR intensive at 7 T and, as a result, only a single voxel can be excited every 7 s. Consequently, the technique presented here provides temporal interleaving rather than a decrease in total acquisition duration. Therefore, this technique supports functional studies that require temporal resolution on the order of minutes and spectra from more than one brain region. For 7 T research centers that do not have access to specialized shim equipment, this technique presents a practical solution. Using a long TR resulted in a sufficient recovery time to avoid mutual saturation of voxels. Previously reported values for water T_1 in GM, WM and CSF at 7 T suggest an average T_1 in our VOIs of 1.63 s, therefore we would expect approximately 99% of our magnetization to return to equilibrium by the end of each TR [135, 136].

To benefit from chemical shift dispersion at UHF, efficient B_0 shimming is very important. In the authors' experience it was found that imaging based shimming methods (GRE-SHIM) are well suited to large volumes of interest, and FASTMAP to small VOIs and while this has never been systemically investigated, it has been shown that using FASTMAP results in a water resonance shift and increased line broadening towards the periphery of the shimming [137]. However, our protocol of GRE-SHIM requires all shim currents to be determined together whereas FASTMAP allows optimization of first or second order shims separately. Therefore, in this study, a hybrid GRE-SHIM/FASTMAP shimming approach was used for DSU.

The spectral quality achieved (high SNR, excellent localization performance, efficient water suppression and a distortion-free baseline) allowed reliable quantification of 13 individual and 3 combined metabolites with LCModel analysis. The CRLBs for the dominant metabolites (e.g. NAA, tCr, tCho, mIns, Glu) were below 5% and

were comparable with those obtained previously at 7 T in the motor cortex [134]. The CRLBs for all other metabolites were below 30%. The Bland-Altman analysis revealed an excellent agreement in the neurochemical profiles between DSU and static acquisition schemes. For Lac, the large agreement error may be explained by the presence of overlapping lipid peaks that result in large differences in LCModel outputs. While there are no significant hemispheric or acquisition differences for individual metabolites, there are a few trends. The static technique reports lower NAA+NAAG and Cr+PCr for both VOIs – though the difference is a relatively small amount. These tendencies may be caused by subtle differences in linewidths between VOIs or acquisition schemes – which could give rise to an unpredictable bias in LCModel outputs [138]. Line broadening of up to 4 Hz was performed on the raw spectra prior to LCModel to check if linewidth differences were an issue but we found that line broadening had virtually no effect on the resulting neurochemical profile (results not shown).

In order to obtain accurate absolute quantification of metabolites, partial volume effects must be included – otherwise artificial deviations in metabolite concentrations may be overlooked. The most commonly employed correction method scales uncorrected metabolite values by the CSF percentage in the VOI - as no relevant metabolites (apart from Gln) exist in the CSF [139]. This method does not include differences in the relative amounts of GM to WM and, used on its own, can lead to less accurate quantification of certain metabolites [140, 141]. Regrettably there is currently no consensus on the best method to correct for relative amounts GM or WM and there are a variety of techniques employed [142, 143]. We chose to use the method of Dou *et al.* [132] as the only assumption made is that metabolite concentrations are linearly dependent on tissue composition.

Our neurochemical profile findings from the human primary motor cortices were in agreement with previous postmortem studies of individuals, whereas previous *in-vivo*

MRS studies differ slightly from those reported here. For instance, the absolute NAA (9.3-9.7 µmol/g), NAAG (2.0-2.3 µmol/g), Glu (6.0-6.4 µmol/g) and Asp (1.1-1.6 µmol/g) concentrations quantified from the 8 ml VOIs were similar to those measured from postmortem human brain (NAA 7.4-9.4 µmol/g, NAAG 1.4-1.6 µmol/g, Glu 6.0-7.0 µmol/g, Asp 1.3-1.6 µmol/g) [144]. However, the GABA (1.2-1.5 µmol/g) and the Gln (2.6-2.7 µmol/g) concentrations reported here are lower than from postmortem human brains (GABA 1.97 µmol/g [145], Gln 4.5-4.9 µmol/g) though this discrepancy is almost certainly due to an increase of GABA [146] and Gln [147] in the postmortem human brain. The slight difference observed between the concentrations reported in this study and those reported in previous MRS studies is partly due to the fact that the concentrations we report were not corrected for T_2 values of individual metabolites. Additionally, differences in relative amounts of GM to WM also contributed to this difference since the VOIs used in this study contain more GM (0.30 compared with 0.19) and less WM (0.63 compared with 0.73) [134].

This study does not include DSU of the higher order shims as the rapid altering of the unshielded and uncompensated higher order shims generates eddy currents that result in strong field variations that can take 3-10 seconds to disappear [148, 149]. As the majority of the 7-second TR is spent waiting (due to SAR limitations), it may be possible to include DSU of the higher order shims without requiring pre-emphasis. This would improve linewidths and may be required for areas of the brain that are more difficult to shim (e.g. near the nasal cavity) but would require investigating the eddy current decay time on a system specific basis.

This technique lends itself to functional spectroscopy applications requiring high spectral resolution in multiple brain regions. Acquiring data from more than one region in an interleaved fashion is vital in allowing the study of any intervention that modulates the brain with a timescale of minutes to hours and could reasonably be expected to involve more than one brain region. Three immediate applications might

be as follows: (1) To study the neurochemistry of pharmacological interventions, where the temporal dynamics of induced changes in neurotransmitters might well be expected to be different across the brain, and this information would be very important in understanding the brain's response [150]. (2) To examine the response to short-term stimuli, such as a tonic pain stimulus, where multiple brain regions would be expected to respond, but in different directions and with different temporal dynamics. Understanding these responses, and therefore how the brain regions might interact, would be very important in understanding the mechanisms underlying the cortical pain response, for example [151]. (3) To study neurotransmitter changes during plasticity-induction, for example learning or brain stimulation. In the context of the motor system, for example, it is well known that plasticity does not only occur in the directly involved network node (usually primary motor cortex, M1), but rather occurs between and within the directly involved network node and the rest of the functional network. Understanding the time courses of changes occurring at these remote sites, and how they interact with M1 is of vital importance in understanding plasticity and learning in humans [152, 153].

In conclusion, the present study provides an effective method for acquiring high-quality spectra at UHF in multiple brain regions concurrently within a single session – without additional specialized hardware. The outlined acquisition scheme acquired neurochemical profiles from both motor cortices with accurate quantification of 13 individual and 3 combined metabolites.

Chapter 5

Modulation of Cortical Neurotransmitters by Transcranial Direct Current Stimulation of the Human Motor Cortices

5.1 Introduction

Transcranial direct current stimulation (tDCS) is a non-invasive brain stimulation technique that applies weak DC current (1-2 mA) delivered to the brain area of interest via small electrodes placed on the scalp. tDCS has polarity-dependent effects on the brain, depending on the orientation of electrodes and direction of current. In animals and humans, anodal stimulation increases neuronal excitability in the area around the location of stimulation whereas cathodal stimulation decreases neuronal excitability [154, 155]. During anodal stimulation current flows from the anode, placed over the area of interest, to a reference electrode (cathode) whereas during cathodal stimulation the anode and cathode are switched and the current flows in the opposite

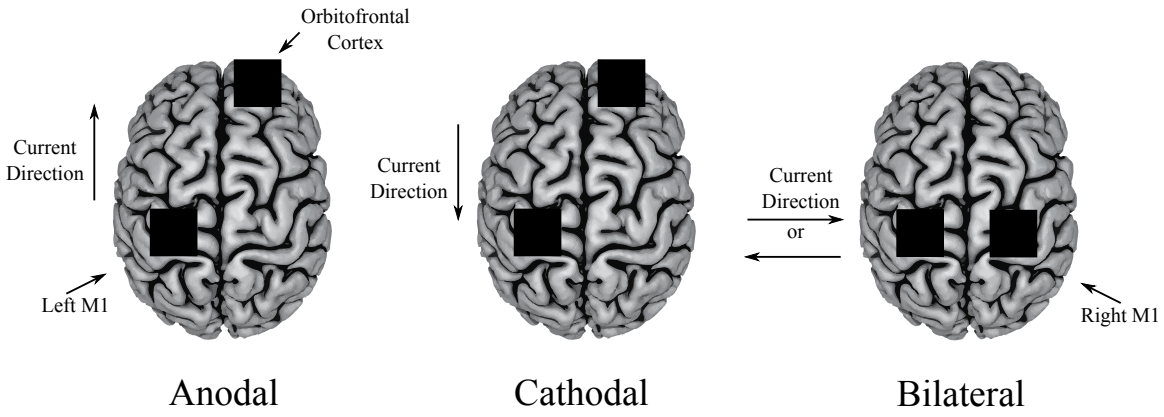


Figure 5.1: tDCS electrode placement for anodal, cathodal and bilateral tDCS. For our study current flowed from the left M1 to the right M1.

direction. When applying tDCS to the primary motor cortex (M1), the electrode of interest is placed on the scalp over the M1 of interest and the reference electrode is typically placed over the orbitofrontal cortex contralateral to the M1 of interest. Another electrode configuration, referred to as bilateral stimulation [156], places both electrodes over each M1. Fig. 5.1 illustrates common tDCS electrode placement locations. Anodal, and to a lesser extent cathodal, tDCS of the M1 has been shown to improve motor performance and motor learning in both healthy controls [157, 158] and after stroke [159], suggesting its potential use as a tool to modulate plasticity. However, the pathways by which specific neurochemicals might mediate the tDCS-induced changes are not fully understood.

Pharmacological studies in humans have shown that tDCS changes are modulated by both glutamate and GABA [160, 161]. As MRS is currently the only technique capable of non-invasive direct measurements of *in-vivo* glutamate and GABA levels, MRS is an ideal tool to examine cortical neurotransmitters following tDCS. Previous MRS studies have shown that anodal tDCS decreases M1 GABA levels for at least 20 minutes after cessation of stimulation [162, 157]. Cathodal tDCS reduces both Glx (composite peak comprised of glutamate and glutamine) and GABA concentrations [162]. In one study, anodal tDCS to the right frontal lobe was shown to significantly

increase *myo*-inositol content [163]. However, the physiological significance of this *myo*-inositol change is unclear. It has been proposed that simultaneous application of both anodal and cathodal tDCS over each M1 could produce benefits greater than its constituent unilateral tDCS interventions [164, 165]. However, results of bilateral stimulation are heterogeneous [166, 167, 168] and the direct changes to brain metabolites are unclear.

The effects of anodal and cathodal tDCS on the excitability of the stimulated hemisphere are well established [154, 160]. However, the effects on the non-stimulated hemisphere are not routinely investigated. Likewise, MRS studies investigating the neurochemical changes associated with tDCS have focused on acquiring spectra from only the stimulated M1; very few studies have examined the neurochemical changes occurring in the non-stimulated hemisphere [169]. This is largely due to methodological limitations of MRS, as GABA has historically been difficult to quantify accurately and quickly (Sec. 2.6.4). While there are a number of spectral editing techniques including MEGA [53], multiple-quantum-filters [170] and 2-D spectroscopy [171] that can accurately determine the GABA concentration at 3 T, they generally focus on only one region of the brain at a time. The increased spectral resolution and signal-to-noise ratio (SNR) at 7 T allows for more accurate GABA measurements [110] and the acquisition scheme outlined in Chapter 4 provides a novel method to measure not only GABA and glutamate but a total of 13 individual and 3 combined metabolites concurrently from both M1s. This method gives the unique opportunity to determine the neurochemical changes induced by tDCS in the previously neglected M1.

5.2 Experimental

Subjects

Twelve healthy participants [2 male; aged 20-32 years, mean 25 years] participated in the study after giving informed consent in accordance with ethical approval from the East London Research Ethics Committee (Ref: 10/H0703/50). All were right-handed as assessed by the Edinburgh Handedness Inventory [172].

Experimental design

All subjects participated in four testing sessions comprised of either anodal, cathodal, bilateral tDCS or a sham condition. For the sham condition the electrodes are placed in a manner identical to the anodal/cathodal condition but the DC stimulator is switched off after a initial ramp-up period of 10 seconds (as described previously [157]). With the exception of a tingling sensation during the ramp-up period, subjects rarely experience any other sensations and this has previously been shown to be an acceptable sham condition [173]. Two subjects did not complete the bilateral condition due to personal time constraints. All sessions were separated by at least one week and the order of the sessions was counterbalanced across the group. In each experimental session, measurements of neurochemicals were acquired at five time points: at baseline, during tDCS, and at three time-points post-tDCS (15 minutes or post-tDCS 1, 30 minutes or post-tDCS 2, and 45 minutes or post-tDCS 3). Hence a total of 460 spectra were acquired (5 time-points from each hemisphere for 4 sessions per subject for 10 subjects and for 3 sessions per subject for 2 subjects). Subjects watched a wildlife or dinosaur documentary for the entire duration of the experiment.

Transcranial direct current stimulation (tDCS)

A DC-Stimulator (Magstim, Ltd; UK) delivered a 1 mA current to the scalp via electrodes measuring 5 × 7 cm (Easycap, GmbH; Germany). The active electrode was centered over the left M1. For the anodal, cathodal, and sham conditions, the reference electrode was placed over the contralateral supraorbital ridge. For the bilateral condition, the anode was placed over the left M1 and the cathode over the right M1. High Chloride Electrolyte-Gel (Easycap, GmbH; Germany) was used as the conducting medium between the scalp and electrodes. For the anodal, cathodal and bilateral conditions the current was ramped up over 10 seconds and held at 1 mA for 10 minutes before being ramped down over 10 seconds. As described above, for the sham condition the current was ramped up over 10 seconds before being switched off.

MR Protocol

All measurements were acquired using the interleaved 2-voxel MRS acquisition scheme described in Chapter 4. All measurements were performed on a 7 T Siemens scanner (Siemens, Erlangen). A dielectric pad was placed on the scalp (in the same manner as the previous chapter) to increase B_1^+ in the VOIs. In order to verify that adequate and normalized transmit power had been achieved with the dielectric pads, B_1 maps were acquired using the actual flip angle imaging (AFI) sequence [123] (field of view, 240 × 240 mm^2 ; TR1/2 = 6/30 ms; TE = 2.58 ms; slice thickness 2.5 mm; non-selective flip angle 60°, scan time 3 minutes). When necessary, the dielectric pad was re-positioned and the B_1 map repeated to achieve the best B_1 efficiency in the VOI. To aid in selecting the regions of interest, structural 3D T_1-weighted images were acquired with an MP-RAGE sequence [125] (field of view, 192 × 192 mm^2; TR = 2.2 s; TE = 2.82 ms; slice thickness 1 mm; slices 96; non-selective inversion; scan time 3 minutes) for all subjects. All spectra were localized using semi-LASER as described

in the previous Chapter. 64 averages with an echo time of 30 ms and repetition time of 7 s were acquired for each of the five time points: baseline, during tDCS, post-tDCS 1, post-tDCS 2, and post-tDCS 3. Water unsuppressed spectra (both with and without VAPOR gradients) were acquired once before application of tDCS and once at the end of post-tDCS 3. The water unsuppressed spectra were used for eddy current corrections, linewidth measurements, to account for subject movement and to confirm that creatine provided a stable reference compound (see below). Signal was acquired from two voxels in an interleaved fashion from the left and right motor cortex with a voxel size of $20 \times 20 \times 20$ mm^3 and average distance of 40 mm between voxel edges.

Processing of MR Spectra

The spectra were processed in the same fashion as described in Sec. 4.2 except the criteria for spectral rejection was modified. For this chapter the maximum Cramér–Rao lower bound (CRLB) was relaxed from 30% to 50%. The motivation for this change was that a threshold CRLB of 30% may cause biases in metabolites concentrations as recently pointed out by Kries [174]. In addition to relaxing the CRLB threshold we have also included a new criterion for spectral rejection: water linewidths at full width at half maximum (FWHM) must be less than 15 Hz.

Statistical Analysis

Statistical analyses on the data were conducted using SPSS (Version 22, IBM). Based on previous MRS studies of tDCS, the metabolites of interest are GABA, glutamate (Glu) and *myo*-inositol (*myo*-Ins) with concentrations reported as a ratio to the total creatine (Cr+PCr). We chose to use creatine as a reference compound over water in order to facilitate comparison with previous studies as nearly all previous MRS GABA studies use creatine as a reference [153]. To control for any between-session

differences, the absolute change in neurochemical concentrations from the baseline value and each time point after were calculated for GABA, Glu, and *myo*-Ins for both the left and right M1. For each neurochemical, a Repeated Measures ANOVA (RM ANOVA) was run with one factor of stimulation (anodal, cathodal, bilateral, sham), and one factor of time (during tDCS, post-tDCS 1, post-tDCS 2, and post-tDCS 3). Subsequently, a RM ANOVA was performed to test each real stimulation condition (anodal, cathodal, bilateral) separately against the sham condition, with one factor of stimulation and one factor of time. In each case, the main result of interest is a main effect of stimulation.

5.3 Results

Spectral Quality

Fig. 5.2 shows the average baseline (prior to tDCS application) spectra from all conditions in all subjects. We achieved excellent spectral resolution as in the previous chapter. Water suppression was effective for all subjects and conditions though a Hankel-Lanczos singular value decomposition (HLSVD) [66] filter was used to remove any residual water signal. Measured water linewidths (FWHM) were 12.6 $\pm$ 1.5 Hz for the left M1 and 12.8 $\pm$ 1.4 Hz for the right M1 and were not significantly different between the VOIs (paired t-test, 2-tailed, p-value > 0.1). Based on our spectral rejection criteria, out of 460 acquired spectra, a total of 15 GABA measurements were excluded due to high CRLBs and 2 complete spectra were excluded due to large linewidths. All but 3 of these occured during the last time-point. Table 5.1 shows the average CRLBs for the metabolites of interest.

	Left M1 CRLBs (%)	Right M1 CRLBs (%)
GABA	20.0 ± 8.2	17.0 ± 6.5
Glu	2.9 ± 0.6	3.2 ± 0.7
myo-Ins	2.4 ± 0.7	3.1 ± 0.9

Table 5.1: The average (± standard deviation) CRLBs for GABA, glutamate (Glu), and *myo*-Inositol (*myo*-Ins) in the left and the right M1 over all subjects and conditions.

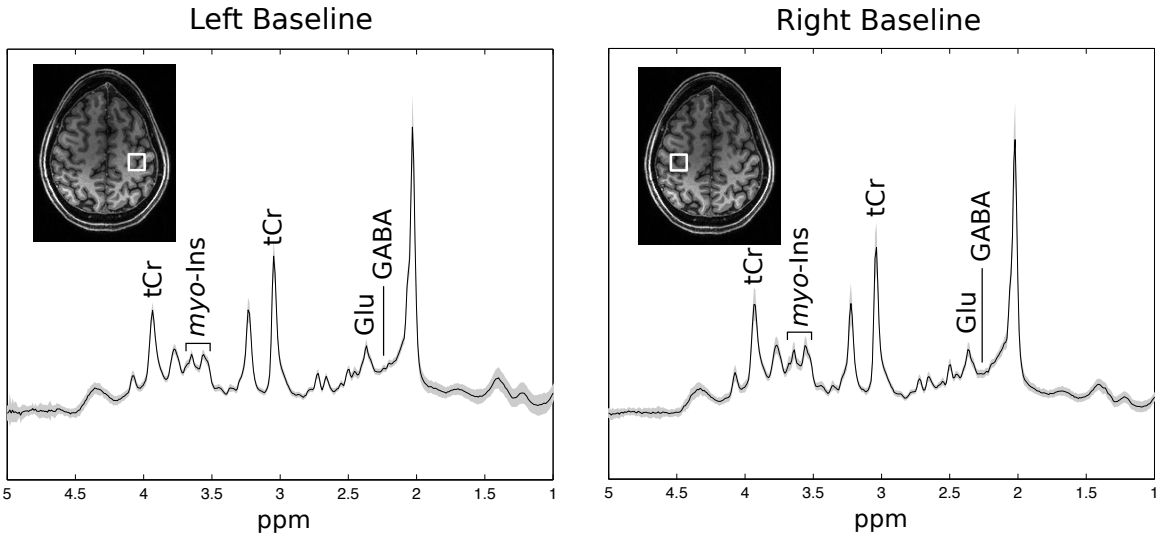


Figure 5.2: Average *in-vivo* ^{1}H semi-LASER spectra (TR = 7 s; TE = 30 ms; Averages = 64) from all subjects and conditions from both VOIs at baseline (prior to application of tDCS). The shaded grey area is the standard deviation.

Reference Conditions

In order to establish confident reference conditions we tested for any differences between baseline time-points (before tDCS was turned on) for each stimulation condition and hemisphere by performing a RM ANOVA with one factor of stimulation and one factor of hemisphere for each metabolite (GABA, Glu and *myo*-Ins). We found no significant effects of pre-stimulation levels of GABA, Glu and *myo*-Ins (all p-value > 0.1) but there was a significant difference between hemispheres at baseline for metabolites GABA ($F_{(1,7)} = 121.26$, p-value < 0.001) and Glu ($F_{(1,9)} = 82.76$, p-value < 0.001) but not *myo*-Ins (p-value > 0.1). We found that the right M1 showed consistently higher values for GABA and Glu when compared with the left. In order to control for any possible systematic baseline differences between the left and right M1s, we used the absolute change in neurochemical concentrations from baseline for all further analyses.

We also performed a RM ANOVA for the sham session with factors of time (baseline, during tDCS, post-tDCS 1, post-tDCS 2, and post-tDCS 3) and hemisphere for each metabolite. We found no significant effects of time or hemisphere for either Glu or *myo*-Ins (all p-value > 0.1). We did, however, find a significant increase in GABA ($F_{(3,27)} = 3.01$, p-value $= 0.05$) in the sham condition over time but no significant effects between M1s.

Stimulation Analysis

With the reference and baseline conditions established, we went on to investigate the effects of tDCS. To do so we began by testing the changes in GABA, Glu and *myo*-Ins for each real stimulation condition against the sham by performing RM ANOVAs (sham and anodal, sham and cathodal, sham and bilateral) with one factor of stimulation and one factor of time (during tDCS, post-tDCS 1, post-tDCS 2, and post-tDCS 3). The results are presented below and, as we were interested in the

change occurring with real stimulation compared to the sham condition, all time-course data are presented as the percentage change from baseline corrected to the sham condition, *i.e.* the sham condition time-course is considered our baseline.

Anodal Stimulation

We found significantly lower GABA levels after anodal stimulation compared with the sham condition. A RM ANOVA with one factor of stimulation and one factor of time demonstrated a significant main effect of stimulation in both the stimulated M1 ($F_{(1,8)} = 8.03$, p-value $= 0.02$) and non-stimulated M1 ($F_{(1,11)} = 7.90$, p-value $= 0.02$). We determined that no significant effects were caused by stimulation in either M1 for Glu or *myo*-Ins (all p-value > 0.05). We found a correlation between the decrease in GABA in the stimulated M1 and the decrease in GABA in the non-stimulated M1 for both the post-tDCS 2 (R $= 0.66$, p-value $= 0.02$) and post-tDCS 3 time-points (R $= 0.64$, p-value $= 0.03$).

Cathodal Stimulation

A RM AVOVA for the cathodal condition, with one factor of stimulation and one factor of time, revealed no significant main effect of stimulation for both GABA and Glu in the stimulated M1 (p-value > 0.1). However we did find a significant decrease in both GABA ($F_{(1,9)} = 13.11$, p-value < 0.01) and Glu ($F_{(1,11)} = 4.98$, p-value < 0.05) in the non-stimulated M1. Just as with anodal stimulation we again found that stimulation had no observed effect on *myo*-Ins levels in either M1 (p-value > 0.05).

Bilateral Stimulation

For the bilateral stimulation condition a RM ANOVA with one factor of stimulation and one factor of time revealed no significant effects on GABA concentration in the

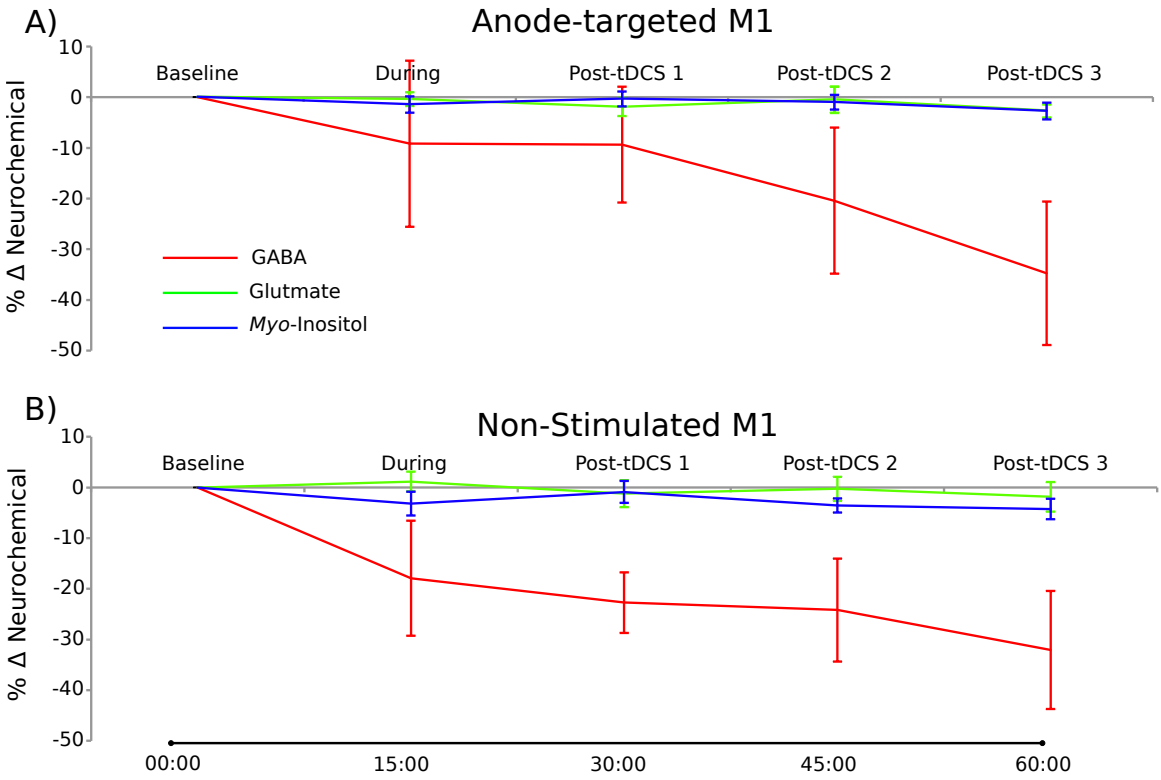


Figure 5.3: Effects of anodal stimulation on cortical neurotransmitters in both M1s. Mean percentage change in neurochemicals from baseline corrected to the sham condition for A) anode-targeted (stimulated) M1 and B) non-stimulated M1. Error bars are standard error of the mean. Figure adapted from Bachtiar DPhil Thesis 2015.

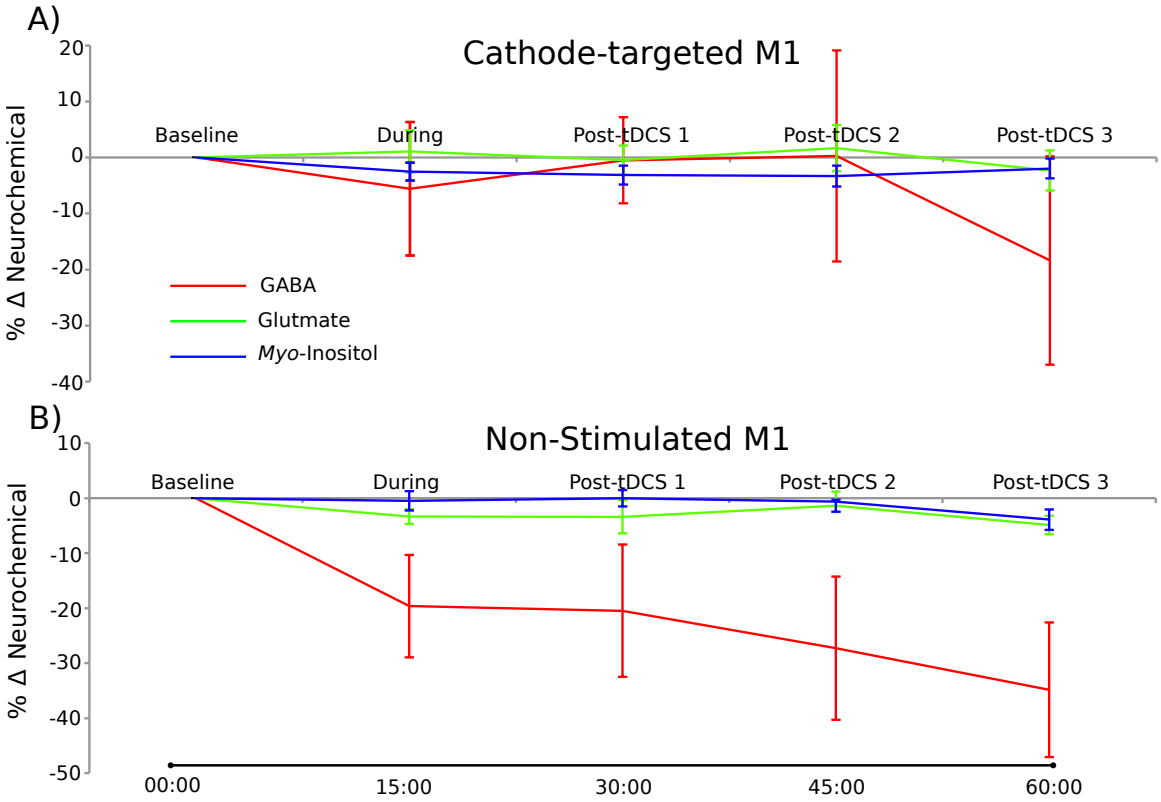


Figure 5.4: Effects of cathodal stimulation on cortical neurotransmitters in both M1s. Mean percentage change in neurochemicals from baseline corrected to the sham condition for A) cathodal-targeted (stimulated) M1 and B) non-stimulated M1. Error bars are standard error of the mean. Figure adapted from Bachtiar DPhil Thesis 2015.

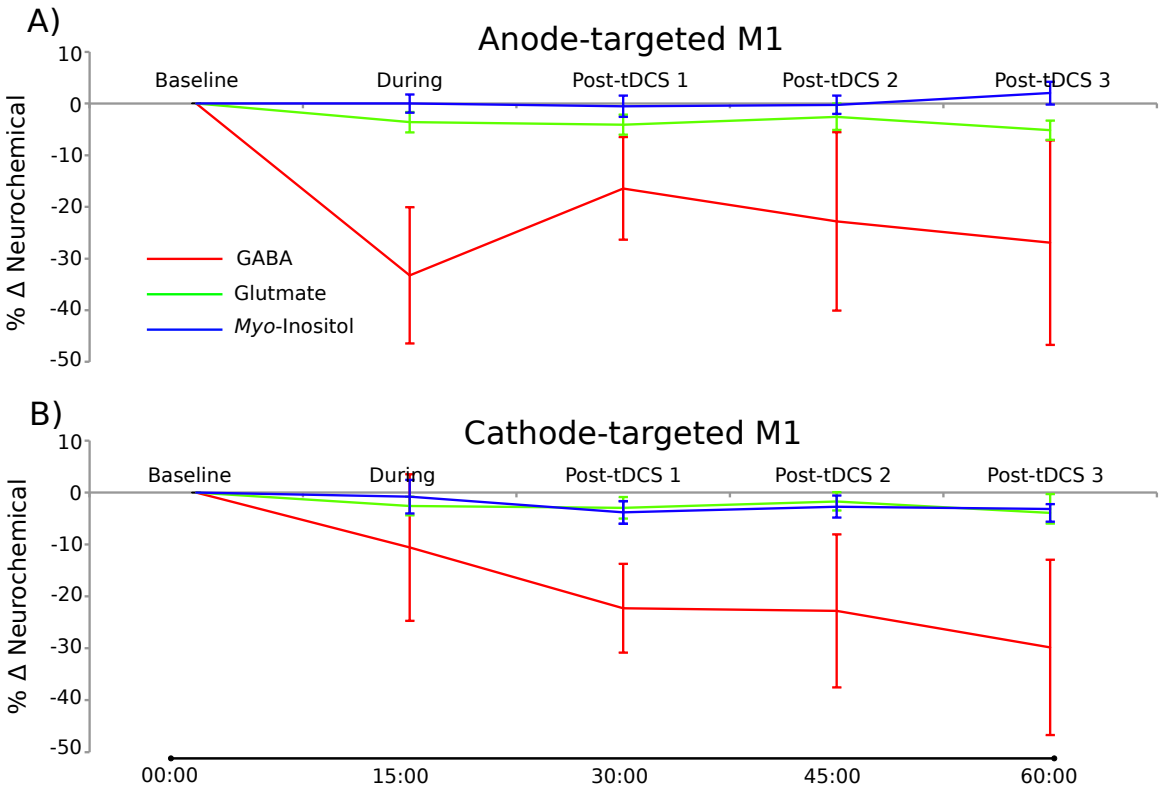


Figure 5.5: Effects of bilateral stimulation on cortical neurotransmitters in both M1s. Mean percentage change in neurochemicals from baseline corrected to the sham condition for A) anodal-targeted M1 and B) cathodal-targeted M1. Error bars are standard error of the mean. Figure adapted from Bachtiar DPhil Thesis 2015.

anode-targeted M1 ($F_{(1,7)} = 1.60$, p-value $= 0.25$) and a trend towards a decrease in the cathode-targeted M1 ($F_{(1,9)} = 4.47$, p-value $= 0.06$). We also found significantly decreased Glu levels in both the anode- ($F_{(1,9)} = 6.46$, p-value $= 0.03$) and cathode-targeted ($F_{(1,9)} = 5.21$, p-value < 0.05) M1s. Once again we found no observed effect on *myo*-Ins levels in either M1 (p-value > 0.1).

We wanted to determine whether the changes in GABA in the bilateral condition could be predicted from our results from the constituent unilateral anodal and cathodal stimulation. We performed a linear regression analysis on the overall change (average of post stimulation time-points) for each unilateral and bilateral condition. We found that the change in GABA in the unilateral anodal-targeted M1 predicted the change found in the bilateral anodal-targeted M1 (adjusted R square $= 0.40$,

$F_{(1,8)} = 6.90$, p-value = 0.03, β = -0.68) but that the unilateral cathode-targeted M1 did not predict the change in GABA (p-value > 0.1) for the bilateral stimulation.

5.4 Discussion

The purpose of this study was to investigate the effects of anodal, cathodal and bilateral stimulation on the concentrations of GABA, Glu and *myo*-Ins in both motor cortices concurrently. We have reproduced previous results and demonstrated that anodal tDCS reduces GABA in the stimulated M1 for at least 30 minutes after stimulation. We demonstrate, for the first time, a decrease in GABA and glutamate in the non-stimulated M1 following cathodal stimulation. In every tDCS condition there were no significant changes in *myo*-Ins levels. Though a previous study did show a large increase in *myo*-Ins levels in the frontal lobe after anodal stimulation [163], differences in brain region and stimulation parameters make these findings difficult to reconcile. Additionally, the physiological basis for how or why DC current may affect *myo*-Ins is not well understood.

The significant difference in metabolite concentrations between hemispheres was surprising; especially as the study in the previous chapter did not show any significant lateral asymmetry in any metabolites using effectively the same acquisition conditions (same subject handedness and approximate gray/white matter fractions). To investigate possible explanations we looked at the difference between the average baseline concentrations (prior to tDCS application) from each M1. We found that tCr levels are slightly higher in the left VOI which is consistent with previous MRS studies [175]. As we used tCr as a reference compound for this study but not in the previous chapter, this could explain part of the increase in Metabolite:tCr ratios found in the right VOI. After correcting for tissue composition and referencing to an unsuppressed water peak, we found that the difference in LCModel outputs of creatine between

VOIs at baseline were not statistically significant (left: 16.4 ± 2.9 mmol/g; right: 16.3 mmol/g ± 2.9, p-value > 0.1) and, since there was only a relatively small difference in peak height, this cannot be the only cause for the difference. For GABA (left: 2.6 ± 0.8 mmol/g, right: 5.0 ± 1.7 mmol/g) lateral asymmetry is also supported by a previous post-mortem study that showed a right M1 GABA bias [176]. The same study also showed a correlation between left-right asymmetries for GABA and glutamate decarboxylase (GAD). As GAD is the catalyst required for synthesis of GABA from Glu, we could also expect elevated Glu levels in the right M1.

Stagg *et al.* previously reported, using the same tDCS parameters, a similar decrease in GABA in the stimulated M1 as we report here [157, 162]. Here we also report, for the first time, that the GABA decrease at later time-points (10-20 minutes after tDCS) is correlated with a decrease in GABA in the non-stimulated M1. This is largely supported in a recent study in which motor evoked potential (MEP) amplitude increased in both hands following anodal tDCS, indicating an increase in excitability in both M1s [168]. Previous studies on the behavioural effects of anodal tDCS on healthy controls have shown that the degree of motor learning is related to the degree of tDCS-induced GABA decrease [157] though previous studies have only investigated the stimulated M1. As GABA levels were measured at rest, the behavioural relevance of the GABA decrease in the non-stimulated M1 observed in this study is unclear and should be investigated in future studies.

Interestingly our cathodal results do not agree with those reported previously by Stagg *et al* [162]. They reported a significant decrease in both GABA and Glx (glutamate and glutamine composite peak) in the stimulated M1. If the excitability effects are due to GABA alone, we would expect an increase in GABA in the stimulated M1 following cathodal tDCS. Hence both their results and those results reported here appear to contradict the neurophysiological effects of cathodal tDCS, which has been reliably shown to decrease excitability [154]. O'Shea *et. al* also predict an increase

of GABA in the stimulated M1 and a decrease in the non-stimulated M1 [168]. Our non-stimulated M1 results agree though in the stimulated M1 there is, again, a discrepancy. Future studies are needed to elucidate the disagreements though it appears that GABA is not the only metabolite involved with excitability modulation following cathodal tDCS.

As there are no previous MRS studies of bilateral tDCS, we did not have any strong predictions concerning the effects of bilateral stimulation on M1 neurotransmitters other than a hypothesis derived from combining the effects of anodal and cathodal unilateral tDCS. Curiously, we found no significant changes in GABA with bilateral stimulation though we did demonstrate a decrease in glutamate concentration in both M1s. When we tested our GABA results to determine whether the responses in the bilateral condition could be determined by the responses in the unilateral anodal and cathodal conditions, we found that this was true for the anode-targeted M1 but not for the cathode-targeted M1. The source of this discrepancy may also be the cause of the heterogeneity of GABA predictions found in the unilateral cathodal condition. How the bihemispheric current exerts its effects on each M1, and on the interactions between the two M1s will need to be tested in future studies.

Chapter 6

Refocusing *J*-modulation

6.1 Introduction

6.1.1 Short Vs. Long Echo Time Spectroscopy

In a conventional PRESS, STEAM or semi-LASER experiment, signal from scalar-coupled resonances decreases rapidly with echo time due to destructive interactions between those J-coupled resonances (J-modulation). Therefore, a short-TE experiment is usually employed to obtain adequate SNR for the case of coupled resonances. However, short-TE *in-vivo* proton spectra typically include a broad baseline consisting of signals from macromolecules and lipids (as discussed in Sec. 2.7) which complicate analysis of the spectrum and can result in decreased quantification precision [59]. As these broad resonances possess a much shorter T_2 than metabolites, waiting for a longer echo time can result in minimal macromolecule and lipid contamination. Depending on the application, echo times for long echo time spectroscopy typically range from 90-200 ms [177]. As a result of J-modulation and T_2 relaxation it is difficult to detect coupled metabolites at long echo time. Nevertheless, there are a number of pulse sequences designed to detect specific coupled resonances by acquiring signal when the peak of interest is either fully upright or fully inverted [178, 179]. There

are also many techniques designed to exploit J-coupling to isolate coupled spins that are overlapped by more intense signals, e.g. MEGA, or multiple-quantum filters (see Sec. 2.6.4) [53, 180].

In ideal experimental conditions the macromolecule and lipid signals can be accurately simulated using prior knowledge resulting in unbiased metabolite measurements [59]. However, in many disease conditions or for VOIs near the scalp, macromolecule and lipid signals can introduce significant signal variations which reduce the precision and accuracy of metabolite quantification [181, 182, 183]. Additionally the macromolecule baseline has been shown to vary slightly in different brain regions and with subject age [184]. Acquiring a separate, subject specific, metabolite-nulled spectrum can be used to experimentally measure the baseline signal and this has been shown to significantly reduce baseline associated errors [59]. Acquiring a metabolite-nulled spectrum can be time demanding and therefore a single characteristic macromolecule basis spectrum is commonly used for most regions of healthy brain [185]. For certain disease conditions a patient and VOI specific macromolecule basis spectrum may be required but acquiring this may not be feasible due to time or subject constraints. In these conditions long echo time spectroscopy may be preferable. Additionally, in clinical settings, long echo time spectroscopy may be preferred to short echo time due to easier data processing as at long echo time only N-acetylaspartate (NAA), creatine (Cr), choline (Ch), glutamate (Glu) and (usually) lactate (Lac) are visible.

6.1.2 Suppressing J-Modulation

The first NMR technique that provided a reduction of the effects of J-modulation is the Carr-Purcell-Meiboom-Gill (CPMG) pulse train [186, 187]. By replacing a single 180° refocusing pulse in a spin echo pulse sequence with a train of n 180° refocusing pulses, J-modulation can be suppressed so long as the inter-pulse interval τ is short relative to the chemical shift difference Δf between the coupled spins $\Delta f < 1/\tau$ [188].

For example, the coupled spins of the methine and methyl groups of Lac resonate with a difference $\Delta f = 360$ Hz at 3 T [128] which would require $\tau < 3$ ms. This would require a large amount of RF power in order to generate pulse trains long enough for the technique to fully suppress J-modulation at long echo times. CPMG based sequences have been shown to reduce the effects of J-modulation *in-vivo* at 2.0 T for echo times up to 135 ms [189] and more recently for echo times over 200 ms at 1.5 T by using composite pulses [190]. Regrettably, increasing the field strength to 3 T or greater would result in unfeasible RF power requirements and impossible sequence timing as, for example, obtaining sufficient suppression for all coupled metabolites at TE = 90 ms would require over 100 RF pulses of very short pulse duration (see Fig. 6.3).

Another pulse sequence that can remove J-modulation is the so-called perfect echo sequence [191, 192]. For an AX spin system, insertion of a 90° pulse at the midpoint of a double spin echo (*i.e* PRESS) will refocus J-modulation caused during the first half of the sequence leading to complete refocusing of J-modulation at the end of the sequence. The product operator formalism of a spin echo for two weakly coupled spins I and S (ignoring chemical shift as this is refocused for a spin echo) is:

$$\begin{aligned} I_z + S_z &\xrightarrow{90(I_x+S_x)} -(I_y + S_y) \\ &\xrightarrow{2\pi J_{IS} I_z S_z 2\tau 180(I_y+S_y)} -(I_y + S_y)\cos\theta_J + 2(I_x S_z + I_z S_x)\sin\theta_J \end{aligned} \tag{6.1}$$

where $\tau = \text{TE}/2$ and $\theta_J = \pi J_{IS}\tau$. If a 90° pulse is now applied about the y-axis we get:

$$\begin{aligned} -(I_y + S_y)\cos\theta_J + 2(I_x S_z + I_z S_x)\sin\theta_J &\xrightarrow{90(I_y+I_y)} \\ &-(I_y + S_y)\cos\theta_J - 2(I_z S_x + I_x S_z)\sin\theta_J \end{aligned} \tag{6.2}$$

so the y pulse leaves the in-phase terms unchanged but exchanges the anti-phase

terms. If we employ a second spin echo, we will refocus J-modulation:

$$-(I_y + S_y)\cos\theta_J - 2(I_zS_x + I_xS_z)\sin\theta_J \xrightarrow{2\pi J_{IS} I_z S_z 2\tau 180(I_y+S_y)} -(I_y + S_y) \qquad (6.3)$$

For a general AX_n spin system the result is a bit more complicated. The spin states at the end of a conventional PRESS sequence are:

$$-\sum_{i=1}^{N} I_y^i \cos 2\theta_J + 2\sum_{i=1}^{N}\sum_{j=i+1}^{N} (I_x^i I_z^j + I_z^i I_x^j)\sin 2\theta_{Jij} \qquad (6.4)$$

Whereas with an extra 90° J-modulation refocusing pulse:

$$-\sum_{i=1}^{N} I_y^i \left(\cos^2\theta_J + \sin^2\theta_J \cos^{N-1}\theta_J\right) + 2\sum_{i=1}^{N}\sum_{j=i+1}^{N} (I_x^i I_z^j + I_z^i I_x^j)\sin\theta_{Jij}\cos\theta_{Jij}(1 - \cos^{N-1}\theta_{Jij}) \qquad (6.5)$$

In this case J-modulation is only refocused if $N = 1$ (as already shown above) or if $\theta_J = \pi J\mathrm{TE}/2 \ll 1$ - though it has been shown that for AX_n spin systems J-modulation can still be sufficiently suppressed for echo times up to $1/4J$ [192]. For lactate $J = 6.933$ Hz [128] therefore a perfect echo sequence will sufficiently suppress J-modulation when TE < 36 ms. Lee *et al.* implemented a localized version of a perfect echo entitled JPRESS which provided J-modulation refocusing for glutamate and glutamine for echo times up to 30 ms at 1.5 and 3.0 T - though they did not show any *in-vivo* spectra [193].

Constraints on both the CPMG ($\Delta f < 1/\tau$) and perfect echo (TE < $1/4J$) sequences have limited their use for *in-vivo* spectroscopy. An elegant extension of the perfect echo was recently demonstrated in high resolution NMR, looping perfect echoes that resulted in J-refocusing for AX_n spin systems after each perfect echo so long as each echo module is shorter than $1/4J$ [20]. This sequence (PROJECT)

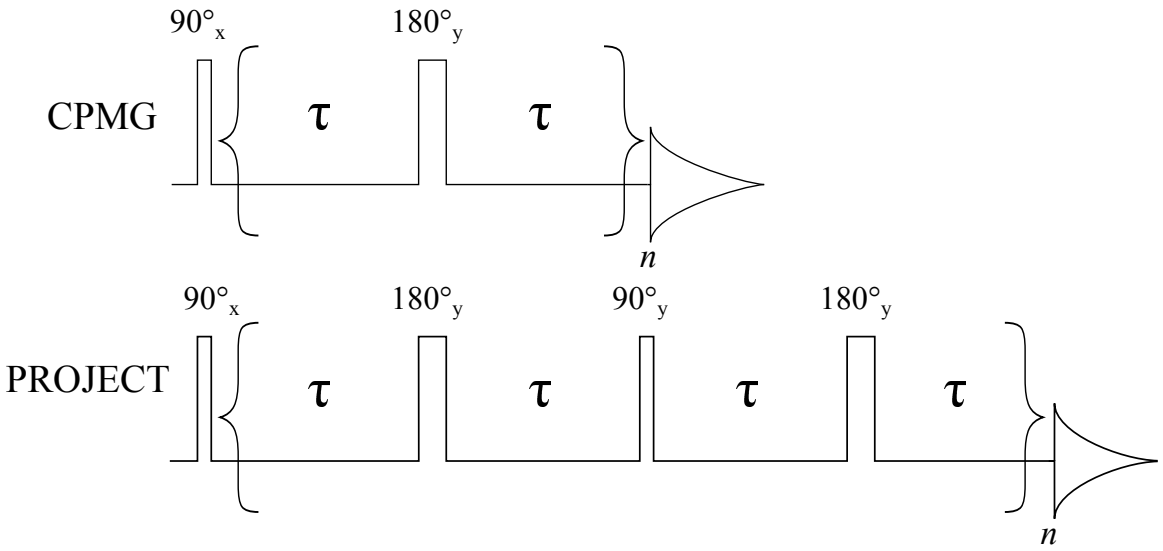


Figure 6.1: Pulse sequence diagrams for the CPMG experiment and a train of perfect echoes to refocus J-modulation (PROJECT) [20].

offers a much easier constraint to satisfy when compared with CPMG or a single perfect echo and is illustrated in Fig. 6.1 . The goal of this chapter was to implement a localized *in-vivo* implementation of PROJECT entitled PRESS with J-refocusing (PRESS-JR).

6.2 Simulations

To determine the expected behaviour using this new approach, simulations were performed comparing PRESS, CPMG and PRESS-JR. Simulations were performed using Versatile Simulation, Pulses and Analysis for Magnetic Resonance Spectroscopy (VeSPA) [70] using a density matrix representation at 3 T. Simulations of Lac, *myo*-inositol (Ins) and Glu were performed for a variety of echo times and refocusing units. These metabolites were chosen to provide a range of coupling strengths and chemical shift differences. To demonstrate their difference in modulation behaviour, a simulation of PRESS with ideal pulses for a number of echo times is illustrated in Fig. 6.2. Note that Lac undergoes simple, periodic modulation, while the modulation

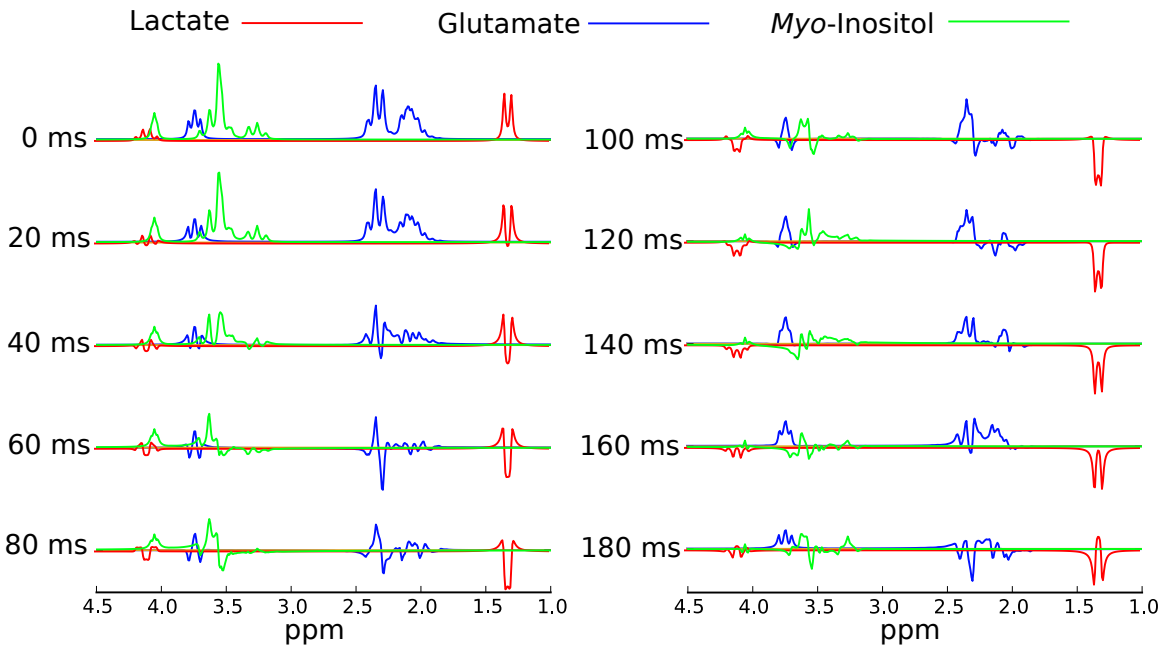


Figure 6.2: Simulation of lactate, glutamate and *myo*-inositol with a conventional PRESS sequence for a number of echo times. Field strength: 3 T; Number of points: 2048; Spectral width: 3000 Hz; Line-broadening: 6 Hz.

patterns of Glu and Ins are much more complicated and will never fully invert. Fig. 6.3 shows a comparison on the effectiveness of CPMG and PRESS-JR in suppressing J-modulation at TE = 90 ms. On the left are integrals of Glu, Lac and Ins as a function of the number of refocusing units. While both techniques will sufficiently suppress Ins modulation after approximately the same number of units (or pulses), CPMG struggles for Glu and Lac requiring over 50 additional pulses before reaching the same suppression efficiency as PRESS-JR. Employing this many pulses within a 90 ms echo time is unfeasible *in-vivo*, as the pulse durations would have to be much shorter than currently possible. The spectra on the right of Fig. 6.3 demonstrate the difference in modulation suppression between CPMG and PRESS-JR after only 3 refocusing units. As expected from the integrals, for all three metabolites PRESS-JR provides nearly complete J-modulation refocusing but CPMG has significant modulation for Lac and Glu as for these metabolites the CPMG condition for J-modulation is not satisfied ($\Delta f > 1/\tau$). One can extend this behaviour to other echo times by

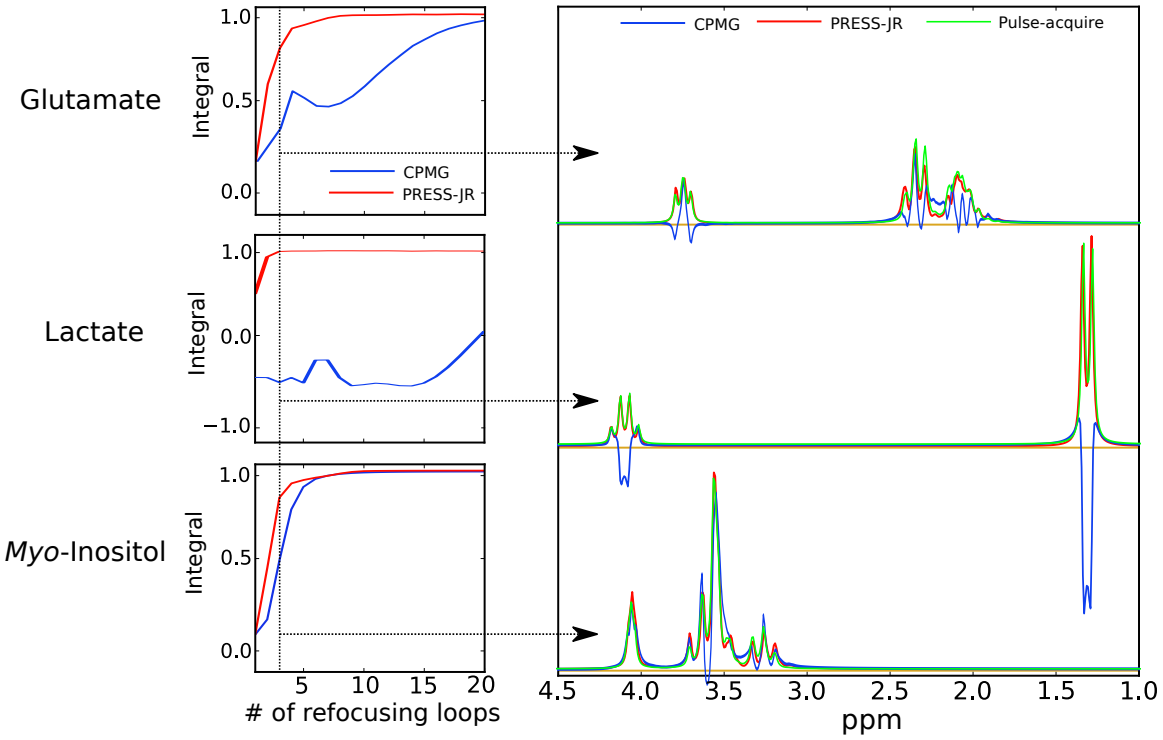


Figure 6.3: Simulations of integrals for TE = 90 ms as a function of # of refocusing loops for CPMG and PRESS-JR. Note that PRESS-JR has almost no J-modulation for all three metabolites after only 3 refocusing units. Field strength: 3 T; Number of points: 2048; Spectral width: 2000 Hz; Line-broadening: 4.5 Hz.

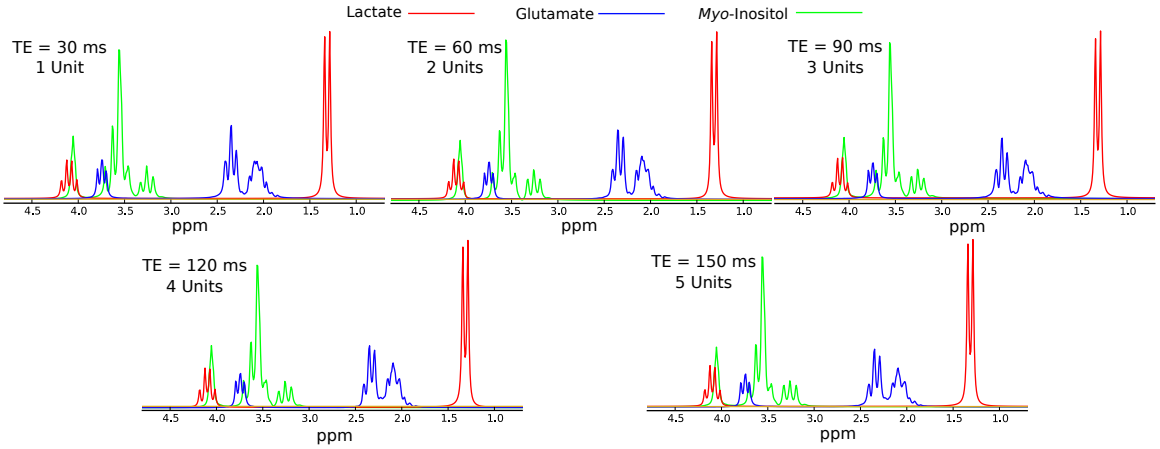


Figure 6.4: Simulations of PRESS-JR for 5 echo times and number of refocusing units. One refocusing unit every 30 ms of echo time is sufficient to refocus J-modulation.

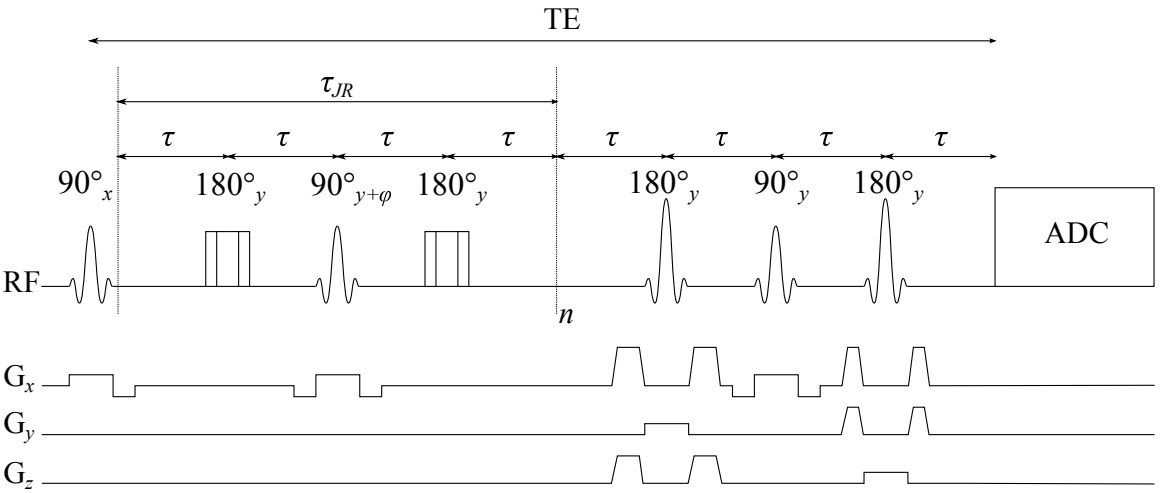


Figure 6.5: Pulse sequence diagram of PRESS-JR. The refocusing unit is performed n times as required. Each composite 180° pulse is surrounded by crusher gradients.

employing 1 PRESS-JR refocusing unit for every 30 ms of echo time as illustrated in Fig. 6.4. In this way one can refocus J-modulation for all relevant metabolites at arbitrary echo times.

6.3 Experiments

6.3.1 Pulse Sequence

A schematic for the implemented sequence is shown in Fig. 6.5. There are two problems that arise when employing many pulses for localized spectroscopy. The first is that the introduction of additional (90° and/or 180°) pulses can generate many unwanted coherences that arise from outside the voxel of interest or through different coherence pathways. The second problem is that any pulse imperfections from traditional 180° refocusing pulses can have cumulative effects, resulting in significantly decreased signal. In order to solve the first problem a combination of magnetic field gradient crushers and phase cycling was employed. The main unwanted coherence will be generated by the final two pulses (90°-180°) as they form a simple spin echo localized only along 2 dimensions. In order to remove this coherence, we used a 2-step phase cycle which alternated the phase of every J-refocusing 90° pulse by 180° (see Appendix for brief background on phase cycling). Removal of the rest of the unwanted coherences (stimulated, spin or spurious) was performed by phase cycling each of the final two 180° pulses in four 90° steps (with the ADC phased accordingly), adding crusher gradients surrounding each 180° pulse and using outer volume suppression (OVS). See Table 6.1 for the complete phase cycle. The crusher gradients were all 1 ms duration with amplitudes either 13 mT/m or 21 mT/m (as shown in Fig. 6.6). This orientation was chosen to minimize potential eddy current effects but still provide robust removal of unwanted signal. We found that if we used hard J-refocusing 90° pulses, we could not obtain adequate localization and unwanted coherence removal. Instead we opted to use slice selective symmetric 7-lobe sinc pulses with pre-winder and rewinder gradients (see Fig. 6.7 for comparison) [194]. The pre-winder gradients were necessary for the signal to be in phase at the center of the pulse and the rewinder gradients were used to produce a linear phase.

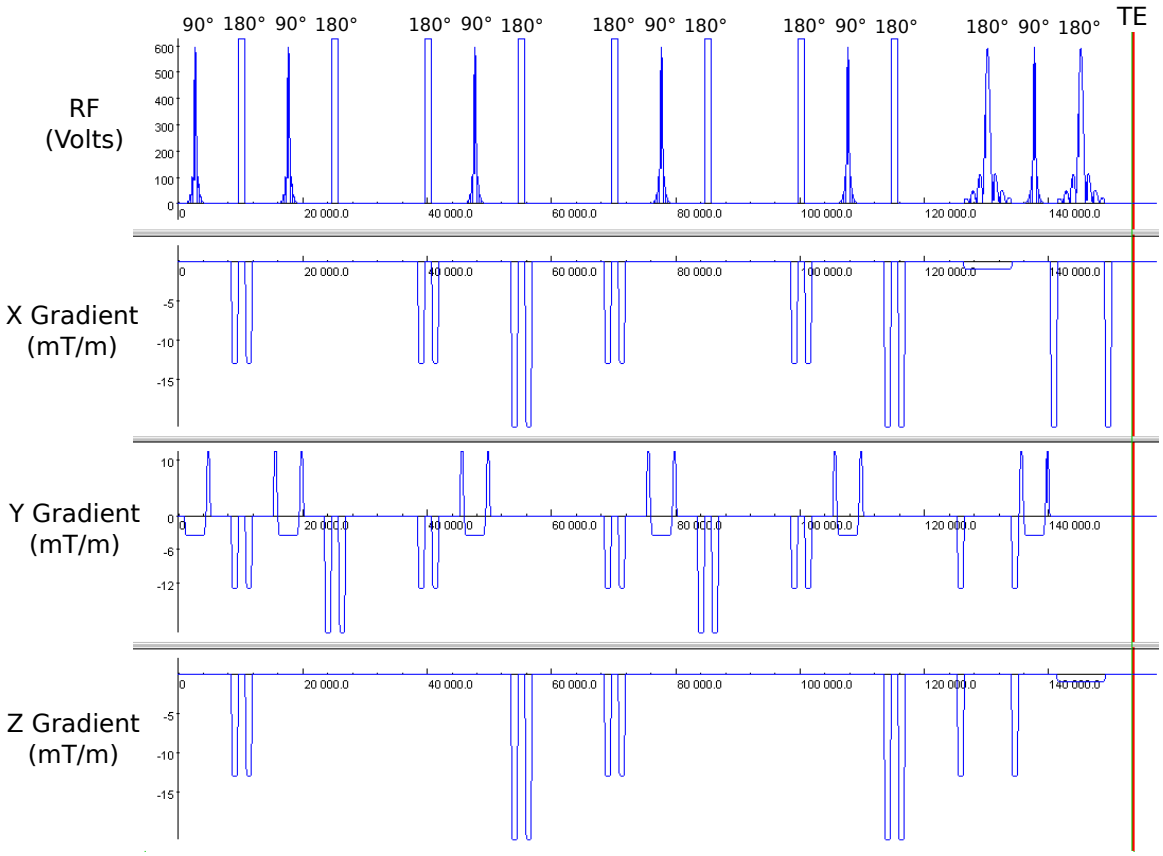


Figure 6.6: Gradient amplitudes and orientations for PRESS-JR.

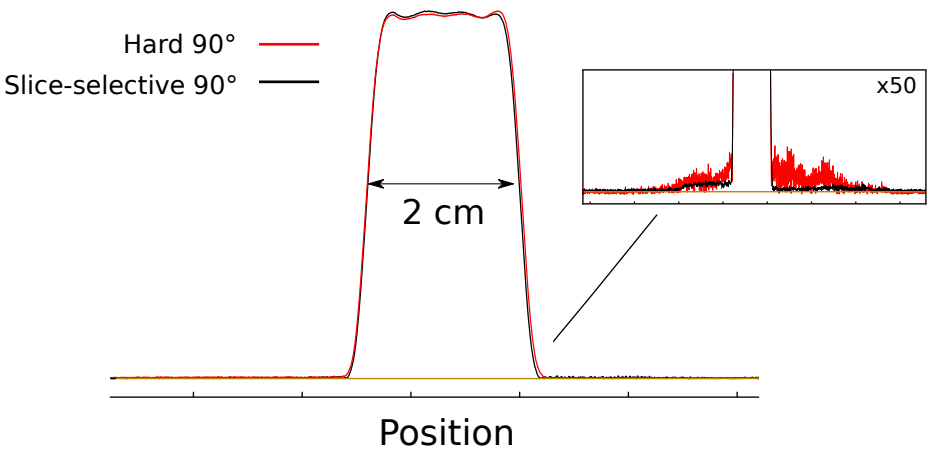


Figure 6.7: Acquired slice profiles for PRESS-JR with 3 refocusing units at TE = 90 ms using hard or slice-selective 90° J-refocusing pulses. # of averages = 4.

Step	Excit. 90°	Composite 180°	J-refocusing 90°	1st Slice 180°	2nd Slice 180°	ADC
1	0°	0°	90°	90°	90°	0°
2	0°	0°	270°	90°	90°	0°
3	0°	0°	90°	180°	90°	180°
4	0°	0°	270°	180°	90°	180°
5	180°	0°	90°	90°	90°	180°
6	180°	0°	270°	90°	90°	180°
7	180°	0°	90°	180°	90°	0°
8	180°	0°	270°	180°	90°	0°
9	0°	0°	90°	90°	180°	180°
10	0°	0°	270°	90°	180°	180°
11	0°	0°	90°	180°	180°	0°
12	0°	0°	270°	180°	180°	0°
13	180°	0°	90°	90°	180°	0°
14	180°	0°	270°	90°	180°	0°
15	180°	0°	90°	180°	180°	180°
16	180°	0°	270°	180°	180°	180°

Table 6.1: Phase cycle used to remove spurious echoes.

In order to reduce pulse imperfections and reduce specific absorption rate (SAR), all refocusing units (except the last one) employed global composite 180° refocusing pulses (hard $90_x - 180_y - 90_x$) instead of slice selective pulses [195]. These pulses had previously been used by Soher *et al.* for a localized implementation of CPMG entitled CP-PRESS [190]. In the presence of B_1 inhomogeneity these pulses are designed to produce a spin echo with full signal intensity (to first order approximation) but with a slight phase offset ϕ along the transverse plane. For conventional CPMG, the next pulse in the sequence is designed to remove the phase offset acquired from the first pulse resulting in a spin echo with full intensity and zero phase. For PRESS-JR, the reversal of J-modulation is based on the presence of signal that, except for the scalar coupling evolution, has zero phase and, as J-refocusing pulses appear after each odd 180° pulse, the phase of each J-refocusing pulse must therefore be offset by ϕ in order to maintain full signal intensity. ϕ must be determined empirically as the offset will depend on experimental conditions including voxel location and magnetic field homogeneity. To increase the robustness of this setup, the phase of

the composite pulses was also changed from unit to unit according to the MLEV-4 phase sequence [196, 197], *i.e.* pairs of composite pulses alternated between having positive ($90_x - 180_y - 90_x$) and negative phase ($90_{-x} - 180_{-y} - 90_{-x}$). The final two 180° were optimized 180° Mao refocusing pulses and required for localization [97].

6.3.2 Phantom Experimental

Phantom measurements were performed on a 3 T Siemens TRIO scanner (Siemens, Erlangen) using a 32-channel head-coil. A spherical phantom (GE Medical Systems, Milwaukee) was used containing 12.5 mM NAA, 10.0 mM Cr, 3.0 mM choline chloride (Cho), 12.5 mM glutamate (Glu), 7.5 mM *myo*-inositol (Ins), and 5.0 mM lactate (Lac). $20 \times 20 \times 20$ mm^3 voxels were placed in the centre of the phantoms and shimmed with FASTMAP [64]. Determining the correct phase offset for the J-refocusing pulses was accomplished by acquiring water-unsuppressed spectra and iterating the phase offset in order to find the offset that resulted in the maximum signal. Metabolite spectra were acquired with outer volume suppression and VAPOR water suppression (pulse bandwidth = 70 Hz) [27]. The duration of the sinc slice-selective excitation pulse and slice selective J-refocusing pulses was 2.5 ms with bandwidth 3.0 kHz, the duration of the Mao slice-selective 180° refocusing pulses was 6.3 ms with bandwidth 0.85 kHz and the duration of the composite pulses was 1.0 ms with bandwidth approximately 2.0 kHz. Water and metabolite spectra were acquired for PRESS, PRESS-JR and CPMG for a number of different echo-times (TE = 30, 60, 90, 120, 150 ms). For PRESS-JR and CPMG, 1 refocusing unit was used per 30 ms of echo time, *i.e.* for TE = 30 ms 1 refocusing unit was used, for TE = 60 ms 2 refocusing units were used, etc. 64 averages were acquired for each spectra with a repetition time of 3 s. To confirm accurate spatial localization, slice profiles for PRESS and PRESS-JR were also acquired using a water phantom by employing a linear gradient during acquisition of water-unsuppressed signal. Fig. 6.8 shows slice

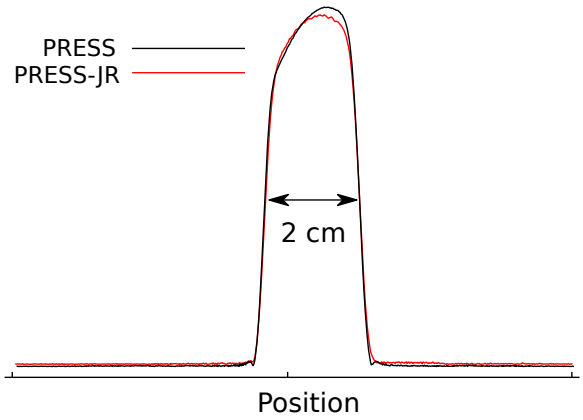


Figure 6.8: Slice profiles for PRESS and PRESS-JR with 3 refocusing units at TE = 90 ms. # of averages = 2; Bandwidth = 6000 Hz.

profiles in the excitation direction for PRESS and PRESS-JR (3 refocusing units), indicating a good agreement in slice profile.

LCModel [69] analysis was performed to ensure that phantom measurements matched the simulations and to determine metabolite T_2 relaxation times. The model spectra were generated based on previously reported chemical shifts and coupling constants [128, 129] using in-house MATLAB simulations with real refocusing pulses and incorporating the 4-compartment artifact [26]. LCModel analysis was performed on all spectra within the chemical shift range 0.5 to 4.2 ppm with line-broadening of 2.5 Hz to aid in fitting and to achieve a closer approximation to *in-vivo* conditions. Metabolite concentrations were obtained relative to creatine. Metabolite T_2 values were estimated based on the decay curves of the fitted LCModel integrals using a mono-exponential regression and the quality of fits was assessed with the coefficient of determination R^2. As performed previously [198], the multiplets (NAA-Aspartate) and singlet (NAA-Acetyl) of NAA, the $-CH_2$ and -CH_3 groups of Cr, and the multiplets and singlet of Cho were fitted separately. This is because the simulated spectra inaccurately assume that all proton groups have the same T_2 relaxation time.

	PRESS		PRESS-JR	
	T_2 (ms)	R^2	T_2 (ms)	R^2
NAA-Acetyl	470	0.95	625	0.91
NAA-Aspartate	166	0.88	128	0.91
Cr-CH_2	243	0.96	267	0.92
Cr-CH_3	276	0.98	368	0.98
Cho-$(CH_3)_3$	188	0.99	190	0.99
Cho-Multiplets	1265*	0.07*	258	0.97
Glu	189	0.98	214	0.94
Ins	258*	0.59*	313	0.91
Lac	105*	0.57*	260	0.94

Table 6.2: Phantom T_2s and corresponding coefficient of determination R^2 (p-value < 0.1 except for *). Cho-multiplets, Ins and Lac with PRESS result in inaccurate T_2 measurements due to J-modulation.

6.3.3 Phantom Results

Fig. 6.9 shows side-by-side plots for measured phantom spectra, LCModel fits, and the difference between the fit and measured data (residuals) for PRESS, PRESS-JR and CPMG for all TEs. Water full-width-half-maximum (FWHM) linewidths were 1.6 ± 0.1 Hz for PRESS, 1.6 ± 0.1 Hz for PRESS-JR and 1.7 ± 0.1 Hz for CPMG. SNR_{NAA} averaged over all TEs was 165 ± 41 for PRESS, 186 ± 36 for PRESS-JR and 191 ± 44 for CPMG. Fig. 6.10 shows the creatine referenced metabolite concentrations for PRESS and PRESS-JR at all TEs. Table 6.2 lists metabolite T_2s and corresponding R^2 (p-value < 0.1 except for marked conditions). As demonstrated in Fig. 6.11, all CRLBs were less than 10% except for Lac with PRESS at TE = 150 ms (CRLB = 17%).

6.3.4 *In-Vivo* Experimental

In-vivo measurements were also performed on a 3 T Siemens TRIO scanner (Siemens, Erlangen) using the same pulse sequence and experimental parameters as with the phantom measurements. 20 × 20 × 20 mm^3 voxels were positioned in the occipital lobe of 1 subject with acquisition parameters: TR = 3.0 s, sweep width = 3000 Hz, and

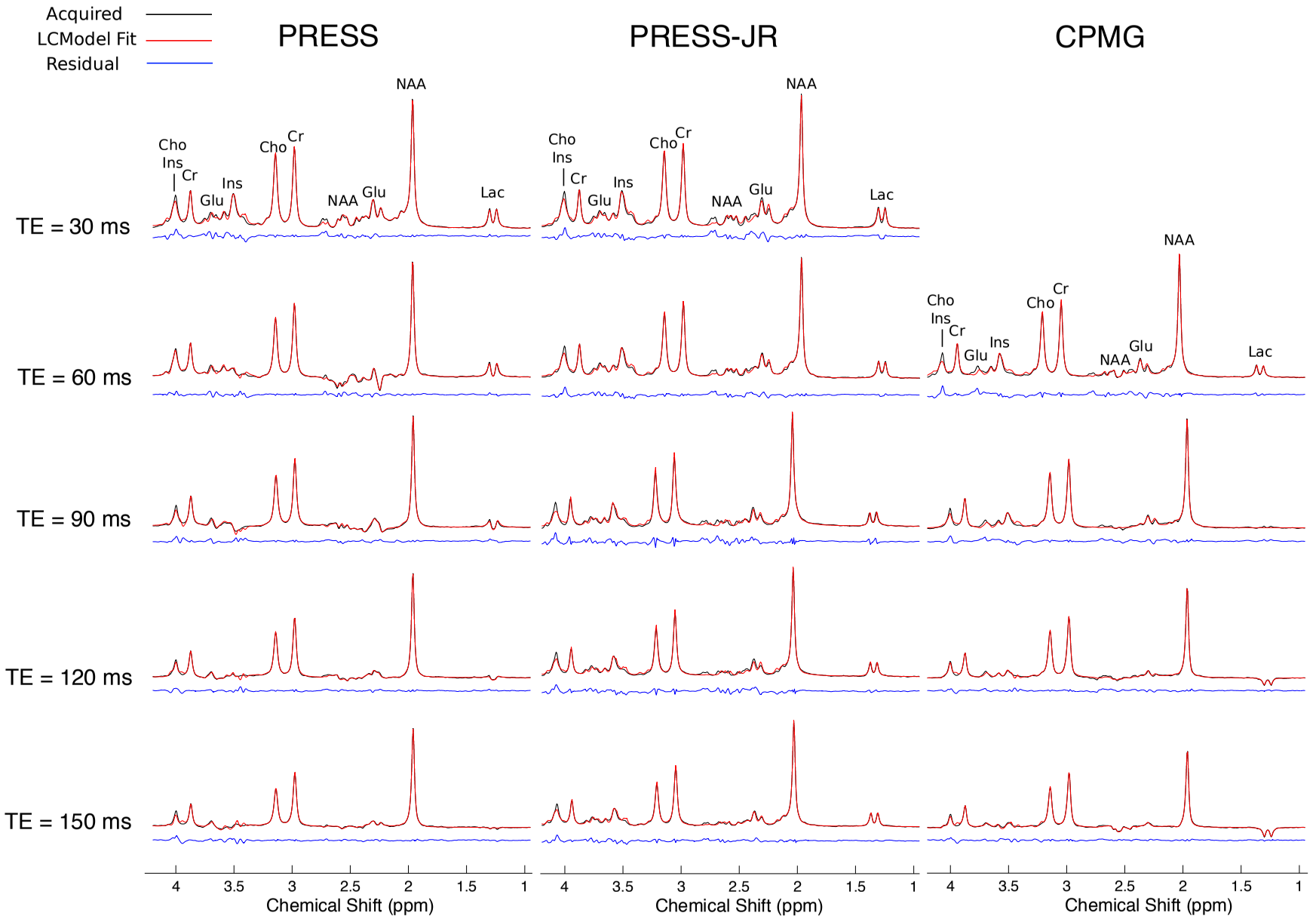


Figure 6.9: Experimental *in-vitro* spectra acquired with PRESS, PRESS-JR and CPMG at TE = 30, 60, 90, 120 and 150 ms, LCModel fits and residuals.

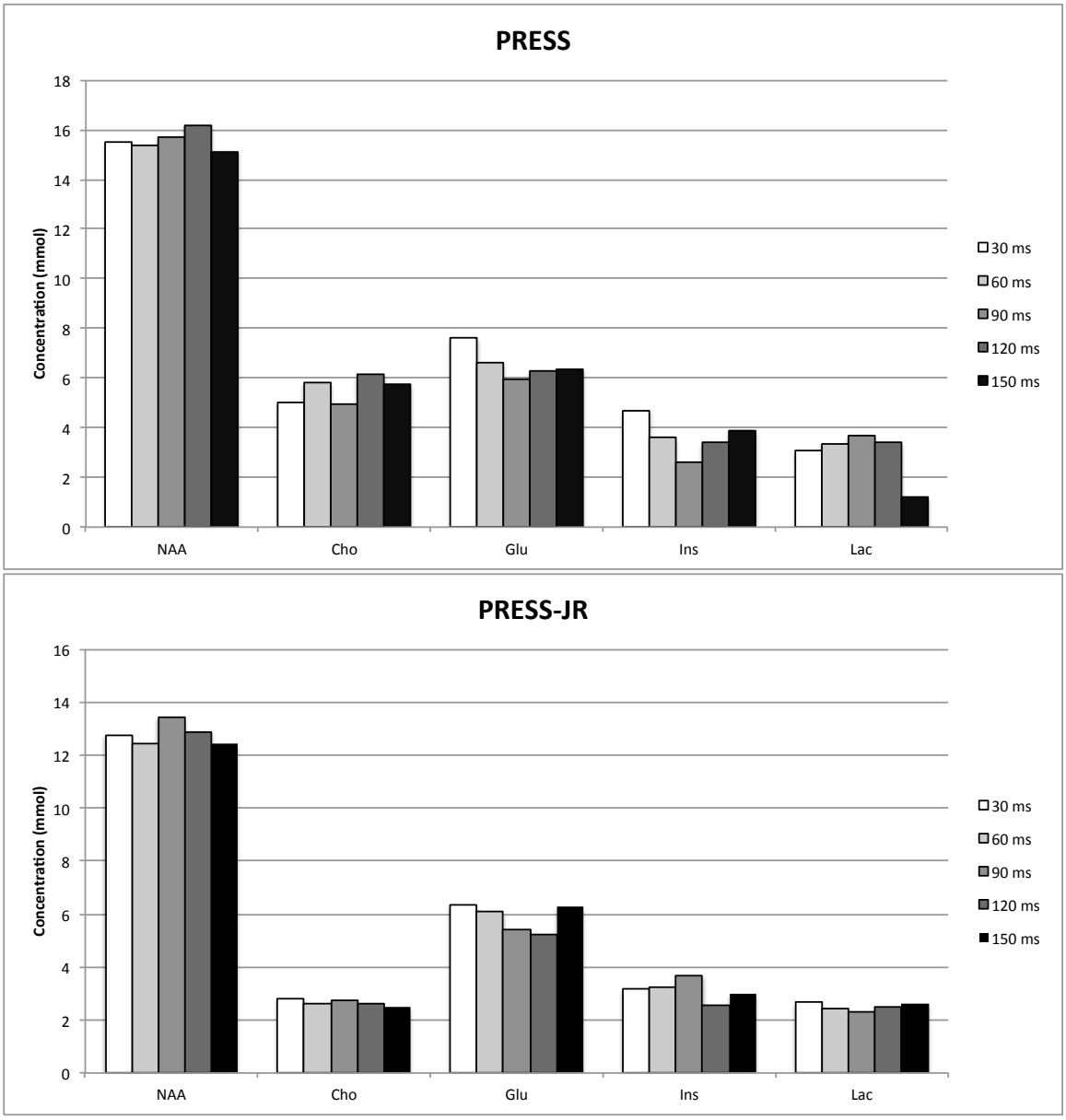


Figure 6.10: Creatine referenced metabolite concentrations (mmol) in phantom for all TEs of PRESS and PRESS-JR.

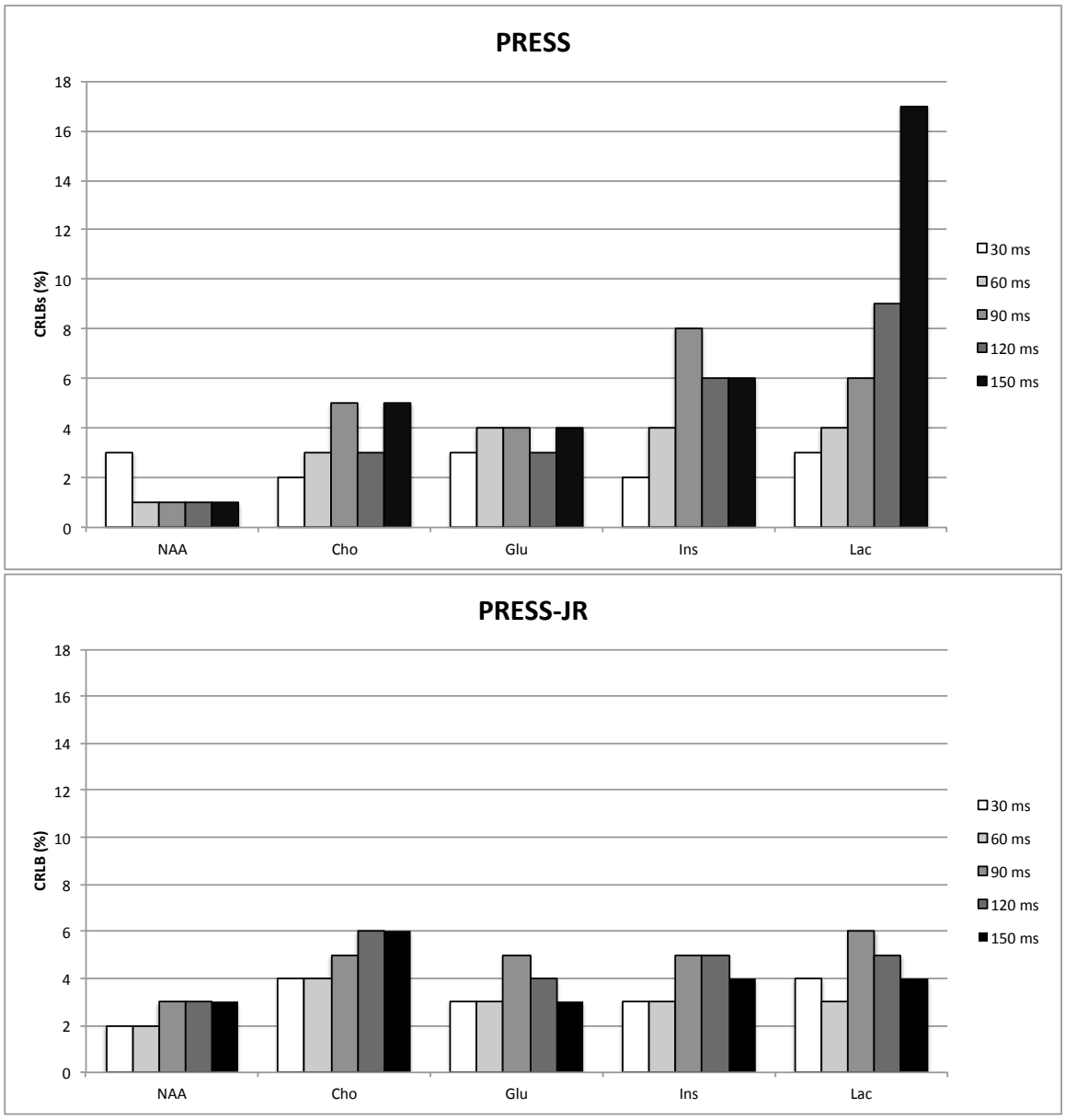


Figure 6.11: CRLBs (%) in phantom for all TEs of PRESS and PRESS-JR.

128 averages. Spectra were acquired for PRESS and PRESS-JR at TE = 30, and for PRESS, PRESS-JR and CPMG at TE = 150 ms. A water spectrum was also acquired for water reference. Metabolites were quantified with LCModel using a model spectra composed of alanine (Ala), aspartate (Asp), ascorbate/vitamin C (Asc), glycerophosphocholine (GPC), phosphocholine (PCho), total Cr, γ-aminobutyric acid (GABA), glutamine (Gln), Glu, glutathione (GSH), Ins, Lac, NAA, N-acetylaspartylglutamate (NAAG), phosphoethanolamine (PE), *scyllo*-inositol (*scyllo*-Ins) and taurine (Tau) generated in the same fashion as that of the phantom basis sets. The macromolecule baseline was simulated by LCModel and was comprised of an overall spline and individual macromolecule and lipid resonances at 0.9, 1.2, 1.3, 1.4, 1.7 and 2.0 ppm.

6.3.5 *In-Vivo* Results

Fig. 6.12 shows *in-vivo* spectra, LCModel fits, the difference between the fit and measured data and the fitted macromolecule baseline. Water FWHM linewidths were 7.2 ± 0.3 Hz for PRESS, 7.7 ± 0.4 Hz for PRESS-JR and 7.4 Hz for CPMG. SNR_{NAA} at TE = 30 ms was 101 for PRESS and 95 for PRESS-JR, at TE = 150 it was 68 for PRESS, 50 for PRESS-JR and 50 for CPMG. SNR_{Cr-CH3} at TE = 30 ms was 60 for PRESS and 63 for PRESS-JR and at TE = 150 ms it was 37 for PRESS, 41 for PRESS-JR and 37 for CPMG. Fig. 6.13 illustrates the LCModel concentrations referenced to creatine for PRESS and PRESS-JR (only metabolites that had CRLB $< 50\%$ in all measurement conditions are included). Table 6.3 shows the CRLBs for metabolites with CRLB $< 50\%$ in at least half the spectra.

6.4 Discussion

The first validation step was to confirm that the additional pulses associated with PRESS-JR do not result in unwanted coherences outside the VOI. As the slice pro-

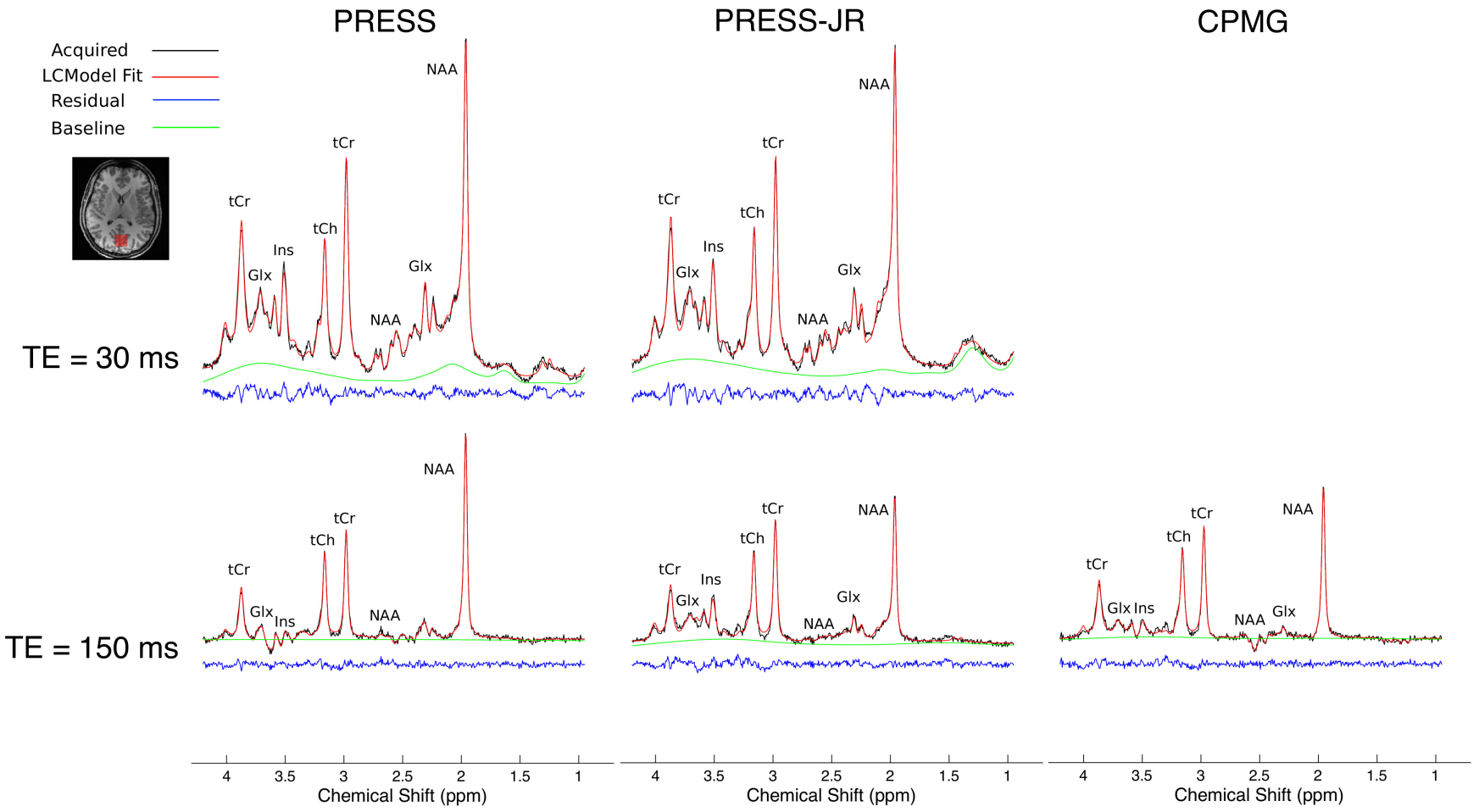


Figure 6.12: Acquired spectra taken from the occipital lobe in a normal subject with PRESS, PRESS-JR and CPMG for two TE values (30, 150 ms), LCModel fits, residuals and the LCModel fitted baseline.

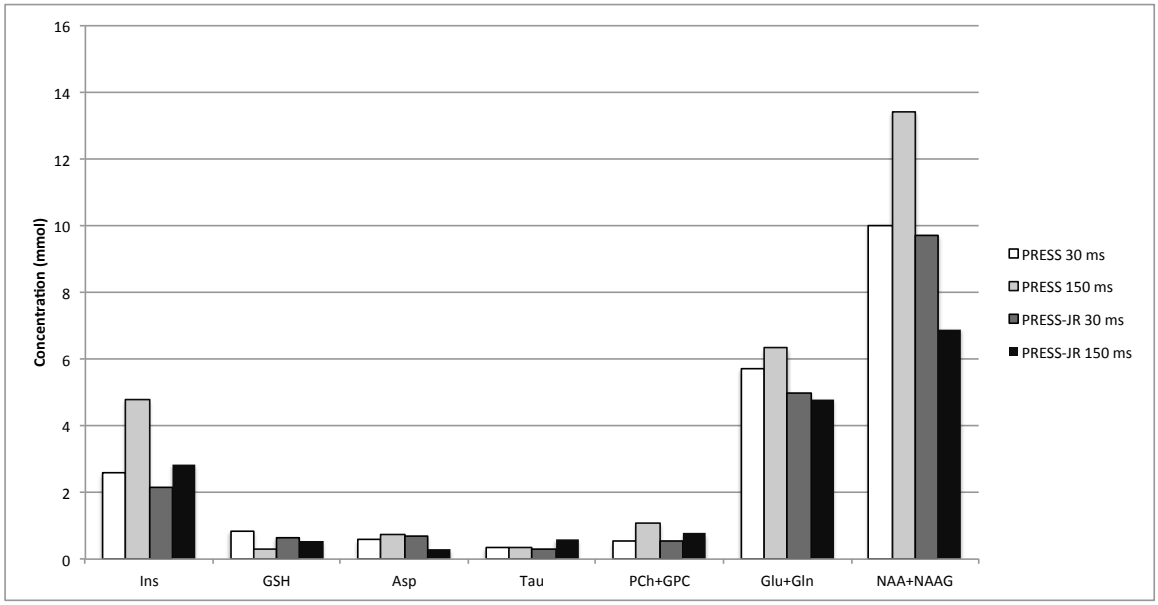


Figure 6.13: *In-vivo* metabolite concentrations (mmol) of PRESS and PRESS-JR.

	CRLB (%)			
	PRESS		PRESS-JR	
	30 ms	150 ms	30 ms	150 ms
NAA-Acetyl	2	2	2	2
NAA-Aspartate	13	6	12	7
Cr-CH_2	3	4	3	6
Cr-CH_3	2	2	2	2
Glu+Gln	4	6	4	4
Glu	4	8	4	5
Gln	20	26	12	25
Ins	3	6	3	4
GSH	7	23	9	14
GPC+PCho	3	9	4	21
PE	15	51*	12	37
Ala	999*	23	99*	22
Asp	18	23	14	38
NAAG	27	51*	16	106*
Tau	23	37	26	13

Table 6.3: Table of *in-vivo* metabolite CRLBs for PRESS and PRESS-JR at TE = 30 and 150 ms. Only those metabolites that can be quantified in 2 of the 4 spectra with CRLB $< 50\%$ were included. Asterisks refer to metabolites over CRLB $= 50\%$.

files show excellent localization, we can be confident that the combination of OVS and phase cycling sufficiently removed all unwanted coherences generated outside the VOI. The phantom linewidths and SNR were not significantly different (t-test, p-value > 0.1) between PRESS, PRESS-JR and CPMG though an SNR difference may be expected due to differences in the proportion of the echo time experiencing a pulse [199]. The simulated basis set provided a suitable fit for all phantom spectra thereby confirming the theory and simulations though the shape of NAA-Aspartate struggled to fit the group at 2.8 ppm for short-TE conditions in all pulse sequences. An experimentally acquired and calibrated basis set would correct this. In the phantom, PRESS-JR provided sufficient J-modulation suppression for all the coupled peaks (Glu, Ins, Lac, NAA-Aspartate and Cho-Multiplets) for all TEs resulting in the same effective spectral pattern for all metabolites at all TEs. Hence the difference between PRESS-JR spectra only arises due to T_2 interactions. CPMG provided J-modulation suppression up to TE = 60 ms, but at longer echo times all the coupled spins have undergone significant modulation. A comparison between the PRESS and PRESS-JR creatine-referenced metabolite concentration reveals a number of differences. NAA and Cho are consistently lower with PRESS-JR and Lac is severely underestimated with PRESS at TE = 150 ms. The NAA and Cho differences are best explained by the underestimation of the LCModel fit to the NAA multiplet at 2.8 ppm and Cho-multiplets at 4.0 ppm with PRESS-JR. The underestimation of Lac with PRESS at TE = 150 ms is due to the lack of overall signal. This may be predicted from the literature as, depending on sequence parameters, additional anomalous J-modulation can result in almost complete reduction in Lac doublet signal at approximately TE = 150 ms [200]. Mono-exponential fits provided robust T_2 measurements for all metabolites with PRESS-JR ($R^2 > 0.9$, p-value < 0.1) but not for Cho-Multiplets, Lac and Ins with PRESS ($R^2 < 0.9$, p-value > 0.1). This is expected as, at longer TEs, LCModel may fit the data with acceptable CRLBs but, due to J-modulation associated signal

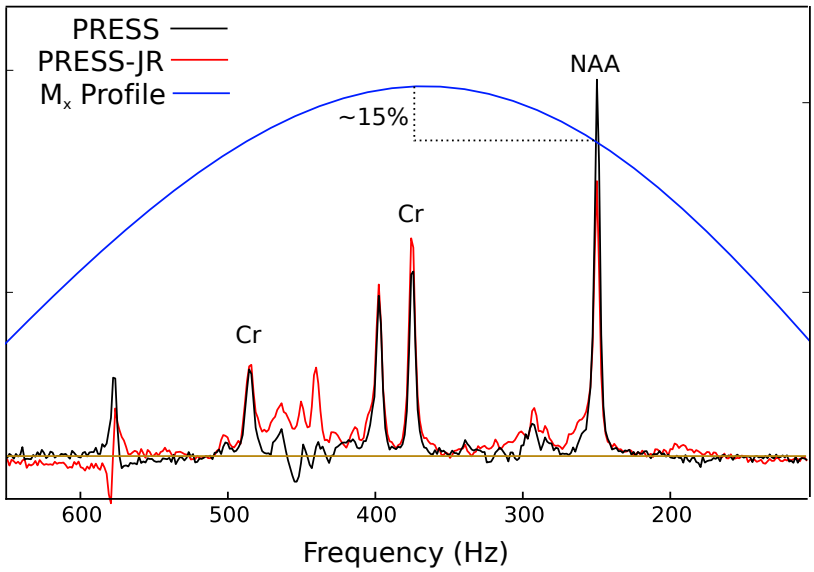


Figure 6.14: Frequency profile of a 180° composite refocusing pulse overlaid with PRESS and PRESS-JR spectra at TE = 150 ms. The frequency dependent phase difference results in signal loss of approximately 15% between $Cr - CH_3$ and NAA.

loss, may provide inaccurate metabolite concentrations. For all metabolites in which accurate T_2 measurements could be determined, PRESS-JR had longer T_2 measurements. This has been shown *in-vivo* in rat and human brain for CPMG variations and is caused by a reduction in effective dephasing with CPMG compared with a single spin-echo [201, 190].

The *in-vivo* spectra had similar linewidths and SNR_{Cr-CH3} for all sequences at each TE though SNR_{NAA} was higher with PRESS than with PRESS-JR and CPMG at TE = 150 ms - suggesting that the CPMG or PRESS-JR pulse train affects the NAA peak more than Cr. This is unexpected as previous metabolite T_2 studies have shown that a pulse train should affect all the singlets approximately equally [202]. This can perhaps be explained by the frequency dependent phase generated by each 180° composite refocusing pulse. Bloch simulations show a phase difference of approximately 15% between the carrier frequency (3.0 ppm / $Cr - CH_3$ peak) and the NAA peak (see Fig. 6.14). An improved pulse design may reduce this effect.

Similar to the phantom measurements, simulated basis sets were found to ac-

curately fit the *in-vivo* spectra - though, once again, this could be improved with an experimentally acquired basis set. At TE = 150 ms, PRESS-JR suppressed J-modulation resulting in fully upright peaks for all metabolites. In particular, Glx and Ins, which are metabolites of interest in many clinical research studies, have improved SNR and simplified resonance patterns compared with PRESS and CPMG. The metabolite concentrations for PRESS and PRESS-JR were similar except for NAA+NAAG which had a marked decrease for PRESS-JR at TE = 150 ms. In parallel to the $\mathrm{SNR_{NAA}}$ comment, this is likely due to either subject motion, remaining pulse imperfections or the composite 180° refocusing pulse slice profile. Though the CRLBs at TE = 150 ms were larger for all metabolites (except for Ala, NAA-Aspartate and Tau) when compared with TE = 30 ms, at TE = 150 ms there is minimal macromolecule contamination and therefore less potential to bias results. Hence a higher (but still acceptable CRLB) may not inherently suggest that short-TE PRESS offers increased precision over a long-TE PRESS-JR. Further studies exploring the potential for increased precision of coupled metabolites must be performed. One of the concerns with wide bandwidth 180° pulse trains is that the amount of energy deposited quickly approaches safety limits. As simulations and our experimental measurements suggest that PRESS-JR provides sufficient J-modulation suppression with significantly less refocusing units when compared with CPMG, we are not SAR-limited but rather limited by the number of pulses and gradients we can fit within a given TE. Though PRESS-JR shows potential for both straightforward T_2-weighted spectroscopy and, at long TE, decreased quantification variability caused by erroneous baseline estimation, further studies involving more subjects are required.

Future improvements of PRESS-JR could involve implementing the sequence at higher field strengths ($\geq$ 7 T). As it is more difficult to accurately model the baseline of short-TE spectra at higher field strengths [59], long-TE PRESS-JR may be a good alternative. However, extending PRESS-JR to higher field strengths would require

replacement of all the refocusing pulses as, at these field strengths, the chemical shift displacement artifact would be too severe. Replacing hard composite pulses with adiabatic pulses [202] and conventional 180° pulses with pairs of adiabatic pulses would effectively solve this issue - though SAR limits will be a problem. A previous study has employed a single perfect echo to generate high-quality MRSI spectra at 7 T for TE = 34 ms [203]. As macromolecule signals relax faster at 7 T, 2 or 3 refocusing units may be adequate for baseline clear spectra. Another potential extension of PRESS-JR is to include phase-encoding gradients and convert the sequence to MRSI (similar to [203]) . In short-TE MRSI studies, intense lipid signals from the scalp may bleed into adjacent brain voxels obscuring important metabolic information [204]. PRESS-JR may offer a solution to this problem by acquiring long-TE spectra and thereby avoiding the contamination altogether.

Chapter 7

Conclusion

In-vivo spectroscopy provides vital insight into neurochemical environments. Due to the relatively low concentrations of the metabolites of interest, however, technical challenges must be overcome in order to acquire high quality spectra and precise metabolite concentrations. This thesis tackled some of these technical challenges and demonstrated a novel acquisition scheme for acquiring spectra from multiple locations concurrently at 7 T. Using this scheme, we have shed new insight into neurochemical time-courses following tDCS. This thesis also outlined a novel pulse sequence that can effectively suppress J-modulation.

Future improvements on the two-voxel acquisition scheme include extension of the sequence to acquire spectra from more voxels or to have dynamic higher-order shimming. Dynamic higher-order shimming would unlock any shimming constraints on the scheme - though B_1^+ requirements still remain. A recent extension to the 2-voxel acquisition scheme outlined in this thesis is to include parallel reconstruction so as to acquire the spectra from both voxels in one TR (thereby decreasing the acquisition time by a theoretical 50%) [205]. One downside to this approach is that it results in an increased chemical shift displacement artifact and a noise increase. Therefore if one requires the highest possible precision for a particular experiment,

the technique outlined in this thesis is still the better choice.

PRESS-JR has a number of potential avenues for future developments. One potential investigation is a full validation of *in-vivo* T_2 measurements. T_2 measurements are extremely useful as they can provide additional information over concentration measurements. A given metabolite concentration does not provide any insight regarding the local cellular environment but T_2 measurements can potentially probe cellular dynamics [206] and microstructure [207]. As PRESS-JR provides fully-upright peaks across the spectral range of interest, determining accurate T_2 values for coupled metabolites may be straightforward. Acquiring PRESS-JR spectra takes the same scan time as conventional single-voxel-spectroscopy for a given voxel location and SNR and therefore one could potentially acquire a suitable number of TEs within a single scan to probe compartmental dynamics by fitting a multi-exponential to the T_2 decay [208]. If this is possible, this opens up a number of potential studies examining coupled metabolite T_2s that would otherwise be difficult or unfeasible with CPMG including probing bipolar disorder and schizophrenia at the cellular level [209].

Another avenue for PRESS-JR is to examine tumor spectra at long-TE. Fig. 7.1 illustrates the impact that lipids and macromolecules can have on cancer spectra. Due to the tumor baseline signals, one generally must employ long TE spectroscopy to accurately quantify most metabolites but, due to J-modulation, at long TE only a few coupled metabolites remain. As the presence (or absence) of certain coupled metabolites has been shown to effect prognosis [210], there is the potential that PRESS-JR can help in cancer diagnostics and treatment planning.

A natural extension of PRESS-JR is to implement the sequence at 7 T. This could provide even greater reduction in baseline-associated errors as baseline signals become harder to tell apart from metabolite signals as the magnetic field strength is increased (see Chapter 3). Higher magnetic field strength would also increase the number of metabolite T_2s that could be determined (*i.e.* Glx would be separated

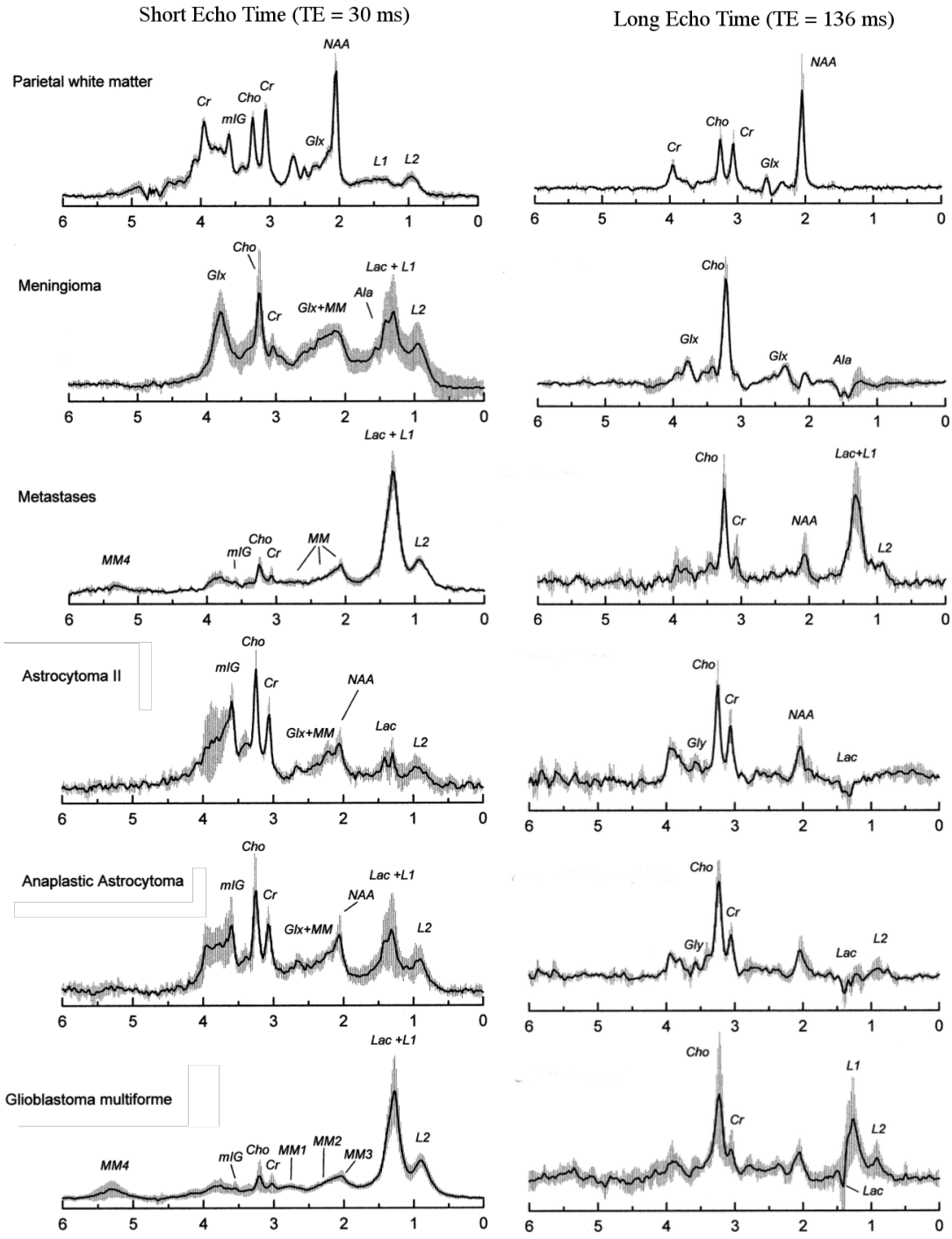


Figure 7.1: Mean and SD of normalized short and long TE spectra from healthy white matter and a variety of tumor classes. Adapted from [182].

into Glu and Gln). Implementation would require redesign of the 180° pulses as the pulse bandwidth of the composite and slice selective 180° refocusing pulses used in this thesis would not be adequate at 7 T. The obvious alternative would be to use adiabatic pulses (as with semi-LASER) and take advantage of their wide bandwidth and resilience to magnetic field inhomogeneities. This could also be thought of as introducing J-refocusing 90° pulses into CP-LASER and therefore calling the technique LASER-JR may be more appropriate [201]. The main challenge with this approach is keeping the SAR within safety limits. As the SAR is already a problem with semi-LASER (4 adiabatic pulses), one would need to improve B_1^+ efficiency using parallel transmit or increase the TR in order to use 2 or more refocusing units. As T_2s are shorter at 7 T, one could acquire spectra at shorter TEs and therefore use fewer refocusing units in order to acquire long-TE spectra without J-modulation or baseline contamination. This approach could also be easily combined with the 2-voxel acquisition scheme outlined in this thesis to provide multiple long-TE, J-refocused spectra concurrently. An alternative approach in extending PRESS-JR to 7 T is to use an additional crusher coil for outer volume suppression [112] and broadband hard 180° pulses as implemented previously [203]. In that study, Pan *et al.* used one refocusing unit and phase encoding to generate fully J-refocused MRSI at TE = 34 ms. Extending their approach with multiple refocusing units and longer TEs should be rather straightforward and has the advantage of significantly reduced SAR when compared with the adiabatic approach but would require a specialized crusher coil.

An extension of both T_2 and cancer related experiments would be to incorporate phase encoding in order to acquire spectra from many regions at once. Assuming an acquisition duration of approximately 15 minutes per TE, one may be able to acquire a sufficient number of TEs for whole-brain T_2 measurements in a typical scan slot of 1 hour. Alternatively, one could reduce lipid bleeding effects associated with short-TE MRSI in tumors by acquiring long TE PRESS-JR spectra and accurately map

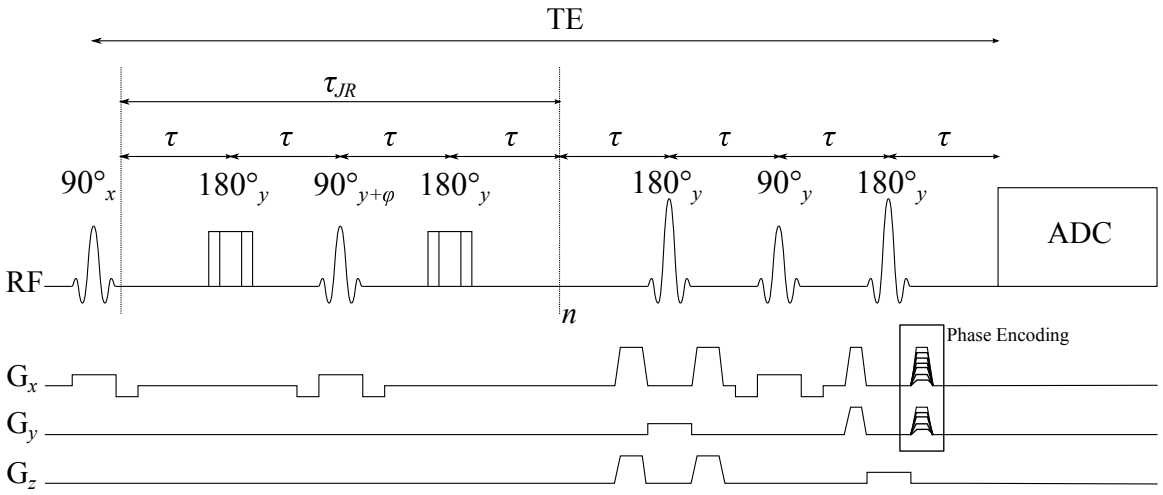


Figure 7.2: Pulse sequence diagram of PRESS-JR with phase encoding for MRSI acquisition.

distributions of coupled metabolites throughout the tumor and surrounding region. An illustration of how this might be implemented is shown in Fig. 7.2.

References

[1] I. I. Rabi, *Physical Review*, 1937, **51**, 652–654.

[2] E. M. Purcell, H. C. Torrey, R. V. Pound, *Physical Review*, 1946, **69**, 37–38.

[3] F. Bloch, *Physical Review*, 1946, **70**, 460–474.

[4] W. G. Proctor, F. C. Yu, *Physical Review*, 1950, **77**, 717–717.

[5] W. C. Dickinson, *Physical Review*, 1950, **77**, 736–737.

[6] R. Damadian, *Science*, 1971, **171**, 1151–1153.

[7] P. C. Lauterbur, *Nature*, 1973, **242**, 190–191.

[8] P. Mansfield, P. K. Grannell, *Journal of Physics C: Solid State Physics*, 1973, **6**, L422.

[9] R. A. de Graaf, *In Vivo NMR Spectroscopy: Principles and Techniques 1st ed.*, Wiley, 1999.

[10] M. H. Levitt, *Spin Dynamics: Basics of Nuclear Magnetic Resonance 2nd ed.*, Wiley-Blackwell, 2008.

[11] R. A. Webb, *Review of Scientific Instruments*, 1977, **48**, 1585–1594.

[12] S. Gross, C. Barmet, B. Dietrich, K. Prussmann in *Proceedings of the 20th Annual Meeting ISMRM*, Melbourne, Australia, p. 378.

[13] N. Bloembergen, E. M. Purcell, R. V. Pound, *Physical Review*, 1948, **73**, 679–712.

[14] W. A. Anderson, R. Freeman, *The Journal of Chemical Physics*, 1962, **37**, 85–103.

[15] T. R. Carver, C. P. Slichter, *Physical Review*, 1953, **92**, 212–213.

[16] N. F. Ramsey, E. M. Purcell, *Physical Review*, 1952, **85**, 143–144.

[17] H. J. Bernstein, J. A. Pople, W. G. Schneider, *Canadian Journal of Chemistry*, 1957, **35**, 67–83.

[18] E. L. Hahn, *Physical Review*, 1950, **80**, 580–594.

[19] T. C. Farrar, J. E. Harriman, *Density matrix theory and its applications in NMR spectroscopy: an introduction to the theory and applications 2nd ed.*, Farragut Press, Madison, Wisconsin, 1995.

[20] J. A. Aguilar, M. Nilsson, G. Bodenhausen, G. A. Morris, *Chemical Communications*, 2012, **48**, 811.

[21] D. G. Norris, J. M. S. Hutchison, *Magnetic Resonance Imaging*, 1990, **8**, 33–37.

[22] M. A. Bernstein, X. J. Zhou, J. A. Polzin, K. F. King, A. Ganin, N. J. Pelc, G. H. Glover, *Magnetic Resonance in Medicine*, 1998, **39**, 300–308.

[23] H. Nyquist, *Trans. AIEE*, 1928, **47**, 617–644.

[24] C. Shannon, *Proc. Institute of Radio Engineers*, 1949, **37**, 10–21.

[25] P. A. Bottomley, *Annals of the New York Academy of Sciences*, 1987, **508**, 333–348.

[26] L. G. Kaiser, K. Young, G. B. Matson, *Journal of Magnetic Resonance*, 2008, **195**, 67–75.

[27] I. Tkáč, Z. Starčuk, I.-Y. Choi, R. Gruetter, *Magnetic Resonance in Medicine*, 1999, **41**, 649–656.

[28] K.-D. Merboldt, D. Hörstermann, W. Hänicke, H. Bruhn, J. Frahm, *Magnetic Resonance in Medicine*, 1993, **29**, 125–129.

[29] G. Öz, I. Tkáč, *Magnetic Resonance in Medicine*, 2011, **65**, 901–910.

[30] M. Garwood, L. DelaBarre, *Journal of Magnetic Resonance*, 2001, **153**, 155–177.

[31] M. S. Silver, R. I. Joseph, D. I. Hoult, *Physical Review A*, 1985, **31**, 2753–2755.

[32] M. Piotto, V. Saudek, V. Sklenár, *Journal of Biomolecular NMR*, 1992, **2**, 661–665.

[33] S. L. Patt, B. D. Sykes, *The Journal of Chemical Physics*, 1972, **56**, 3182–3184.

[34] E. D. Becker, J. A. Feretti, T. C. Farrar, *Journal of the American Chemical Society*, 1969, **91**, 7784–7785.

[35] A. Haase, J. Frahm, W. Hanicke, D. Matthaei, *Physics in Medicine and Biology*, 1985, **30**, 341.

[36] D. J. Rigotti, M. Inglese, J. S. Babb, M. Rovaris, B. Benedetti, M. Filippi, R. I. Grossman, O. Gonen, *American Journal of Neuroradiology*, 2007, **28**, 1650–1651.

[37] J. R. Moffett, A. M. A. Namboodiri in *N-Acetylaspartate*, of *Advances in Experimental Medicine and Biology*, J. R. Moffett, S. B. Tieman, D. R. Weinberger, J. T. Coyle, A. M. A. Namboodiri (Eds.), Springer US, 2006, pp. 7–26.

[38] S. Brugger, J. M. Davis, S. Leucht, J. M. Stone, *Biological Psychiatry*, 2011, **69**, 495–503.

[39] S. Signoretti, R. Vagnozzi, B. Tavazzi, G. Lazzarino, *Neurosurgical Focus*, 2010, **29**, E1.

[40] J. M. Wardlaw, I. Marshall, J. Wild, M. S. Dennis, J. Cannon, S. C. Lewis, *Stroke*, 1998, **29**, 1618–1624.

[41] I. Savic, A. Lekvall, D. Greitz, G. Helms, *Epilepsia*, 2000, **41**, 290–296.

[42] P. A. Narayana, *Journal of Neuroimaging*, 2005, **15**, 46S–57S.

[43] L. A. Passani, J. P. Vonsattel, R. E. Carter, J. T. Coyle, *Molecular and Chemical Neuropathology*, 1997, **31**, 97–118.

[44] H. J. Wittsack, H. Kugel, B. Roth, W. Heindel, *Journal of Magnetic Resonance Imaging*, 1996, **6**, 889–893.

[45] P. Arun, C. N. Madhavarao, J. R. Moffett, M. A. A. Namboodiri, *Journal of Neurochemistry*, 2006, **98**, 2034–2042.

[46] J. R. Moffett, B. Ross, P. Arun, C. N. Madhavarao, A. M. A. Namboodiri, *Progress in Neurobiology*, 2007, **81**, 89–131.

[47] D. E. Saunders, F. A. Howe, A. van den Boogaart, J. R. Griffiths, M. M. Brown, *Journal of Magnetic Resonance Imaging*, 1999, **9**, 711–716.

[48] N. De Stefano, P. M. Matthews, J. P. Antel, M. Preul, G. Francis, D. L. Arnold, *Annals of Neurology*, 1995, **38**, 901–909.

[49] B. S. Y. Li, H. Wang, O. Gonen, *Magnetic Resonance Imaging*, 2003, **21**, 923–928.

[50] M. Erecińska, I. A. Silver, *Progress in Neurobiology*, 1990, **35**, 245–296.

[51] L. Hertz, *Neurochemistry International*, 2004, **45**, 285–296.

[52] N. Sibson, G. Mason, J. Shen, G. Cline, A. Zara Herskovits, J. Wall, K. Behar, D. Rothman, R. Shulman, *Journal of Neurochemistry*, 2001, **76**, 975–989.

[53] M. Mescher, H. Merkle, J. Kirsch, M. Garwood, R. Gruetter, *NMR in Biomedicine*, 1998, **11**, 266–272.

[54] G. Oz, M. Terpstra, I. Tkác, P. Aia, J. Lowary, P. J. Tuite, R. Gruetter, *Magnetic Resonance in Medicine*, 2006, **55**, 296–301.

[55] A. Floyer-Lea, M. Wylezinska, T. Kincses, P. M. Matthews, *Journal of Neurophysiology*, 2006, **95**, 1639–1644.

[56] O. A. Petroff, K. L. Behar, R. H. Mattson, D. L. Rothman, *Journal of Neurochemistry*, 1996, **67**, 2399–2404.

[57] G. Sanacora, G. F. Mason, D. L. Rothman, K. L. Behar, F. Hyder, O. A. Petroff, R. M. Berman, D. S. Charney, J. H. Krystal, *Archives of General Psychiatry*, 1999, **56**, 1043–1047.

[58] K. L. Behar, D. L. Rothman, D. D. Spencer, O. A. Petroff, *Magnetic Resonance in Medicine*, 1994, **32**, 294–302.

[59] C. Cudalbu, V. Mlynárik, R. Gruetter, *Journal of Alzheimer's Disease*, 2012, **31**, S101–115.

[60] R. Kreis, J. Slotboom, L. Hofmann, C. Boesch, *Magnetic Resonance in Medicine*, 2005, **54**, 761–768.

[61] R. L. Vold, J. S. Waugh, M. P. Klein, D. E. Phelps, *The Journal of Chemical Physics*, 1968, **48**, 3831–3832.

[62] F. Roméo, D. I. Hoult, *Magnetic Resonance in Medicine*, 1984, **1**, 44–65.

[63] S. Shah, P. Kellman, A. Greiser, P. Weale, S. Zuehlsdorff, R. Jerecic in *Proceedings of the 17th Annual Meeting ISMRM*, Honolulu, Hawaii, USA, p. 565.

[64] R. Gruetter, I. Tkáč, *Magnetic Resonance in Medicine*, 2000, **43**, 319–323.

[65] U. Klose, *Magnetic Resonance in Medicine*, 1990, **14**, 26–30.

[66] E. Cabanes, S. Confort-Gouny, Y. Le Fur, G. Simond, P. J. Cozzone, *Journal of Magnetic Resonance*, 2001, **150**, 116–125.

[67] A. Naressi, C. Couturier, I. Castang, R. de Beer, D. Graveron-Demilly, *Computers in Biology and Medicine*, 2001, **31**, 269–286.

[68] Vanhamme, van den Boogaart A, V. H. S, *Journal of Magnetic Resonance*, 1997, **129**, 35–43.

[69] S. W. Provencher, *NMR in Biomedicine*, 2001, **14**, 260–264.

[70] B. Soher, P. Semanchuk, D. Todd, J. Steinberg, K. Young in *Proceedings of the 19th Annual Conference ISMRM*, Quebec, Canada, p. 1410.

[71] Cavassila, Deval, Huegen, van Ormondt D, Graveron-Demilly, *Journal of Magnetic Resonance*, 2000, **143**, 311–320.

[72] J. F. A. Jansen, W. H. Backes, K. Nicolay, M. E. Kooi, *Radiology*, 2006, **240**, 318–332.

[73] R. Kreis, T. Ernst, B. D. Ross, *Journal of Magnetic Resonance, Series B*, 1993, **102**, 9–19.

[74] R. A. de Graaf, P. B. Brown, S. McIntyre, T. W. Nixon, K. L. Behar, D. L. Rothman, *Magnetic Resonance in Medicine*, 2006, **56**, 386–394.

[75] F. Träber, W. Block, R. Lamerichs, J. Gieseke, H. H. Schild, *Journal of Magnetic Resonance Imaging*, 2004, **19**, 537–545.

[76] I. I. Kirov, L. Fleysher, R. Fleysher, V. Patil, S. Liu, O. Gonen, *Magnetic Resonance in Medicine*, 2008, **60**, 790–795.

[77] D. Öngür, A. P. Prescot, J. E. Jensen, E. D. Rouse, B. M. Cohen, P. F. Renshaw, D. P. Olson, *Magnetic Resonance in Medicine*, 2010, **63**, 1–8.

[78] P. Pugnat, R. Barbier, C. Berriaud, R. Berthier, F. Debray, P. Fazilleau, B. Hervieu, P. Manil, M. Massinger, c. pes, R. Pfister, M. Pissard, L. Ronayette, C. Trophime, *IEEE Transactions on Applied Superconductivity*, 2014, **24**, 1–5.

[79] R. Fu, W. W. Brey, K. Shetty, P. Gor'kov, S. Saha, J. R. Long, S. C. Grant, E. Y. Chekmenev, J. Hu, Z. Gan, M. Sharma, F. Zhang, T. M. Logan, R. Brüschweller, A. Edison, A. Blue, I. R. Dixon, W. D. Markiewicz, T. A. Cross, *Journal of Magnetic Resonance*, 2005, **177**, 1–8.

[80] C. Qian, I. S. Masad, J. T. Rosenberg, M. Elumalai, W. W. Brey, S. C. Grant, P. L. Gor'kov, *Journal of Magnetic Resonance*, 2012, **221**, 110–116.

[81] P. Vedrine, G. Aubert, J. Belorgey, C. Berriaud, A. Bourquard, P. Bredy, A. Donati, O. Dubois, F. Elefant, g. Gilgrass, F. Juster, H. Lannou, F. Molinie, M. Nusbaum, F. Nunio, A. Payn, L. Quettier, T. Schild, L. Scola, A. Sinanna, *IEEE Transactions on Applied Superconductivity*, 2014, **24**, 1–6.

[82] B. R. Plantinga, Y. Temel, A. Roebroeck, K. Uludağ, D. Ivanov, M. L. Kuijf, B. M. ter Haar Romenij, *Frontiers in Human Neuroscience*, 2014, **8**, 876.

[83] R. Mekle, V. Mlynárik, G. Gambarota, M. Hergt, G. Krueger, R. Gruetter, *Magnetic Resonance in Medicine*, 2009, **61**, 1279–1285.

[84] J. T. Vaughan, M. Garwood, C. M. Collins, W. Liu, L. DelaBarre, G. Adriany, P. Andersen, H. Merkle, R. Goebel, M. B. Smith, K. Ugurbil, *Magnetic Resonance in Medicine*, 2001, **46**, 24–30.

[85] K. R. Foster, H. P. Schwan, *Critical Reviews in Biomedical Engineering*, 1989, **17**, 25–104.

[86] IEC, *International standard, medical equipment – part 2: particular requirements for the safety of magnetic resonance equipment for medical diagnosis 3rd ed.*, Geneva, International Electrotechnical Commission, 2002.

[87] P. A. Bottomley, R. W. Redington, W. A. Edelstein, J. F. Schenck, *Magnetic Resonance in Medicine*, 1985, **2**, 336–349.

[88] Z. Wang, J. C. Lin, W. Mao, W. Liu, M. B. Smith, C. M. Collins, *Journal of Magnetic Resonance Imaging*, 2007, **26**, 437–441.

[89] C. M. Collins, W. Liu, J. Wang, R. Gruetter, J. T. Vaughan, K. Ugurbil, M. B. Smith, *Journal of Magnetic Resonance Imaging*, 2004, **19**, 650–656.

[90] K. Caputa, M. Okoniewski, M. Stuchly, *IEEE Antennas and Propagation Magazine*, 1999, **41**, 102–107.

[91] C. E. Hayes, W. A. Edelstein, J. F. Schenck, O. M. Mueller, M. Eash, *Journal of Magnetic Resonance*, 1985, **63**, 622–628.

[92] J. T. Vaughan, H. P. Hetherington, J. O. Otu, J. W. Pan, G. M. Pohost, *Magnetic Resonance in Medicine*, 1994, **32**, 206–218.

[93] A. G. Webb, C. M. Collins, *Int. J. Imaging Syst. Technol.*, 2010, **20**, 2–13.

[94] D. I. Hoult, *Concepts in Magnetic Resonance*, 2000, **12**, 173–187.

[95] Q. X. Yang, J. Wang, X. Zhang, C. M. Collins, M. B. Smith, H. Liu, X.-H. Zhu, J. T. Vaughan, K. Ugurbil, W. Chen, *Magnetic Resonance in Medicine*, 2002, **47**, 982–989.

[96] C. Collins, Q. Yang, J. Wang, X. Zhang, H. Liu, S. Michaeli, X.-H. Zhu, G. Adriany, J. Vaughan, P. Anderson, H. Merkle, K. Ugurbil, M. Smith, W. Chen, *Magnetic Resonance in Medicine*, 2002, **47**, 1026–1028.

[97] J. Mao, T. H. Mareci, E. R. Andrew, *Journal of Magnetic Resonance*, 1988, **79**, 1–10.

[98] G. Adriany, P.-F. Van de Moortele, F. Wiesinger, S. Moeller, J. P. Strupp, P. Andersen, C. Snyder, X. Zhang, W. Chen, K. P. Pruessmann, P. Boesiger, T. Vaughan, K. Uğurbil, *Magnetic Resonance in Medicine*, 2005, **53**, 434–445.

[99] P. B. Roemer, W. A. Edelstein, C. E. Hayes, S. P. Souza, O. M. Mueller, *Magnetic Resonance in Medicine*, 1990, **16**, 192–225.

[100] C. E. Hayes, P. B. Roemer, *Magnetic Resonance in Medicine*, 1990, **16**, 181–191.

[101] U. E. Emir, E. J. Auerbach, P.-F. V. D. Moortele, M. Marjańska, K. Uğurbil, M. Terpstra, I. Tkáč, G. Öz, *NMR in Biomedicine*, 2012, **25**, 152–160.

[102] K. Uğurbil, *IEEE Trans Biomed Eng*, 2014, **61**, 1364–1379.

[103] K. Haines, N. B. Smith, A. G. Webb, *Journal of Magnetic Resonance*, 2010, **203**, 323–327.

[104] W. M. Teeuwisse, W. M. Brink, K. N. Haines, A. G. Webb, *Magnetic Resonance in Medicine*, 2012, **67**, 912–918.

[105] J. E. M. Snaar, W. M. Teeuwisse, M. J. Versluis, M. A. van Buchem, H. E. Kan, N. B. Smith, A. G. Webb, *NMR in Biomedicine*, 2011, **24**, 873–879.

[106] W. M. Teeuwisse, W. M. Brink, A. G. Webb, *Magnetic Resonance in Medicine*, 2012, **67**, 1285–1293.

[107] Q. X. Yang, J. Wang, J. Wang, C. M. Collins, C. Wang, M. B. Smith, *Magnetic Resonance in Medicine*, 2011, **65**, 358–362.

[108] A. M. Abduljalil, P. M. Robitaille, *Journal of Computer Assisted Tomography*, 1999, **23**, 832–841.

[109] R. Gruetter, S. A. Weisdorf, V. Rajanayagan, M. Terpstra, H. Merkle, C. L. Truwit, M. Garwood, S. L. Nyberg, K. Uğurbil, *Journal of Magnetic Resonance*, 1998, **135**, 260–264.

[110] I. Tkác, G. Oz, G. Adriany, K. Uğurbil, R. Gruetter, *Magnetic Resonance in Medicine*, 2009, **62**, 868–879.

[111] A. Henning, A. Fuchs, J. B. Murdoch, P. Boesiger, *NMR in Biomedicine*, 2009, **22**, 683–696.

[112] H. P. Hetherington, N. I. Avdievich, A. M. Kuznetsov, J. W. Pan, *Magnetic Resonance in Medicine*, 2010, **63**, 9–19.

[113] N. I. Avdievich, J. W. Pan, J. M. Baehring, D. D. Spencer, H. P. Hetherington, *Magnetic Resonance in Medicine*, 2009, **62**, 17–25.

[114] V. O. Boer, D. W. J. Klomp, C. Juchem, P. R. Luijten, R. A. de Graaf, *Magnetic Resonance in Medicine*, 2012, **68**, 662–670.

[115] J. Frahm, K.-D. Merboldt, W. Hänicke, *Journal of Magnetic Resonance*, 1987, **72**, 502–508.

[116] T. W. J. Scheenen, D. W. J. Klomp, J. P. Wijnen, A. Heerschap, *Magnetic Resonance in Medicine*, 2008, **59**, 1–6.

[117] T. Ernst, J. Hennig, *Magnetic Resonance in Medicine*, 1991, **20**, 27–35.

[118] J. Théberge, R. S. Menon, P. C. Williamson, D. J. Drost, *Magnetic Resonance in Medicine*, 2005, **53**, 713–718.

[119] K. M. Koch, L. I. Sacolick, T. W. Nixon, S. McIntyre, D. L. Rothman, R. A. de Graaf, *Magnetic Resonance in Medicine*, 2007, **57**, 587–591.

[120] K. M. Koch, S. McIntyre, T. W. Nixon, D. L. Rothman, R. A. de Graaf, *Journal of Magnetic Resonance*, 2006, **180**, 286–296.

[121] R. A. de Graaf, P. B. Brown, S. McIntyre, D. L. Rothman, T. W. Nixon, *Magnetic Resonance in Medicine*, 2003, **49**, 409–416.

[122] T. A. Yousry, U. D. Schmid, H. Alkadhi, D. Schmidt, A. Peraud, A. Buettner, P. Winkler, *Brain*, 1997, **120 (Pt 1)**, 141–157.

[123] V. L. Yarnykh, *Magnetic Resonance in Medicine*, 2007, **57**, 192–200.

[124] B. Schaller, L. Xin, K. O'Brien, A. W. Magill, R. Gruetter, *NeuroImage*, 2014, **93, Part 1**, 138–145.

[125] M. Brant-Zawadzki, G. D. Gillan, W. R. Nitz, *Radiology*, 1992, **182**, 769–775.

[126] V. O. Boer, A. L. H. M. W. van Lier, J. M. Hoogduin, J. P. Wijnen, P. R. Luijten, D. W. J. Klomp, *NMR in Biomedicine*, 2011, **24**, 1038–1046.

[127] B. L. van de Bank, U. E. Emir, V. O. Boer, J. J. A. van Asten, M. C. Maas, J. P. Wijnen, H. E. Kan, G. Oz, D. W. J. Klomp, T. W. J. Scheenen, *NMR in Biomedicine*, 2015, **28**, 306–316.

[128] V. Govindaraju, K. Young, A. A. Maudsley, *NMR in Biomedicine*, 2000, **13**, 129–153.

[129] I. Tkác in *Proceedings of the 16th Annual Meeting ISMRM*, Toronto, Canada, p. 1624.

[130] K. P. Whittall, A. L. MacKay, D. A. Graeb, R. A. Nugent, D. K. Li, D. W. Paty, *Magnetic Resonance in Medicine*, 1997, **37**, 34–43.

[131] M. Jenkinson, P. Bannister, M. Brady, S. Smith, *NeuroImage*, 2002, **17**, 825–841.

[132] W. Dou, N. Palomero-Gallagher, M.-J. v. Tol, J. Kaufmann, K. Zhong, H.-G. Bernstein, H.-J. Heinze, O. Speck, M. Walter, *The Journal of Neuroscience*, 2013, **33**, 12698–12704.

[133] J. M. Bland, D. G. Altman, *Statistical Methods in Medical Research*, 1999, **8**, 135–160.

[134] M. Marjańska, E. J. Auerbach, R. Valabrègue, P.-F. Van de Moortele, G. Adriany, M. Garwood, *NMR in Biomedicine*, 2012, **25**, 332–339.

[135] W. D. Rooney, G. Johnson, X. Li, E. R. Cohen, S.-G. Kim, K. Ugurbil, C. S. Springer, Jr, *Magnetic Resonance in Medicine*, 2007, **57**, 308–318.

[136] L. Xin, B. Schaller, V. Mlynarik, H. Lu, R. Gruetter, *Magnetic Resonance in Medicine*, 2013, **69**, 931–936.

[137] J. Shen, D. L. Rothman, H. P. Hetherington, J. W. Pan, *Magnetic Resonance in Medicine*, 1999, **42**, 1082–1088.

[138] J. Near, J. Andersson, E. Maron, R. Mekle, R. Gruetter, P. Cowen, P. Jezzard, *NMR in Biomedicine*, 2013, **26**, 1353–1362.

[139] J. Lynch, J. Peeling, A. Auty, G. R. Sutherland, *The Canadian Journal of Neurological Sciences*, 1993, **20**, 194–198.

[140] M. A. McLean, F. G. Woermann, G. J. Barker, J. S. Duncan, *Magnetic Resonance in Medicine*, 2000, **44**, 401–411.

[141] H. P. Hetherington, G. F. Mason, J. W. Pan, S. L. Ponder, J. T. Vaughan, D. B. Twieg, G. M. Pohost, *Magnetic Resonance in Medicine*, 1994, **32**, 565–571.

[142] N. Schuff, F. Ezekiel, A. C. Gamst, D. L. Amend, A. A. Capizzano, A. A. Maudsley, M. Weiner, *Magnetic Resonance in Medicine*, 2001, **45**, 899–907.

[143] C. Gasparovic, R. Yeo, M. Mannell, J. Ling, R. Elgie, J. Phillips, D. Doezema, A. R. Mayer, *Journal of Neurotrauma*, 2009, **26**, 1635–1643.

[144] G. Tsai, B. Stauch-Slusher, L. Sim, J. C. Hedreen, J. D. Rothstein, R. Kuncl, J. T. Coyle, *Brain Research*, 1991, **556**, 151–156.

[145] M. Banay-Schwartz, M. Palkovits, A. Lajtha, *Neurochemical Research*, 1993, **18**, 417–423.

[146] J. a. M. van der Heyden, J. Korf, *Journal of Neurochemistry*, 1978, **31**, 197–203.

[147] W. E. Finkbeiner, P. C. Ursell, R. L. D. (M.D.), *Autopsy Pathology: A Manual and Atlas*, Saunders Elsevier, Philadelphia, PA, 2009.

[148] S. Sengupta, E. B. Welch, Y. Zhao, D. Foxall, P. Starewicz, A. W. Anderson, J. C. Gore, M. J. Avison, *Magnetic Resonance Imaging*, 2011, **29**, 483–496.

[149] C. Juchem, T. W. Nixon, P. Diduch, D. L. Rothman, P. Starewicz, R. A. de Graaf, *Concepts in magnetic resonance. Part B: Magnetic resonance engineering*, 2010, **37B**, 116–128.

[150] E. M. P. Poels, L. S. Kegeles, J. T. Kantrowitz, M. Slifstein, D. C. Javitt, J. A. Lieberman, A. Abi-Dargham, R. R. Girgis, *Molecular Psychiatry*, 2014, **19**, 20–29.

[151] M. C. Lee, I. Tracey, *British Journal of Anaesthesia*, 2013, **111**, 64–72.

[152] V. Bachtiar, C. J. Stagg, *Neuroscience*, 2014, **278**, 93–104.

[153] C. J. Stagg, *NeuroImage*, 2014, **86**, 19–27.

[154] M. A. Nitsche, W. Paulus, *The Journal of Physiology*, 2000, **527 Pt 3**, 633–639.

[155] L. J. Bindman, O. C. J. Lippold, J. W. T. Redfearn, *The Journal of Physiology*, 1964, **172**, 369–382.

[156] R. Lindenberg, L. Nachtigall, M. Meinzer, M. M. Sieg, A. Flöel, *The Journal of Neuroscience*, 2013, **33**, 9176–9183.

[157] C. J. Stagg, V. Bachtiar, H. Johansen-Berg, *Current Biology*, 2011, **21**, 480–484.

[158] J. Reis, H. M. Schambra, L. G. Cohen, E. R. Buch, B. Fritsch, E. Zarahn, P. A. Celnik, J. W. Krakauer, *Proceedings of the National Academy of Sciences of the United States of America*, 2009, **106**, 1590–1595.

[159] C. J. Stagg, V. Bachtiar, J. O'Shea, C. Allman, R. A. Bosnell, U. Kischka, P. M. Matthews, H. Johansen-Berg, *Brain*, 2011, **135**, 276–284.

[160] M. A. Nitsche, K. Fricke, U. Henschke, A. Schlitterlau, D. Liebetanz, N. Lang, S. Henning, F. Tergau, W. Paulus, *The Journal of Physiology*, 2003, **553**, 293–301.

[161] M. A. Nitsche, D. Liebetanz, A. Schlitterlau, U. Henschke, K. Fricke, K. Frommann, N. Lang, S. Henning, W. Paulus, F. Tergau, *The European Journal of Neuroscience*, 2004, **19**, 2720–2726.

[162] C. J. Stagg, J. G. Best, M. C. Stephenson, J. O'Shea, M. Wylezinska, Z. T. Kincses, P. G. Morris, P. M. Matthews, H. Johansen-Berg, *The Journal of Neuroscience*, 2009, **29**, 5202–5206.

[163] M. Rango, F. Cogiamanian, S. Marceglia, B. Barberis, A. Arighi, P. Biondetti, A. Priori, *Magnetic Resonance in Medicine*, 2008, **60**, 782–789.

[164] S. Karok, A. G. Witney, *PLoS ONE*, 2013, **8**, e85693.

[165] B. W. Vines, C. Cerruti, G. Schlaug, *BMC Neuroscience*, 2008, **9**, 103.

[166] D. J. Kidgell, A. M. Goodwill, A. K. Frazer, R. M. Daly, *BMC Neuroscience*, 2013, **14**, 64.

[167] B. Sehm, J. Kipping, A. Schäfer, A. Villringer, P. Ragert, *Frontiers in Human Neuroscience*, 2013, **7**, 183.

[168] J. O'Shea, M.-H. Boudrias, C. J. Stagg, V. Bachtiar, U. Kischka, J. U. Blicher, H. Johansen-Berg, *Neuroimage*, 2014, **85**, 924–933.

[169] S. Kim, M. C. Stephenson, P. G. Morris, S. R. Jackson, *NeuroImage*, 2014, **99**, 237–243.

[170] J. R. Keltner, L. L. Wald, B. D. Frederick, P. F. Renshaw, *Magnetic Resonance in Medicine*, 1997, **37**, 366–371.

[171] Y. Ke, B. M. Cohen, J. Y. Bang, M. Yang, P. F. Renshaw, *Psychiatry Research: Neuroimaging*, 2000, **100**, 169–178.

[172] R. C. Oldfield, *Neuropsychologia*, 1971, **9**, 97–113.

[173] P. C. Gandiga, F. C. Hummel, L. G. Cohen, *Clinical Neurophysiology*, 2006, **117**, 845–850.

[174] R. Kreis, *Magnetic Resonance in Medicine*, 2015, n/a–n/a.

[175] R. Jayasundar, *Neurology India*, 2002, **50**, 267.

[176] S. D. Glick, D. A. Ross, L. B. Hough, *Brain Research*, 1982, **234**, 53–63.

[177] Y. Safriel, M. Pol-Rodriguez, E. J. Novotny, D. L. Rothman, R. K. Fulbright, *American Journal of Neuroradiology*, 2005, **26**, 1439–1445.

[178] C. Choi, S. K. Ganji, R. J. DeBerardinis, K. J. Hatanpaa, D. Rakheja, Z. Kovacs, X.-L. Yang, T. Mashimo, J. M. Raisanen, I. Marin-Valencia, J. M. Pascual, C. J. Madden, B. E. Mickey, C. R. Malloy, R. M. Bachoo, E. A. Maher, *Nature Medicine*, 2012, **18**, 624–629.

[179] L. An, S. Li, J. B. Murdoch, M. F. Araneta, C. Johnson, J. Shen, *Magnetic Resonance in Medicine*, 2015, **73**, 451–458.

[180] J. Shen, J. Yang, I.-Y. Choi, S. S. Li, Z. Chen, *Journal of Magnetic Resonance*, 2004, **170**, 290–298.

[181] U. Seeger, U. Klose, I. Mader, W. Grodd, T. Nägele, *Magnetic Resonance in Medicine*, 2003, **49**, 19–28.

[182] F. A. Howe, S. J. Barton, S. A. Cudlip, M. Stubbs, D. E. Saunders, M. Murphy, P. Wilkins, K. S. Opstad, V. L. Doyle, M. A. McLean, B. A. Bell, J. R. Griffiths, *Magnetic Resonance in Medicine*, 2003, **49**, 223–232.

[183] G. D. Graham, J. H. Hwang, D. L. Rothman, J. W. Prichard, *Stroke; a Journal of Cerebral Circulation*, 2001, **32**, 2797–2802.

[184] L. Hofmann, J. Slotboom, C. Boesch, R. Kreis, *Magnetic Resonance in Medicine*, 2001, **46**, 855–863.

[185] B. Schaller, L. Xin, R. Gruetter, *Magnetic Resonance in Medicine*, 2014, **72**, 934–940.

[186] H. Y. Carr, E. M. Purcell, *Physical Review*, 1954, **94**, 630–638.

[187] S. Meiboom, D. Gill, *Review of Scientific Instruments*, 1958, **29**, 688.

[188] E. J. Wells, H. S. Gutowsky, *The Journal of Chemical Physics*, 1965, **43**, 3414–3415.

[189] J. Hennig, T. Thiel, O. Speck, *Magnetic Resonance in Medicine*, 1997, **37**, 816–820.

[190] B. J. Soher, P. M. Pattany, G. B. Matson, A. A. Maudsley, *Magnetic Resonance in Medicine*, 2005, **53**, 1283–1287.

[191] K. Takegoshi, K. Ogura, K. Hikichi, *Journal of Magnetic Resonance*, 1989, **84**, 611–615.

[192] P. C. van Zijl, C. T. Moonen, M. von Kienlin, *Journal of Magnetic Resonance*, 1990, **89**, 28–40.

[193] H. K. Lee, A. Yaman, O. Nalcioglu, *Magnetic Resonance in Medicine*, 1995, **34**, 253–259.

[194] J. Shen, *Journal of Magnetic Resonance*, 2003, **163**, 73–80.

[195] M. H. Levitt, R. Freeman, *Journal of Magnetic Resonance*, 1981, **43**, 65–80.

[196] A. J. Shaka, S. P. Rucker, A. Pines, *Journal of Magnetic Resonance*, 1988, **77**, 606–611.

[197] M. H. Levitt, R. Freeman, *Journal of Magnetic Resonance*, 1981, **43**, 502–507.

[198] D. K. Deelchand, P.-G. Henry, K. Uğurbil, M. Marjańska, *Magnetic Resonance in Medicine*, 2012, **67**, 891–897.

[199] G. E. Santyr, R. M. Henkelman, M. J. Bronskill, *Journal of Magnetic Resonance*, 1988, **79**, 28–44.

[200] T. Lange, U. Dydak, T. P. L. Roberts, H. A. Rowley, M. Bjeljac, P. Boesiger, *American Journal of Neuroradiology*, 2006, **27**, 895–901.

[201] D. K. Deelchand, P.-G. Henry, M. Marjańska, *Magnetic Resonance in Medicine*, 2015, **73**, 13–20.

[202] S. Michaeli, M. Garwood, X.-H. Zhu, L. DelaBarre, P. Andersen, G. Adriany, H. Merkle, K. Ugurbil, W. Chen, *Magnetic Resonance in Medicine*, 2002, **47**, 629–633.

[203] J. Pan, N. Avdievich, H. Hetherington, *Magnetic Resonance in Medicine*, 2010, **64**, 1237–1246.

[204] Y. Zhang, J. Zhou, P. A. Bottomley, *Magnetic Resonance in Medicine*, 2015, **74**, 320–329.

[205] V. Boer, D. Klomp, J. Laterra, P. Barker, *Magnetic Resonance in Medicine*, 2015, n/a–n/a.

[206] J. L. Y. Cheong, E. B. Cady, J. Penrice, J. S. Wyatt, I. J. Cox, N. J. Robertson, *AJNR. American journal of neuroradiology*, 2006, **27**, 1546–1554.

[207] A. MacKay, C. Laule, I. Vavasour, T. Bjarnason, S. Kolind, B. Mädler, *Magnetic Resonance Imaging*, 2006, **24**, 515–525.

[208] M. D. Does, R. E. Snyder, *Magnetic Resonance in Medicine*, 1996, **35**, 207–213.

[209] D. Ongür, A. P. Prescot, J. E. Jensen, E. D. Rouse, B. M. Cohen, P. F. Renshaw, D. P. Olson, *Magnetic Resonance in Medicine*, 2010, **63**, 1–8.

[210] O. C. Andronesi, O. Rapalino, E. Gerstner, A. Chi, T. T. Batchelor, D. P. Cahill, A. G. Sorensen, B. R. Rosen, *The Journal of Clinical Investigation*, 2013, **123**, 3659–3663.

Appendix A

Density Matrix, Product Operator Formalism and Phase Cycling

The density matrix provides an elegant method of describing a quantum state for an ensemble of spin-1/2 spins without referring to individual spin states explicitly. If we start with a single spin in a general state:

$$|\psi\rangle = \begin{pmatrix} c_\alpha \\ c_\beta \end{pmatrix} \tag{A.1}$$

and the expectation value of an operator $\hat{Q}$ is:

$$\begin{aligned} \langle \hat{Q} \rangle &= \langle \psi | \hat{Q} | \psi \rangle \\ &= \begin{pmatrix} c_\alpha^* & c_\beta^* \end{pmatrix} \begin{pmatrix} Q_{\alpha\alpha} & Q_{\alpha\beta} \\ Q_{\beta\alpha} & Q_{\beta\beta} \end{pmatrix} \begin{pmatrix} c_\alpha \\ c_\beta \end{pmatrix} \\ &= c_\alpha c_\alpha^* Q_{\alpha\alpha} + c_\alpha c_\beta^* Q_{\alpha\beta} + c_\beta c_\alpha^* Q_{\beta\alpha} + c_\beta c_\beta^* Q_{\beta\beta} \end{aligned} \tag{A.2}$$

which suggests that we can alternatively express the original state as quadratic products of the original coefficients c_α and c_β. This is accomplished by multiplying $|\psi\rangle$

with $\langle\psi|$:

$$|\psi\rangle\langle\psi| = \begin{pmatrix} c_\alpha c_\alpha^* & c_\alpha c_\beta^* \\ c_\beta c_\alpha^* & c_\beta c_\beta^* \end{pmatrix} \tag{A.3}$$

and now the expectation value of the operator $\hat{Q}$ can be determined from the trace operation:

$$\langle\hat{Q}\rangle = \mathrm{Tr}\{|\psi\rangle\langle\psi|\hat{Q}\} \tag{A.4}$$

which is equivalent to Eq. A.2. While this isn't particularly helpful (we have exchanged two numbers to represent the system (c_α and c_β) for four ($c_\alpha c_\alpha^*$, $c_\alpha c_\beta^*$, $c_\beta c_\alpha^*$, $c_\beta c_\beta^*$), but if we extend our spin system to a large number of spins we now get:

$$\langle\hat{Q}\rangle = \mathrm{Tr}\{(|\psi_1\rangle\langle\psi_1| + |\psi_2\rangle\langle\psi_2| + |\psi_3\rangle\langle\psi_3| + \ldots)\hat{Q}\} \tag{A.5}$$

where the sum is taken over all spins. If we define the spin density operator as $\hat{\rho} = \overline{|\psi\rangle\langle\psi|}$ (the average over all spins) we can express the expectation value for an operator $\hat{Q}$ as:

$$\langle\hat{Q}\rangle = \mathrm{Tr}\{\hat{\rho}\hat{Q}\} \tag{A.6}$$

This result is remarkable as it suggests that any macroscopic observation of a spin ensemble can be determined from only two spin operators - independent of the number of spins the ensemble contains. The matrix representation of $\hat{\rho}$ for an ensemble of non-interacting spins is:

$$\hat{\rho} = \begin{pmatrix} \rho_{\alpha\alpha} & \rho_{\alpha\beta} \\ \rho_{\beta\alpha} & \rho_{\beta\beta} \end{pmatrix} = \begin{pmatrix} \overline{c_\alpha c_\alpha^*} & \overline{c_\alpha c_\beta^*} \\ \overline{c_\beta c_\alpha^*} & \overline{c_\beta c_\beta^*} \end{pmatrix} \tag{A.7}$$

where the populations of states $|\alpha\rangle$ and $|\beta\rangle$ are given by $\rho_{\alpha\alpha}$ and $\rho_{\beta\beta}$ respectively and the off diagonal elements are called *coherences* between states. For coupled spins the density matrix naturally becomes larger (due to more possible energy states) and new

coherences can arise (called multiple-quantum coherences).

According to the Liouville-von Newmann equation for a time independent Hamiltonian the time dependence of the density matrix of a system is given by:

$$\hat{\rho}(t) = \exp(-i\hat{H}t)\hat{\rho}_0 \exp(i\hat{H}t) \tag{A.8}$$

where $\hat{\rho}_0$ is the density matrix at $t = 0$, $\hat{H}$ is the Hamiltonian of the system and $\exp(-i\hat{H}t)$ is the time evolution operator. This suggests that we can calculate the state of a spin system at any time as long as we know the initial state of the spin system, the Hamiltonians that are acting on the spins and the duration of interaction. Quantum coherences are generally classified by their order n (represented by the density operator $\rho^{(n)}$). A coherence of order n will rotate about the z-axis by angle ϕ rotate according to:

$$\exp(-i\phi F_z)\rho^{(n)} \exp(i\phi F_z) = \exp(-ni\phi)\rho^{(n)} \tag{A.9}$$

where F_z is the operator for the total z-component of the spin angular momentum - *i.e.* a coherence of order n experiences a phase shift of $-n\phi$. Only the -1 single quantum coherence is observable.

Although the density matrix formalism an accurate picture, it can become very cumbersome when applied to a multi-spin system and a complicated pulse sequence. Additionally, even after density matrix calculations, it may not provide much insight into why a particular pulse sequence performs the way it does. An alternative formalism, called the product operator formalism, provides a more intuitive approach to understanding complex pulse sequences. In the product operator formalism the density matrix is expressed as a linear combination of base operators and any subsequent evolution of the density matrix can also be expressed with these operators. Product operators also provide a method of keeping track of coherence order but

the formalism only applies for either non-interacting or weakly coupled spin systems (when the difference in chemical shift between coupled spins is much larger than the J-coupling). For a 2 spin system (spin I and spin S) the product operators are:

I_x	X component of I-spin magnetization
I_y	Y component of the I-spin magnetization
I_z	Z component of I-spin magnetization
S_x	X component of S-spin magnetization
S_y	Y component of S-spin magnetization
S_z	Z component of S-spin magnetization
$2I_xS_z$	Antiphase I-spin magnetization
$2I_yS_z$	Antiphase I-spin magnetization
$2I_zS_x$	Antiphase S-spin magnetization
$2I_zS_y$	Antiphase S-spin magnetization
$2I_zS_z$	Longitudinal two-spin order
$2I_xS_x$	Two-spin coherence
$2I_xS_y$	Two-spin coherence
$2I_yS_x$	Two-spin coherence
$2I_yS_y$	Two-spin coherence

Table A.1: Product operators for a two spin-1/2 system

For our purposes there are three main Hamiltonians that we are concerned with:

RF Pulses (i is axis of applied pulse)	$H = \alpha I_i$
Chemical Shift Evolution	$H = \omega I_z$
Scalar (J) Coupling	$H = 2\pi J_{IS} I_z S_z$

Table A.2: Hamiltonians for Product Operator Formalism

Thus using the list of operators and our three Hamiltonians we are left with a rather simple set of rules from which any pulse sequence can be analyzed:

One can classify coherence according to an order p which takes integer values 0, ± 1, ± 2, ... This definition comes about in order to differentiate how different coherences respond to a rotation about the z-axis. A coherence of order p ($\sigma^{(p)}$) evolves under a z-rotation of angle ϕ by:

$$e^{-i\phi F_z}\sigma^{(p)}e^{i\phi F_z} = e^{-ip\phi}\sigma^{(p)} \tag{A.10}$$

Pulses along the x or y axes	Chemical Shift Evolution
$I_z \xrightarrow{\alpha I_x} I_z\cos(\alpha) - I_y\sin(\alpha)$	$I_z \xrightarrow{\omega t I_z} I_z$
$I_z \xrightarrow{\alpha I_y} I_z\cos(\alpha) + I_x\sin(\alpha)$	$I_x \xrightarrow{\omega t I_z} I_x\cos(\omega t) + I_y\sin(\omega t)$
$I_x \xrightarrow{\alpha I_x} I_x$	$I_y \xrightarrow{\omega t I_z} I_y\cos(\omega t) - I_x\sin(\omega t)$
$I_y \xrightarrow{\alpha I_y} I_y$	
$I_y \xrightarrow{\alpha I_x} I_y\cos(\alpha) + I_z\sin(\alpha)$	
$I_x \xrightarrow{\alpha I y_x} I_x\cos(\alpha) - I_z\sin(\alpha)$	
Scalar Coupling	
$I_z \xrightarrow{\pi J t I_z S_z} I_z$	
$2I_xS_y \xrightarrow{\pi J t I_z S_z} 2I_xS_y$	
$I_y \xrightarrow{\pi J t I_z S_z} I_y\cos(\pi Jt) - 2I_xS_z\sin(\pi Jt)$	
$I_x \xrightarrow{\pi J t I_z S_z} I_x\cos(\pi Jt) + 2I_yS_z\sin(\pi Jt)$	
$2I_yS_z \xrightarrow{\pi J t I_z S_z} 2I_yS_z\cos(\pi Jt) - I_x\sin(\pi Jt)$	
$2I_xS_z \xrightarrow{\pi J t I_z S_z} 2I_xS_z\cos(\pi Jt) + I_y\sin(\pi Jt)$	

Table A.3: Summary of product operator formalism for spin I in a 2 spin system (I and S)

where F_z is the operator of the total z-component of the spin angular momentum. In other words, a coherence of order p acquires a phase shift of $-p\phi$. RF pulses cause coherences to be transferred between orders and this can be exploited in pulse sequence design to remove unwanted coherences. This is due to the fact that if the phase of a pulse that changes a coherence by Δp is shifted by $\Delta\phi$, the coherence acquires a phase shift of $-\Delta p \cdot \Delta\phi$. By changing the phase of pulses between acquisitions, coherences can be carefully removed. Additionally, changing the receiver phase can generate additional phase shifts. For example, to select a coherence that transfers from +2 to -1 ($\Delta p = -3$) we could employ the following phase cycle for a signal pulse:

Step	Pulse phase	Phase shift for $\Delta p = -3$	Receiver shift for $\Delta p = -3$	Difference
1	0°	0°	0°	0°
2	90°	270°	270°	0°
3	180°	180°	180°	0°
4	270°	90°	90°	0°

Table A.4: Phase cycle to select coherence transfer from +2 to -1.

So signals acquired from the 4 averages will add up. Using the same phase cycle what about the pathway $\Delta p = +2$?

Step	Pulse phase	Phase shift for $\Delta p = -3$	Receiver shift for $\Delta p = -3$	Difference
1	0°	0°	0°	0°
2	90°	180°	270°	90°
3	180°	0°	180°	180°
4	270°	180°	90°	270°

Table A.5: Phase cycle for $\Delta p = +2$

Because the phase differences cancel each other out, this pathway will be rejected.